# A Solid State NMR Study of the Local Mobility of Water and Water Induced Dynamics of Linkers on Silica Surface

A thesis submitted

in partial fulfilment for the award of the degree of

**Doctor of Philosophy**

in

**Physics**

by

**V. S. Veena**

**Department of Physics**

**Indian Institute of Space Science and Technology**

**Thiruvananthapuram, India.**

**March 2021**

# Certificate

This is to certify that the thesis titled **'*A Solid State NMR Study of the Local Mobility of Water and Water Induced Dynamics of Linkers on Silica Surface*'**, submitted by **V. S. Veena**, to the Indian Institute of Space Science and Technology, Thiruvananthapuram, in partial fulfilment for the award of the degree of **Doctor of Philosophy** in **Physics**, is a bonafide record of the internship work carried out by her under my supervision. The contents of this report, in full or in parts, have not been submitted to any other Institute or University for the award of any degree or diploma.

S. Jayanthi

Associate Professor

Umesh R. Kadhane

Professor

**Place:** Thiruvananthapuram
**Date:** March 24, 2021

# Declaration

I declare that this thesis titled **'*A Solid State NMR Study of the Local Mobility of Water and Water Induced Dynamics of Linkers on Silica Surface*'**, submitted in partial fulfilment for the award of the degree of **Doctor of Philosophy** in **Physics** is a record of original work carried out by me under the supervision of Dr. S. Jayanthi, and has not formed the basis for the award of any degree, diploma, associateship, fellowship, or other titles in this or any other Institution or University of higher learning. In keeping with the ethical practice in reporting scientific information, due acknowledgments have been made wherever the findings of others have been cited.

**Place:** Thiruvananthapuram
**Date:** March 24, 2021

V. S. Veena
(SC16D054)

*To my beloved Family, Friends, and Teachers.*

# Acknowledgments

Completion of this doctoral thesis was possible because of the support of several people. I would like to express my sincere gratitude to many for my academic, intellectual and emotional development during the past few years.

My research supervisor, ***Dr. S. Jayanthi***, deserves respect and admiration in many respects. I often marvelled at her ever growing enthusiasm and passion for research, which was highly contagious and inspirational for me. She has opened the windows for me to the amazing world of Nuclear Magnetic Resonance (NMR). I wish to express my deepest gratitude for her dedication, patience, time, and constant support, at tough times during the pursuit of research. I am highly grateful to her for helping me develop the attitude of independent thinking and build the confidence to pursue independent research.

***Dr. T. G Ajithkumar*** and ***Ms. Kavya Illath*** at National Chemical Laboratory (NCL) Pune deserve special thanks. With **no NMR facility at IIST**, it would have been impossible to meet the requirements of the project without the timely help and extensive support by them. I take this opportunity to thank them for their creative suggestions, time, and hospitality. Thanks are also due to ***Dr. C. P Vinod*** and ***Dr. Anish Lazar*** at NCL Pune for synthesis of the mesoporous materials and relevant discussions.

Doctoral Committee members, ***Dr. S. Raghothama - IISc***, ***Dr. Umesh R. Kadhane - IIST***, and ***Dr. Samir Mandal - IIST,*** were always supportive at different stages of my research and helped me progress with their valuable suggestions and constructive criticism. I take this opportunity to express my heartfelt gratitude to them. I also take this opportunity to thank Dr. Umesh R. Kadhane and ***Ms. M. V. Vinitha*** for providing infrastructure support in the initial stages of my research.

I gratefully acknowledge IIST's former and present Directors, ***Dr. K. S. Das Gupta*** and ***Dr. V. K. Dadhwal*** for providing academic support, for financial support in the year 2019-2020 in terms of IIST research fellowship, and for good infrastructure facilities during my tenure. I thank the cooperation and inspiring words of teaching and non-teaching staff and of research scholars of the *Department of Physics*.

The financial support of ***'Science and Engineering Research Board'*** (SERB), under Department of Science and Technology (DST) is truly appreciated. Without the support of Junior and Senior Research Fellowship (JRF/SRF) funded by SERB-DST, during 2016-2019, it would have been impossible for me to pursue my research studies.

I express my heartfelt thanks to ***Prof. Shimon Vega, Weizmann Institute of Science - Israel*** for his excellent scientific discussions and constructive criticism. Valuable discussions and suggestions by ***Dr. Adonis Lupulescu*** during experimental time at NCL-Pune and TIFR-Centre for Interdisciplinary Sciences, Hyderabad (TCIS) are highly appreciated and will be cherished.

I had the opportunity to work at the solid state NMR facility at TCIS where I had been exposed to the intricacies of methodological development in solid state NMR. I take this opportunity to thank ***Prof. P. K. Madhu*** for providing measurement time, various NMR discussions, for supporting my application to TCIS NMR training session, and for his generous hospitality. Thanks are also due to ***Dr. Kaustubh R. Mote*** and research students at NMR centre, TCIS, during hands-on training on the spectrometers.

I acknowledge my colleagues ***Mr. V. S. Sajith*** and ***Mr. K. Praveen Kumar*** for the good research ambience and their contagious enthusiasm. The environment was often filled with academic discussions and the interactions with them will always be cherished. I take this opportunity to thank my friends and research scholars at IIST, ***Ms. Anuja, Ms. Arya, Ms Arul Selvi, Ms. Soumya, Mr. Manu, Mr. Sarath,*** and ***Ms. Risha,*** for their love, support and care that helped me stay focused on my research. My friends, ***Ms. Aswathy, Ms. Suchithra, Ms. Dhanya,*** and ***Dr. Sreeju*** are gratefully acknowledged for having faith in me and encouraging me to pursue research. They will be always remembered.

Thanks are due to my Physics teachers, ***Dr. V. M. Ananda Kumar, Ms. B. S. Deepthi, Ms. O. K. Saritha***, who ignited my fascination to research. Their classes and discussions motivated me to select a research career. I would like to thank ***Forensic Science Laboratory*** (FSL), Department of Police - Government of Kerala, for granting me education leave to complete my Ph.D tenure.

I am grateful for a supporting and understanding family, who walked with me through thick and thin. I take this opportunity to thank my ***parents*** and my ***sibling*** for their unconditional love and support. They are my pillars and source of strength. Words fail in thanking my ***mother*** for her unassuming support and selfless love. I extend my deepest gratitude to my ***husband***, who has been very tolerant and understanding. I express my sincere gratitude to my ***extended family*** that helped me in all possible ways during this challenging period.

# Abstract

Materials with hybrid organic-inorganic interface, large void pore volume, high surface area per unit volume, and broad pore size distribution, are used in diverse applications like molecular transport, surface catalysis, bio-mineralization etc., where water is the most widely used solvent. In the work presented here, we have employed proton and deuterium solid state magic angle spinning (MAS) NMR to investigate the distribution of water on silica surface and water induced dynamics of functionalized silica materials. Our study contributes to the understanding of surface binding, pore filling, and local dynamics in mesoporous hybrid materials.

In the first part of the work, we have employed existing solid state NMR techniques to investigate the distribution of water molecules near the pore surface of $PMO_E$. Proton MAS NMR spectra of $PMO_E$ acquired at different hydration levels are analysed and interpreted in terms of water clusters of various sizes and distributions of water layers on the pore surface. Based on the analysis, a possible pore filling mechanism is proposed. For $PMO_E$, the proton spectral analysis suggests that both radial and axial filling mechanisms play a significant role in the hydration process. Formation of larger clusters at lower hydration suggests that the pores of $PMO_E$ are getting filled with water at lower hydration levels than those of SBA-15. The challenges faced while analysing $^1H$ MAS NMR spectra of $PMO_E$ are addressed.

Correlation between dynamics induced by a few water molecules/$nm^2$ on SBA-15 amine-functionalized linkers and the resultant possible molecular conformations is the main focus of the study in the second part of the work presented here. Two widely used mesoporous hybrid materials with amine functionalization are used in the study. The diamines tethered at the end group of GPTMS and MATMS are deuterated. By analysing deuterium and proton MAS NMR spectra acquired at different temperatures and various hydration levels, dynamics of the linkers and its dependence on temperature is investigated. Effective quadrupolar parameters calculated from deuterium MAS NMR spectra were indicative of molecular dynamics induced by a few water molecules within the proximity of the grafted linkers. *A-priori* molecular dynamic simulations were performed to (i) derive possible molecular conformations associated with dynamics, (ii) to understand the connection between the length of the linker and dynamics, and (iii) to understand the restriction on dynamics due to steric hindrance generated by double bonds. The effective quadrupolar parameters calculated from the MD simulations were consistent with those obtained from deuterium MAS NMR analysis.

# Contents

# List of Figures

# List of Tables

# I

## 1. Introduction

One of the major goals of studying materials and biomolecules is establishing relation between structure and function. Nuclear magnetic resonance (NMR) [1,2] spectroscopy is a versatile and non-invasive analytical tool for probing molecular level structure and dynamics. NMR experiments involve nuclei which possess a non-vanishing spin and hence a non-zero nuclear magnetic moment [3,4]. In an NMR experiment, the sample under study is placed in a large external magnetic field that exhibits high temporal stability and spatial homogeneity. The nuclear spins in the sample are then subjected for a short time to a resonant magnetic field oscillating in the radiofrequency (RF) range. The effect of this brief irradiation, called RF pulse, is to tilt nuclear magnetization into a plane perpendicular to the static magnetic field. After the RF pulse is switched off nuclear magnetization precesses around the static magnetic field and induces a voltage in the same coil which was used for excitation. This current is recorded and constitutes the NMR signal. The NMR signal is Fourier transformed [5] and the result constitutes the NMR spectrum. The appearance of an NMR spectrum depends on the spin interactions in the sample hence on the environment of the nuclei involved in the experiment, such that information on molecular structure and dynamics can be derived [6,7].

In the periodic table, more than 70% of atoms possess non-zero magnetic moment and hence may be involved in NMR experiments. Protons ($^{1}$H) have almost 100% natural abundance, are highly sensitive due to high gyromagnetic ratio, and are present in most organic molecules, hence $^{1}$H NMR is widely used for structural determination. Commonly occurring elements in biomolecules are carbon and nitrogen. NMR experiments involving these elements are usually performed with $^{13}$C (nuclear spin ½, 1.1% abundance) and $^{15}$N (nuclear spin ½, 0.4% abundance), isotopes. Because of the low abundance, often experiments are performed after $^{13}$C and/or $^{15}$N isotopic enrichment. A few important and noticeable features of an NMR spectrum are: the characteristic frequencies at which spectral lines appear, the width of each line, the areas enclosed by peaks, and the multiplicities of the peaks. In case of solution state NMR, rapid molecular tumbling results in narrow, high resolution NMR spectra. With complex molecules, higher dimensional NMR experiments can be performed correlating various spins and spin interactions in multiple dimensions, from which configuration and conformation of biopolymers – proteins, nucleic acids and their

complexes can be precisely determined [8,9]. NMR spectral analysis provides information about the chemical environment, number of nuclei with same magnetic and chemical equivalence, the nearest neighbour interactions, purity of the sample, sample concentration, information on intramolecular motions such as rotation, diffusion, and so on. The process through which perturbed nuclei return to thermal equilibrium, termed as relaxation, is particularly reflected in the widths of the NMR resonances [7]. Relaxation depends on the local environment of the nuclear spins and on molecular motion, hence NMR relaxation studies often provide valuable information on molecular structure and dynamics [3].

Solid state NMR is widely used in materials chemistry and in structure determination of biological systems [10-13]. Most of the inorganic materials, minerals and membrane proteins are insoluble in any solvents or water and hence solid state NMR naturally becomes a method of choice. When the sample under study is in the form of a polycrystalline solid, NMR spectra exhibit broad features due to the fact that spin interactions are orientation dependent. This results in low resolution spectra and hence structural information is hard to retrieve. In order to attain high resolution spectra mimicking solution NMR, solid state NMR usually employs spinning the sample at 'magic angle' ($54.7^{o}$ with respect to the static magnetic field), which averages out the orientation dependent spin interactions resulting in narrow spectral lines and higher signal-to-noise ratio (sensitivity) [14-16]. Even under magic angle spinning (MAS) proton solid state NMR spectra are severely broadened by $^{1}H$-$^{1}H$ homonuclear dipolar interactions, which are not averaged out by sample rotation. Therefore, contrary to solution NMR, proton solid state MAS NMR is not very informative unless the sample is spun at MAS rates considerably higher than the interaction strength. However, if molecular dynamics is present, the resulting proton spectral lines may be sufficiently narrow, and thus may provide structural and dynamical insight. Multiple pulse sequences in association with MAS are often used to achieve resolution of protons in solid state NMR [17-19]. For experiments involving $^{13}C$, $^{15}N$ etc., cross polarization (CP/CPMAS) [20-22] is a widely used technique for achieving better sensitivity in solid samples. In CP/CPMAS, proton magnetization is transferred to the detected nucleus, which typically is less abundant and has lower gyromagnetic ratio, resulting in sensitivity enhancement. Substantial sensitivity enhancement of the detected nucleus in a CP/CPMAS experiment is achieved by RF irradiation of the protons during detection. This technique is commonly referred as heteronuclear decoupling. CPMAS and heteronuclear decoupling [23] are essential building blocks employed in various multi-dimensional experiments. With advancements in

technology and techniques, solid state NMR has become an indispensable tool for chemists to study different classes of materials such as catalysts, polymers, glasses, zeolites, electrode and electrolyte materials, pharmaceutical compounds, membrane proteins, amyloid fibrils etc.

Due to its non-destructive nature, the principles of magnetic resonance have been extended to new fields like magnetic resonance imaging (MRI) [25,26], magnetic resonance spectroscopy (MRS) [27,28], NMR metabolic profiling [29,30], dynamic nuclear polarization (DNP) [31-33], optical detection techniques [34-36], etc.

A brief introduction to the basics of NMR, including both classical and quantum mechanical pictures, is given below.

## 1.1 Basics of NMR

### 1.1.1 Classical Description of NMR

Most nuclei possess an intrinsic spin angular momentum, $\boldsymbol{I}$, and a nuclear magnetic moment, $\boldsymbol{\mu}$, associated to it. The relation between spin angular momentum and the magnetic moment [3] is given by

$$\boldsymbol{\mu} = \gamma \boldsymbol{I}, \tag{1.1}$$

where $\gamma$ is the gyromagnetic ratio, which is characteristic of a particular nuclear isotope. The classical energy of a magnetic moment $\boldsymbol{\mu}$ placed in an external magnetic field **B** is

$$E = -\boldsymbol{\mu}.\boldsymbol{B}. \tag{1.2}$$

Choosing the z axis of the coordinate system along the external magnetic field and taking into account the quantization of the spin angular momentum, energy of the magnetic moment is quantized according to,

$$E_m = -\mu_z B_0 = -\gamma m\hbar B_0, \tag{1.3}$$

where $m\hbar$ is the projection of spin angular momentum on the z axis. The spin magnetic quantum number $m$ takes $(2I + 1)$ values from $-I$ to $I$. For $I = 1/2$, $m = \pm 1/2$, corresponding to the spin-up and spin-down states denoted by $\alpha$ and $\beta$ respectively. The energy in Eq. (1.3) is called Zeeman interaction. The energy difference $\Delta E = E_{m-1} - E_m$ is given by $\Delta E = \gamma\hbar B_0$ and the corresponding angular frequency, $\omega_0 = \Delta E/\hbar$, is known as the Larmor frequency.

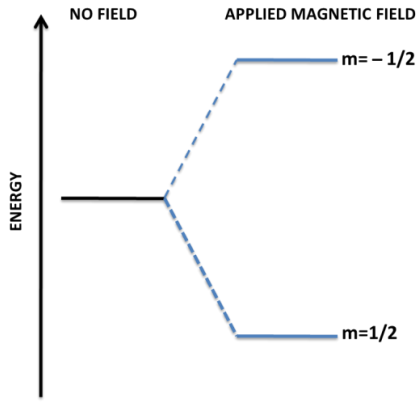


**Figure 1.1** Schematic representation of Zeeman energy levels of spin ½ nuclei.

The nuclear spins present in a sample are not isolated and interact among themselves and with the other degrees of freedom of the lattice. Therefore a description of magnetic resonance phenomena has to be based on statistical considerations. At thermal equilibrium, the arrangement of the nuclear spins over different energy levels is given by Boltzmann distribution [3,4]. For spin-1/2 nuclei, if $N_\alpha$ and $N_\beta$ are the number of nuclei per unit volume in the lower and higher energy states respectively, then

$$N_\alpha = Ce^{-\mathrm{E}_\alpha/k_BT}, N_\beta = Ce^{-\mathrm{E}_\beta/k_BT},$$

where the normalizing constant $C$ satisfies $Ce^{-\mathrm{E}_\alpha/k_BT} + Ce^{-\mathrm{E}_\beta/k_BT} = N$, and $N$ represents the total number of nuclei per unit volume, $T$ is temperature and $k_B$ is Boltzmann constant. Because of the difference between $N_\alpha$ and $N_\beta$, a net macroscopic magnetization, $\boldsymbol{M}_{eq}$, will point along the direction of the external magnetic field and it is given by

$$M_{eq} = \frac{\gamma\hbar}{2}(N_\alpha - N_\beta). \qquad (1.4)$$

For magnetic fields and temperatures encountered in most NMR experiments, $\Delta E/k_BT \ll 1$ and, by expanding in Taylor series the exponentials and retaining only the linear terms in $1/k_BT$ (the high temperature approximation), Eq. (1.4) can be simplified to [3]

$$M_{eq} = \frac{N\gamma^2\hbar^2 B_o}{4k_BT}.$$

The simplest NMR experiment proceeds as follows. The sample containing nuclear spins of interest is placed in a homogeneous static magnetic field and inside an RF coil. For a brief period of time the RF coil delivers a radiofrequency magnetic field oscillating close to Larmor frequency, termed as RF pulse. The RF magnetic field is applied perpendicular to the static magnetic field. The effect of the RF pulse is to bring the equilibrium nuclear

magnetization of the nuclear spins of interest into the plane perpendicular to the static magnetic field. After turning off the pulse, the nuclear magnetization precesses around the static magnetic field at the Larmor frequency and relaxes back to the equilibrium magnetization, $M_{eq}$. Precession of magnetization induces a current in the detection coil surrounding the sample, this current is recorded and constitutes the NMR signal or free induction decay (FID). The factors that affect the return of magnetization to equilibrium are the spin-lattice relaxation time ($T_1$) and spin-spin relaxation time ($T_2$) [3,4,7]. The spin-lattice relaxation time determines the rate of transfer of energy from the nuclear spin system to the lattice. Spin-spin relaxation time is used to quantify the decay rate of the transverse magnetization due to loss of phase coherence between nuclear spins. The time evolution of nuclear magnetization, $M$, in the presence of static and RF magnetic fields, is described by the phenomenological Bloch equations,

$$\frac{dM_z}{dt} = \gamma(M \times B)_z + \frac{M_0 - M_z}{T_1}, \tag{1.5}$$

$$\frac{dM_x}{dt} = \gamma(M \times B)_x - \frac{M_x}{T_2}, \tag{1.6}$$

$$\frac{dM_y}{dt} = \gamma(M \times B)_y - \frac{M_y}{T_2}. \tag{1.7}$$

According to Eq. (1.5-1.7), the time dependence of magnetization during detection is

$$M_z(t) = M_{eq}\left(1 - e^{-\frac{t}{T_1}}\right), \tag{1.8}$$

$$M_y(t) = M_{eq}\sin(\omega_0 t)\left(e^{-\frac{t}{T_2}}\right), \tag{1.9}$$

$$M_x(t) = M_{eq}\cos(\omega_0 t)\left(e^{-\frac{t}{T_2}}\right), \tag{1.10}$$

assuming that the magnetization points along *x* direction at the end of the RF pulse. The quadrature signal [6], $S(t)$, is proportional to $M_x(t) + iM_y(t)$ and according to Eq. (1.9, 1.10) is given by

$$S(t) \propto M_{eq}\, e^{i\omega_0 t}\; e^{-\frac{t}{T_2}} \tag{1.11}$$

The NMR spectrum, $S(\omega)$, is obtained by taking the Fourier transform of the time-domain signal $S(t)$.

$$S(\omega) = \int_0^\infty S(t)\, e^{i\omega t} dt\,.$$

For the signal in Eq. (1.11) the real part of the spectrum consists of an absorptive Lorentzian peak centered at $\omega_0$ with full width at half maximum (FWHM) $2/T_2$, or, in frequency units, $1/\pi T_2$ [3,4,6].

In real samples, spin-spin interactions and interactions with the lattice lead to spin precession at frequencies slightly different from the Larmor frequency. The slight alteration of the precession frequency is a signature of the molecular environment of the nuclei. As a result, the spectrum is usually more complex and may contain several resonance lines, each of which may exhibit a fine structure. A more accurate description of NMR, which takes into account the interactions between spins and with the electronic environment, is provided within the quantum-mechanical framework.

### 1.1.2 Quantum-Mechanical Description of NMR

In quantum mechanics, the state of a quantum system is defined by the state vector, $|\psi(t)\rangle$. The state vector evolves in time according to Schrodinger equation,

$$i\hbar \frac{d}{dt}|\psi(t)\rangle = \mathcal{H}(t)|\psi(t)\rangle \qquad (1.12)$$

where $\mathcal{H}$ is the Hamiltonian. The formal solution of Eq. (1.12) is given by

$$|\psi(t)\rangle = U(t,0)|\psi(0)\rangle,$$

where the propagator or evolution operator, $U$, is a unitary operator satisfying

$$i\hbar \frac{d}{dt}U(t,0) = \mathcal{H}(t)U(t,0),$$

and $U(0,0) = \mathbf{1}$, where $\mathbf{1}$ is the unit operator. For a time-independent Hamiltonian, the propagator is

$$U(t,0) = e^{-i\mathcal{H}t/\hbar}.$$

For a system of nuclear spins, interacting with each other and with other degrees of freedom, the statistical description of the system by means of the state vector is cumbersome and an appropriate description is provided by the density operator formalism [3,4,6].

For a non-isolated system, it is impossible to ascribe a unique state vector at a given time, but a statistical description can be given in terms of probabilities for the system of being found in a series of quantum states. If the probabilities of finding the system in state $|k\rangle$ is $p_k$, the density operator is defined as

$$\rho = \sum_k p_k \, |k\rangle\langle k|.$$

The statistical expectation value of an observable $A$ of the system is given by

$$\langle A \rangle = \sum_\alpha \langle \alpha | A\rho | \alpha \rangle = \mathrm{Tr}(A\rho)$$

where $\{|\alpha\rangle\}$ represents a basis in the Hilbert space of the quantum system. The evolution of the density operator is given by Liouville-von Neumann equation [6]

$$i\hbar \frac{d\rho}{dt} = [\mathcal{H}, \rho].$$

For a time-independent Hamiltonian, the solution of the Liouville-von Neumann equation reads

$$\rho(t) = e^{-i\mathcal{H}t} \rho(0) e^{i\mathcal{H}t},$$

where $\rho(0)$ is the initial density operator.

It can be shown that, for a system in thermal equilibrium with the environment at temperature $T$, the equilibrium density operator is

$$\rho_{eq} = \frac{1}{Z} e^{\frac{-\mathcal{H}}{k_B T}},$$

where $Z = \mathrm{Tr}\{\exp(-\mathcal{H}/k_B T)\}$.

For a nuclear spin in a uniform magnetic field, the Hamiltonian can be expressed as

$$\mathcal{H} = -\gamma \hbar I_z B_0 = \hbar \omega_0 I_z,$$

with $\omega_0 = -\gamma B_0$. For a spin ½ nucleus, the eigenvalues of $\mathcal{H}$ are $\pm\hbar\omega_0/2$ for $|\alpha\rangle$ and $|\beta\rangle$ states. For temperatures and magnetic fields occurring in NMR experiments, $\hbar|\omega_0| \ll k_B T$, and the equilibrium density operator can be approximated by

$$\rho_{eq} = \frac{1}{2}\left(\mathbf{1} - \frac{\hbar\omega_0}{k_B T} I_z\right).$$

Let us consider, within the density operator formalism, the effect of an RF pulse applied on an ensemble of spin-½ nuclei in thermal equilibrium with the lattice. The total Hamiltonian

including the RF pulse, oscillating at frequency $\omega$ and of amplitude $\omega_1 = -\gamma B_1$, where $B_1$ is the strength of oscillating magnetic field, can be written as

$$\mathcal{H} = \omega_0 I_z + 2\omega_1 I_x \cos(\omega t),$$

in angular frequency units and the factor of 2 is introduced for convenience. The corresponding propagator satisfies

$$i\frac{d}{dt}U(t,0) = \mathcal{H}(t)U(t,0).$$

The mathematical problem is simplified by first passing to a new representation called the rotating frame [3,4,6]. This is achieved by setting

$$U(t,0) = e^{-i\omega I_z t}\widetilde{U}(t,0).$$

The new propagator $\widetilde{U}$, which describes evolution of the system in the rotating frame, satisfies

$$i\frac{d}{dt}\widetilde{U}(t,0) = \widetilde{\mathcal{H}}(t)\widetilde{U}(t,0),$$

where

$$\widetilde{\mathcal{H}}(t) = (\omega_0 - \omega)I_z + e^{i\omega I_z t}\, 2\omega_1 I_x e^{-i\omega I_z t}\cos(\omega t)$$

$$= (\omega_0 - \omega)I_z + \omega_1 I_x + \omega_1 I_x \cos(2\omega t) + \omega_1 I_y \sin(2\omega t).$$

The terms rapidly oscillating at $2\omega$ can be neglected and the Hamiltonian becomes time-independent,

$$\widetilde{\mathcal{H}} \cong (\omega_0 - \omega)I_z + \omega_1 I_x.$$

If the radio frequency $\omega$ matches exactly the Larmor frequency, the density operator in the rotating frame at the end of the RF pulse of duration $\tau$ can be written as

$$\tilde{\rho}(\tau) = e^{-i\omega_1 \tau I_x}\tilde{\rho}(0)e^{i\omega_1 \tau I_x}$$

where $\tilde{\rho}(0) = \rho_{eq}$. Using $e^{-i\phi I_x} I_z e^{i\phi I_x} = I_z \cos(\phi) - I_y \sin(\phi)$, we get

$$\tilde{\rho}(\tau) = \frac{\mathbf{1}}{2} - \frac{1}{2}\frac{\hbar\omega_0}{k_B T}\left(I_z cos\omega_1\tau - I_y sin\omega_1\tau\right).$$

Taking into account that, $\mathrm{Tr}(I_y) = 0$, $\mathrm{Tr}(I_x I_y) = 0$, $\mathrm{Tr}(I_y^2) = \frac{1}{2}$, etc., the x component of magnetization is zero and the y component, is given by

$$\widetilde{M}_y(\tau) = N\langle\mu_y(\tau)\rangle = N\gamma\hbar Tr\left(I_y\tilde{\rho}(\tau)\right) = \frac{N}{4}\gamma\hbar\left(\frac{\hbar\omega_0}{k_BT}\right)sin\omega_1\tau \quad (1.13)$$

where *'tilda'* signifies that the magnetization is computed in the rotating frame and $N$ is the total number of nuclei per unit volume. It can be seen that a fraction of magnetization has been rotated into the transverse plane. The amount of transverse magnetization can be maximized by setting the duration of the RF pulse such that $\omega_1\tau = \pi/2$. In this case

$$M_y(\tau) = \frac{N\gamma\hbar^2\omega_0}{4k_BT} = -M_{eq},$$

and we see that the whole equilibrium magnetization $M_{eq}$ has been converted into transverse magnetization by the action of the RF pulse. Once the RF pulse is turned off, the transverse magnetization evolves under the Zeeman interaction with the static magnetic field and signal is detected. The density operator in the laboratory frame at the end of the RF pulse can be obtained from the density operator in the rotating frame by an inverse rotation,

$$\rho(\tau) = e^{i\omega_0 I_z\tau}\tilde{\rho}(\tau)e^{-i\omega_0 I_z\tau} = \frac{\mathbf{1}}{2} + \frac{1}{2}\frac{\hbar\omega_0}{k_BT}\left(I_y\cos\omega_0\tau + I_x sin\omega_0\tau\right).$$

Taking into account that now $\mathcal{H} = \omega_0 I_z$ in the laboratory frame, the density operator at time $t$ during detection is

$$\rho(\tau + t) = e^{-i\omega_0 I_z t}\rho(\tau)e^{i\omega_0 I_z t} = \frac{\mathbf{1}}{2} + \frac{1}{2}\frac{\hbar\omega_0}{k_BT}\left\{I_y\cos\omega_0(t-\tau) - I_x sin\omega_0(t-\tau)\right\}.$$

Proceeding in the similar way as in Eq. (1.13), we find the transverse magnetization components as

$$M_x(t) = N\gamma\hbar Tr\left(I_x\rho(t+\tau)\right) = \frac{N\gamma^2\hbar^2 B_0}{4k_BT}\{sin\omega_0(t-\tau)\},$$

$$M_y(t) = N\gamma\hbar Tr\left(I_y\rho(t+\tau)\right) = -\frac{N\gamma^2\hbar^2 B_0}{4k_BT}\{cos\omega_0(t-\tau)\}.$$

The quadrature signal is

$$S(t) \propto M_x(t) + iM_y(t) = M_{eq}e^{i\phi}e^{i\omega_0 t} \quad (1.14)$$

where $\phi = -\frac{\pi}{2} - \omega_0\tau$, is a constant phase. The Fourier transform of this signal results in a peak at the Larmor frequency $\omega_0$.

In most NMR experiments the raw signal is combined with a reference RF signal which oscillates at the same frequency $\omega$ as the RF field applied for excitation. As a result the processed signal oscillates at frequency $\omega_0 - \omega$ and it can be shown that for evaluation of this signal it is sufficient to compute the density operator in the rotating frame. Thus, if after excitation at frequency $\omega$, the system is found along $x$ in the rotating frame $(rf)$, the processed signal $S_{rf}(t)$ is

$$S_{rf}(t) \propto M_{eq} e^{i(\omega_0 - \omega)t}.$$

If $\omega_0 = \omega$, $S_{rf}$ becomes time independent. In practice $S_{rf}$ decays with relaxation time $T_2$ which is not accounted with the simple formalism developed here. From now onwards the label $'rf'$ is dropped from equations and it is understood that all calculations are performed in the rotating frame.

Since the unit operator in the density operator never contributes to NMR signal and since the actual recorded signal depends on spectrometer hardware, a further simplification in notation will be made by omitting the unit matrix and the numerical factors in the thermal density operator:

$$\rho(0) = \rho_{eq} = \frac{1}{2}\left(\mathbf{1} - \frac{\hbar\omega_0}{k_B T} I_z\right) \rightarrow \rho(0) = I_z.$$

In polarization-transfer experiments involving nuclei *I* and *S* of different gyromagnetic ratios, the $\hbar\omega_0/k_B T$ factors have to be reintroduced. If experiment involves two spin species *S* and *I* of Larmor frequencies $\omega_{0S} = \gamma_S B_0$ and $\omega_{0I} = \gamma_I B_0$ we may write

$$\rho(0) = \rho_{eq} = \frac{1}{4}\left(\mathbf{1} - \frac{\hbar\omega_{0I}}{k_B T} I_z - \frac{\hbar\omega_{0S}}{k_B T} S_z\right) \rightarrow \rho(0) = \gamma_I I_z + \gamma_S S_z.$$

### 1.1.3 Nuclear Spin Interactions

The basic NMR picture introduced above has to be modified in order to take into account various interactions of the nuclear spins and their effect on the NMR spectra. This section introduces the mathematical description of various nuclear spin interactions [8,9,10] and the essential techniques for achieving spectral sensitivity and resolution in solid-state NMR experiments.

According to the discussion in the previous section, nuclear spins interact with external static and RF magnetic fields and the corresponding Hamiltonian is

$$\mathcal{H}_{ext} = \mathcal{H}_Z + \mathcal{H}_1$$

where $\mathcal{H}_Z = -\gamma \mathrm{B}_0 I_z = \omega_0 I_z$ and $\mathcal{H}_1 = -\gamma 2\mathrm{B}_1 I_x \cos(\omega t) = 2\omega_1 I_x \cos(\omega t)$. In the rotating frame, the time independent Hamiltonian representing the externally applied magnetic fields can be written as

$$\widetilde{\mathcal{H}}_{ext} \cong (\omega_0 - \omega) I_z + \omega_1 I_x.$$

Besides the interaction with external magnetic fields, nuclear spins interact among themselves or with the electronic environment. There exist several types of internal interactions, however the corresponding Hamiltonian can be always expressed in a given Cartesian coordinate system by means of a second rank tensor, $\overline{\overline{\boldsymbol{A}}}$, as

$$\mathcal{H}_{int} = \boldsymbol{U}.\overline{\overline{\boldsymbol{A}}}.\boldsymbol{V} = \left(U_x, U_y, U_z\right).\begin{pmatrix} A_{xx} & A_{xy} & A_{xz} \\ A_{yx} & A_{yy} & A_{yz} \\ A_{zx} & A_{zy} & A_{zz} \end{pmatrix}.\left(V_x, V_y, V_z\right) = \sum_{ij} A_{ij} T_{ij}, \qquad (1.15)$$

where $\boldsymbol{U}$ and $\boldsymbol{V}$ are vectors, which can be spin operators or a spin operator and an externally applied magnetic field, and $T_{ij} = U_i V_j$ [10-13]. The components of the tensor depend on the frame of reference, however it is always possible to specify a coordinate system in which the interaction tensor is diagonal. Such a coordinate system is named as the principal axis system (PAS) [10]. Rather than working with the Cartesian tensors $A_{ij}$ and $T_{ij}$ it is convenient to employ irreducible spherical tensors. The components of any Cartesian tensor of rank 2 can be expressed in terms of components of irreducible spherical tensors of rank 0 (scalar), 1(anti-symmetric) and 2 (symmetric). If $A_{kl}$ and $T_{kl}$ represent components of the spherical tensors connected to $A_{ij}$ and $T_{ij}$, the interaction Hamiltonian can be written as,

$$\mathcal{H}_{int} = \sum_{k=0}^{2} \sum_{l=-k}^{k} (-1)^l A_{kl} T_{k,-l}. \qquad (1.16)$$

The tensors $A_{kl}$ and $T_{kl}$ represent the spatial and the spin parts of the interaction Hamiltonian. The relation between Cartesian and spherical tensor components is given in the Table 1.1.

As we have seen in the previous section, description of the nuclear spin system is simplified in the rotating frame coordinate system. In the rotating frame an internal interaction becomes time-dependent according to

$$\tilde{\mathcal{H}}_{int} = e^{i\omega_0 I_z t}\mathcal{H}_{int}e^{-i\omega_0 I_z t} = \sum_{k=0}^{2}\sum_{l=-k}^{k}(-1)^l A_{kl}T_{k,-l}e^{il\omega_0 t}\ . \qquad (1.17)$$

**Table 1.1** Relationship between Cartesian and spherical components of spin and space part of a second rank tensor [19].

| | | | |
|---|---|---|---|
| $A_{00}$ | $-\frac{1}{\sqrt{3}}[A_{xx}+A_{yy}+A_{zz}]$ | $T_{00}$ | $-\frac{1}{\sqrt{3}}[U_xV_x+U_yV_y+U_zV_z]$ |
| $A_{10}$ | $-\frac{i}{\sqrt{2}}[A_{xy}-A_{yx}]$ | $T_{10}$ | $-\frac{i}{\sqrt{2}}[U_xV_y-U_yV_x]$ |
| $A_{1\pm1}$ | $-\frac{1}{2}[A_{zx}-A_{xz}\pm i(A_{zy}-A_{yz})]$ | $T_{1\pm1}$ | $-\frac{1}{2}[U_zV_x-U_xV_z\pm i(U_zV_y-U_yV_z)]$ |
| $A_{20}$ | $\frac{1}{\sqrt{6}}[3A_{zz}-A_{xx}-A_{yy}-A_{zz}]$ | $T_{20}$ | $\frac{1}{\sqrt{6}}[3U_zV_z-U_xV_x-U_yV_y-U_zV_z]$ |
| $A_{2\pm1}$ | $-\frac{1}{2}[A_{xz}+A_{zx}\pm i(A_{zy}+A_{yz})]$ | $T_{2\pm1}$ | $-\frac{1}{2}[U_xV_z+U_zV_x\pm i(U_zV_y+V_yU_z)]$ |
| $A_{2\pm2}$ | $-\frac{1}{2}[A_{xx}-A_{yy}\pm i(A_{xy}+A_{yx})]$ | $T_{2\pm2}$ | $-\frac{1}{2}[U_xV_x-U_yV_y\pm i(U_xV_y+U_yV_x)]$ |

When the interaction with external magnetic field is considerably larger than the internal interactions, the terms with $l \neq 0$ oscillate rapidly and their influence on the spin dynamics is insignificant. Thus, by neglecting terms with $l \neq 0$, in the lab or rotating frame Eq. (1.17) takes the form

$$\tilde{\mathcal{H}}_{int} \cong A_{00}^{L}T_{00} + A_{10}^{L}T_{10} + A_{20}^{L}T_{20}, \qquad (1.18)$$

where the superscript $L$ indicates that the components are in the lab frame. This is called the secular approximation and the terms in Eq. (1.18) are called secular terms [10-13]. Secular approximation is excellent for most internal interactions and typical static magnetic fields in the Tesla range. It can be shown that secular approximation amounts to keeping only those terms in $\tilde{\mathcal{H}}_{int}$ that commute with the Zeeman Hamiltonian. The irreducible tensor components in the lab frame, $A_{Jm}^{L}$, and in the PAS frame, $A_{Jm}^{PAS}$, are related by

$$A_{Jm}^{L} = \sum_{m'=-L}^{L} A_{Jm'}^{PAS}D_{m'm}(\alpha,\beta,\gamma), \qquad (1.19)$$

where $\alpha,\beta,\gamma$ are the Euler angles which relate the lab frame coordinate system to the PAS. The coefficients $D_{m'm}(\alpha,\beta,\gamma)$ are the Wigner rotation matrices [19]. This transformation is

used to express the space part of the Hamiltonian in terms of the irreducible tensor components in the PAS.

**Chemical Shift**: When a sample is introduced in a static magnetic field the electronic orbitals are slightly perturbed resulting in non-vanishing electronic current density around the nucleus. These electronic currents produce a very small magnetic field $\boldsymbol{B}_e$ at the nucleus and the nuclear spin couples to this field with a Zeeman-like Hamiltonian $-\boldsymbol{\mu B}_e$. This interaction causes a shift to the NMR precession frequency and is called the chemical shift interaction. The direction and magnitude of $\boldsymbol{B}_e$ depends on the electronic environment of the nucleus. For a nuclear spin $I$ placed in a static magnetic field $B_0$, the Hamiltonian representing the chemical shift interaction as per Eq. (1.15) is represented as [10]

$$\mathcal{H}_{CS} = -\gamma \boldsymbol{I}.\bar{\bar{\boldsymbol{\sigma}}}.\boldsymbol{B_0} \tag{1.20}$$

where $\bar{\bar{\boldsymbol{\sigma}}}$ is the chemical shift tensor which can be decomposed into irreducible spherical tensors of rank 0, 1 and 2. The chemical shift tensor is diagonal in the PAS, which is fixed with respect to the molecule. The rank 0 component corresponds to one third of the sum of the diagonal elements of $\bar{\bar{\boldsymbol{\sigma}}}$ in the PAS and is called the isotropic chemical shift. Under the secular approximation the rank 1 component does not contribute and rank 2 component represents the chemical shift anisotropy (CSA). The isotropic chemical shift is represented as

$$\sigma_{iso} = \frac{1}{3}(\sigma_{xx}^{PAS} + \sigma_{yy}^{PAS} + \sigma_{zz}^{PAS}). \tag{1.21}$$

The anisotropic part of the chemical shift is determined by two parameters, the chemical shift anisotropy $\Delta_{CS}$ and the asymmetry parameter $\eta$ defined as

$$\Delta_{CS} = \sigma_{zz}^{PAS} - \sigma_{iso}, \tag{1.22}$$

$$\eta = \frac{\sigma_{yy}^{PAS} - \sigma_{xx}^{PAS}}{\sigma_{zz}^{PAS} - \sigma_{iso}}. \tag{1.23}$$

Defining $\boldsymbol{U} = (I_x, I_y, I_z)$, $\boldsymbol{V} = -\gamma\left(B_{0x}, B_{0y}, B_{0z}\right)$, $\bar{\bar{\boldsymbol{A}}} = \bar{\bar{\boldsymbol{\sigma}}}$, and taking into account that $\sigma_{10}^{L} = 0$, the $\sigma_{00}^{L}$ and $\sigma_{20}^{L}$ components are $-\frac{1}{\sqrt{3}}\left[\sigma_{xx}^{L} + \sigma_{yy}^{L} + \sigma_{zz}^{L}\right]$ and $\frac{1}{\sqrt{6}}\left[2\sigma_{zz}^{L} - \sigma_{xx}^{L} - \sigma_{yy}^{L}\right]$ and $T_{00} = -\frac{1}{\sqrt{3}}[-\gamma I_z B_0]$, $T_{20} = \frac{1}{\sqrt{6}}[-2\gamma I_z B_0]$. The chemical shift Hamiltonian can be written as

$$\tilde{\mathcal{H}}_{CS} \cong \sigma_{00}^{L} T_{00} + \sigma_{20}^{L} T_{20}. \tag{1.24}$$

Expressing $\sigma_{00}^{L}$ and $\sigma_{20}^{L}$ in terms of the components in the PAS according to Eq. (1.19), if $\alpha, \beta, \gamma$ are the Euler angles which relate the lab frame coordinate system to the PAS, we obtain $\sigma_{00}^{L} = \sigma_{00}^{PAS} = -\sqrt{3}\sigma_{iso}$ and

$$\sigma_{20}^{L} = \sum_{m=-2}^{2} \sigma_{2m}^{PAS} e^{-im\alpha} d_{m0}(\beta) = \sqrt{\frac{3}{8}} \Delta_{CS} (3\cos^2\beta - 1 - \eta \sin^2\beta \cos(2\alpha)), \qquad (1.25)$$

where $d_{m0}$ is the reduced Wigner rotation matrix [19]. The resulting chemical shift Hamiltonian in the laboratory frame is

$$\mathcal{H}_{CS} = -I_z[\gamma B_0 \sigma_{iso} + \gamma B_0 \tfrac{\Delta_{CS}}{2} (3\cos^2\beta - 1 - \eta \sin^2\beta \cos(2\alpha))]. \qquad (1.26)$$

The Euler angles $\beta$ and $\alpha$ are in fact the polar angles $\theta$ and $\phi$ describing the direction of the static magnetic field in the PAS. From here onwards we use angles $\theta$ and $\phi$ such that

$$\mathcal{H}_{CS} = -I_z[\gamma B_0 \sigma_{iso} + \gamma B_0 \tfrac{\Delta_{CS}}{2} (3\cos^2\theta - 1 - \eta \sin^2\theta \cos(2\phi))]. \qquad (1.27a)$$

The chemical shift Hamiltonian can be written as

$$\mathcal{H}_{CS} = \omega_{CS}(\theta, \phi) I_z = \big(\omega_{ISO} + \omega_{CSA}(\theta, \phi)\big) I_z, \qquad (1.27b)$$

where the isotropic frequency, $\omega_{ISO} = -\gamma B_0 \sigma_{iso}$, is separated from the chemical shift anisotropy

$$\omega_{CSA}(\theta, \phi) = -\gamma B_0 \tfrac{\Delta_{CS}}{2} (3\cos^2\theta - 1 - \eta \sin^2\theta \cos(2\phi))]. \qquad (1.28)$$

Let us compute the time evolution of a nuclear spin under the chemical shift interaction in the rotating frame for which $\omega_0 = \omega$. The corresponding propagator can be written as

$$U(t, 0) = e^{-i\omega_{CS}(\theta,\phi) I_z t}$$

After the 90$^{o}$ excitation pulse the density operator is $\rho(0) = I_x$ and the density matrix at time *t* reads

$$\rho(t) = U(t, 0) I_X U(t, 0)^{+} = I_x \cos(\omega_{CS}(\theta, \phi) t) + I_y \sin(\omega_{CS}(\theta, \phi) t).$$

The corresponding signal can be written as

$$S'(t) = S'_X + iS'_Y = \mathrm{Tr}\big(I_x \rho(t)\big) + i\mathrm{Tr}\left(I_y \rho(t)\right) = A\,[\cos(\omega_{CS}(\theta, \phi) t) + i\sin(\omega_{CS}(\theta, \phi) t)]$$

$$= A e^{+i\omega_{CS}(\theta,\phi) t}, \qquad (1.29)$$

where $A$ is a constant. A given orientation $(\theta, \phi)$ corresponds to a given spectral component at frequency $\omega_{CS}(\theta, \phi)$. For a powder sample, the above signal has to be integrated over all possible orientations $(\theta, \phi)$, giving rise to

$$S(t) = \frac{1}{4\pi}\int_0^{2\pi}\int_0^{\pi} S'(t)\, sin\theta d\theta d\phi. \tag{1.30}$$

The powder pattern thus can be obtained by Fourier transforming the above Eq. (1.30). Since $\omega_{CS}$ is a continuous function of $(\theta, \phi)$ it follows that the spectrum will be confined to a certain frequency range and will exhibit a specific lineshape depending on parameters $\Delta_{CS}$ and $\eta$. Lineshapes simulated using SIMPSON (Simulation program for solid state NMR) [37] for $\eta = 0, 0.5,$ and 1 are shown in Figure 1.2. The lineshape corresponding to $\eta = 0$ (Figure 1.2(a)) is termed as *axially-symmetric* powder pattern.

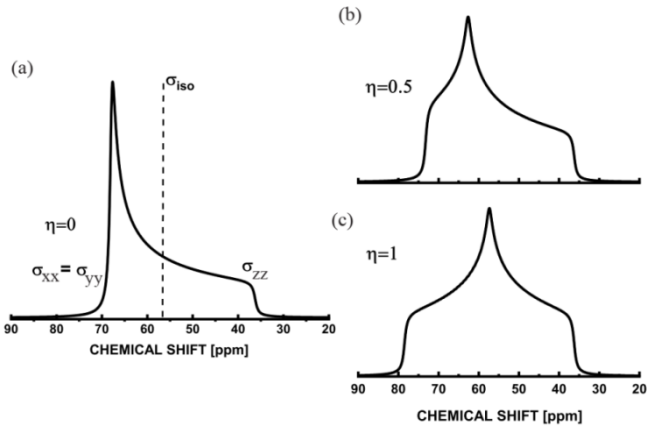


**Figure 1.2** Simulated powder spectra for $\eta$ values 0, 0.5, and 1.0. The time domain signal after a single $90^o$ pulse is Fourier transformed to get the resultant spectra shown in (a-c). The parameters used for simulation are, $\sigma_{iso} = 57$ ppm , $\Delta_{CS} = 21$ ppm , and the nucleus considered is $^{13}$C.

**Spin-Spin Interactions**

**(a) *J*-coupling**: This interaction is mediated through bonded electrons connecting any two nuclei in the sample. *J*-coupling results in spectral multiplicities of NMR resonances and is very useful for sequential assignment of solution-state NMR spectra. The anisotropic part of *J*-coupling interaction is very small and hence can be neglected. For a homonuclear $(I_i, I_j)$ spin pair, the bilinear *J*-coupling Hamiltonian can be written as,

$$\mathcal{H}_J^{II} = J_{ij}\boldsymbol{I_i}.\boldsymbol{I_j} = J_{ij}\left[I_z^i I_z^j + I_x^i I_x^j + I_y^i I_y^j\right] = J_{ij}\left[I_z^i I_z^j + I_+^i I_-^j + I_+^i I_-^j\right]. \quad (1.31)$$

This expression simplifies to

$$\mathcal{H}_J^{IS} = J_{IS} I_z S_z \quad (1.32)$$

for a heteronuclear $(I, S)$ spin pair. $J_{ij}/2\pi$ or $J_{IS}/2\pi$ is the *J*-coupling strength in frequency units. Typically *J*-coupling is in hundred Hz range or below. For example, a strong *J*-coupling exists, $J_{IS}/2\pi \cong 160\ Hz$, for a directly bonded $^{13}$C - $^{1}$H spin pair while usually $^{1}$H - $^{1}$H *J*-couplings are less than 10 Hz [8]. Since solid state NMR line widths are of the order of 100-1000 Hz, usually special NMR techniques are needed to retrieve *J*-coupling in solids [12]. The presence of the so called *flip-flop term*, $I_+^i I_-^j + I_+^i I_-^j$, in multi-spin systems is responsible for magnetization exchange between like spins [10].

**(b) Dipolar Interaction**: The magnetic dipole moment of a nucleus *i* creates a local magnetic field and the dipole moment of a neighbouring spin *j* interacts with this local magnetic field and results in shifting of the Zeeman energy levels [10]. The bilinear dipolar Hamiltonian can be obtained from classical electromagnetic theory as

$$\mathcal{H}_D = -\frac{\mu_0 \hbar \gamma_i \gamma_j}{4\pi r_{ij}^3}\left[3\frac{\left(\boldsymbol{I}_i.\boldsymbol{r}_{ij}\right)\left(\boldsymbol{I}_j.\boldsymbol{r}_{ij}\right)}{r_{ij}^2} - \boldsymbol{I}_i.\boldsymbol{I}_j\right], \quad (1.33)$$

where the classical magnetic dipole moment $\mu_j$ is replaced by its quantum-mechanical counterpart $\boldsymbol{\mu}_j = \hbar\gamma_j \boldsymbol{I}_j$ and $r_{ij}$ is the internuclear vector connecting the nucleus *i* and *j*. Using Eq. (1.15), the homonuclear dipolar Hamiltonian can be written as

$$\mathcal{H}_D = \boldsymbol{I_i}.\overline{\overline{\boldsymbol{D}}}.\boldsymbol{I_j} \quad (1.34)$$

where

$$\overline{\overline{\boldsymbol{D}}} = -\omega_D \begin{bmatrix} 3x_{ij}^2/r_{ij}^2 - 1 & 3x_{ij}y_{ij}/r_{ij}^2 & 3x_{ij}z_{ij}/r_{ij}^2 \\ 3y_{ij}x_{ij}/r_{ij}^2 & 3y_{ij}^2/r_{ij}^2 - 1 & 3y_{ij}z_{ij}/r_{ij}^2 \\ 3z_{ij}x_{ij}/r_{ij}^2 & 3z_{ij}y_{ij}/r_{ij}^2 & 3z_{ij}^2/r_{ij}^2 - 1 \end{bmatrix}$$

and dipolar coupling constant $\omega_D = \mu_0 \hbar \gamma_i \gamma_j / 4\pi r_{ij}^3$. The dipolar coupling tensor $\overline{\overline{\boldsymbol{D}}}$ is traceless and symmetric. For homonuclear dipolar interaction, $\gamma_i = \gamma_j = \gamma_I$, and in the lab frame the Hamiltonian can be expressed in terms of spherical tensors $A_{kl}$ and $T_{kl}$. Under

secular approximation the homonuclear dipolar Hamiltonian is given by Eq. (1.17). Since $A_{00}^L = 0$, $A_{10}^L = 0$, and

$$A_{20}^L = -\omega_D\sqrt{3/2}\,(3z_{ij}^2/r_{ij}^2 - 1),$$

$$T_{20} = \tfrac{1}{\sqrt{6}}(2I_{zi}I_{zj} - I_{xi}I_{xj} - I_{yi}I_{yj}),$$

the homonuclear dipolar Hamiltonian in the secular approximation is

$$\mathcal{H}_D = A_{20}^L T_{20} = -\omega_D \frac{(3\cos^2\theta - 1)}{2}\left[2I_{zi}I_{zj} - I_{xi}I_{xj} - I_{yi}I_{yj}\right], \tag{1.35}$$

where $\theta$ is the polar angle the internuclear vector $\boldsymbol{r}_{ij}$ makes with the applied magnetic field with $\omega_D = \mu_0\hbar\gamma_I^2/4\pi r_{ij}^3$.

After excitation with a 90$^o$ pulse the density operator of a homonuclear spin pair is $\rho(0) = I_{xi} + I_{xj}$. The density operator at time $t$ during detection is $\rho(t) = e^{-i\mathcal{H}_D t}\rho(0)e^{i\mathcal{H}_D t}$, and it can be shown that

$$\rho(t) = \left(I_{xi} + I_{xj}\right)\cos\left(\tfrac{3}{2}\omega_D' t\right) + 2(I_{yi}I_{zj} + I_{zi}I_{yj})\sin(\tfrac{3}{2}\omega_D' t) \tag{1.36}$$

The corresponding signal is

$$S(t,\theta) \propto Tr\{\rho(t)(I_{xi} + I_{xj})\} = \cos\left(\tfrac{3}{2}\omega_D' t\right) Tr\left\{\left(I_{xi} + I_{xj}\right)^2\right\} = 2\cos\left(\tfrac{3}{2}\omega_D' t\right) \tag{1.37}$$

where $\omega_D' = -\omega_D\,(3\cos^2\theta - 1)/2$ and we have taken into account that $Tr\{(I_{xi} + I_{xj})(I_{yi}I_{zj} + I_{zi}I_{yj})\} = 0$. Fourier transform of this signal results in a spectrum containing two peaks located at $\pm\frac{3}{2}\omega_D'$. In case of the powder, the signal has to be integrated over $\theta$ according to Eq. (1.30). Because of its dependence on $(3\cos^2\theta - 1)$, the spectrum of a dipolar-coupled spin pair in a powder display a characteristic lineshape termed as *Pake pattern* [10,11]. A simulated dipolar spectrum is shown in Figure 1.3. For a heteronuclear spin pair $I - S$, the secular dipolar Hamiltonian simplifies to

$$\mathcal{H}_D^{IS} = -\omega_D^{IS}\frac{(3\cos^2\theta - 1)}{2}2I_zS_z,$$

$$\omega_D^{IS} = \frac{\mu_0\hbar\gamma_I\gamma_S}{4\pi r_{IS}^3}\,. \tag{1.38}$$

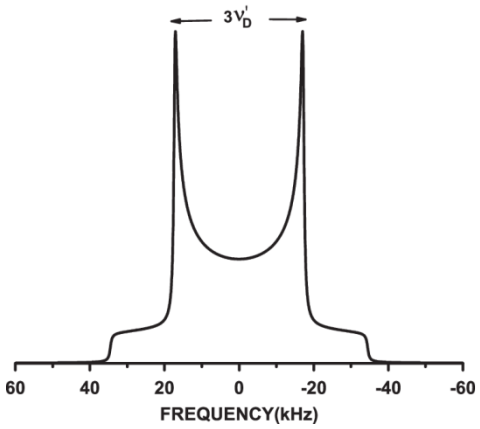


**Figure 1.3** Simulated homonuclear dipolar *Pake pattern* corresponding to protons in a rigid $CH_2$. The distance between two protons is 1.74 Å which provides a dipolar coupling strength of $\omega'_D/2\pi = \nu'_D = 23$ kHz. The spectrum was simulated using SIMPSON program.

After 90$^o$ excitation pulse of the S spin, the density operator is $\rho(0) = S_x$, and it can be shown that the density operator at time *t* during detection of the *S* spin is

$$\rho(t) = S_x \cos(\omega'_D t) + 2S_y I_z \sin(\omega'_D t) \qquad (1.39)$$

where $\omega'_D = -\omega_D^{IS}(3\cos^2\theta - 1)/2$. Fourier transform of this signal results in a spectrum containing two peaks located at $\pm\omega'_D$ and in a powder the spectrum is again a *Pake pattern*.

We can see from the Eq. (1.39) that the strength of the dipolar interaction depends on the gyromagnetic ratio's of the coupled nuclei and is inversely proportional to the cube of the distance of separation between them. Therefore the *Pake pattern* provides valuable structural information as it is directly associated with the distance of separation between the interacting spins. To appreciate the magnitude of the dipolar interaction, if we consider two protons separated by a distance of 1 Å, the dipolar interaction strength is about 121 kHz, whereas for the same distance and for a $^1$H-$^{13}$C spin pair, the magnitude reduces to 30 kHz as $\gamma_H/\gamma_C = 4$. For a $^2$H-$^{13}$C spin pair, it further reduces to 4.6 kHz as $\gamma_H/\gamma_{2H} = 6.5$. In real samples, the closest distance between two protons is larger than 1 Å, for example in $CH_2$ it is 1.74 Å, which provides a dipolar coupling strength of about 23 kHz. Similarly for a CH pair, the closest internuclear distance is 1.1 Å leading to dipolar interaction strength of 22.7 kHz. In practice, since one nuclear spin is dipolar coupled to several other nuclear spins, *Pake patterns* are rarely observed experimentally. This problem is especially severe in samples containing protons as protons form a strong dipolar-coupled network [11]. Due to the proton dipolar network also simple CSA powder patterns for the rare spins (eg. $^{13}$C, $^{15}$N, $^{29}$Si etc.)

are difficult to obtain. Extracting information on chemical shift and dipolar couplings in solids demand more complex pulse techniques [11,12].

At this point, it is worth mentioning that the homonuclear dipolar Hamiltonian contains a flip-flop term, $I_+^i I_-^j + I_+^i I_-^j$, which is responsible for spin-diffusion in solids.

**Quadrupolar Interaction:** More than 70% of NMR active nuclei have nuclear spin $I \geq 1$, and they possess a nuclear electric quadrupolar moment $eQ$, where $e$ is the charge of the electron. Nuclear quadrupole moment is due to the fact that electric charge distribution inside the nucleus is not spherically symmetric. The interaction between the quadrupolar moment and electric field gradient tensor (EFG) $\overline{\overline{\boldsymbol{V}}}$ arising from the electronic environment [11], results in quadrupolar interaction Hamiltonian,

$$H_Q = \boldsymbol{I}.\overline{\overline{\mathbf{Q}}}.\boldsymbol{I} \tag{1.40}$$

where $\overline{\overline{\boldsymbol{Q}}}$ is the quadrupolar interaction tensor, and is related to $\overline{\overline{\boldsymbol{V}}}$ via the nuclear electric quadrupolar moment as,

$$\overline{\overline{\mathbf{Q}}} = [\mathrm{eQ}/2\mathrm{I}(2\mathrm{I}-1)\hbar]\,\overline{\overline{\boldsymbol{V}}}. \tag{1.41}$$

Irrespective of the coordinate system, the tensor $\overline{\overline{\boldsymbol{V}}}$ is symmetric $\overline{\overline{\boldsymbol{V}}}_{ij} = \overline{\overline{\boldsymbol{V}}}_{ji}, (i,j = x,y,z)$ and traceless, $\{V_{xx} + V_{yy} + V_{zz}\} = 0$. Defining $\boldsymbol{U} = (I_x, I_y, I_z)$, $\boldsymbol{V} = (I_x, I_y, I_z)$, $\overline{\overline{\boldsymbol{A}}} = \overline{\overline{\mathbf{Q}}}$, we construct the corresponding spherical tensor components needed for the secular approximation, using Eq. (1.18). We find that $\mathrm{Q}_{00}^L = 0$, $\mathrm{Q}_{10}^L = 0$, and $\mathrm{Q}_{20}^L = \sqrt{3/2}\,\mathrm{Q}_{zz}^L$, $T_{20} = 1/\sqrt{6}\left[3I_z^2 - I_x^2 - I_y^2 - I_z^2\right] = 1/\sqrt{6}\ [3I_z^2 - I(I+1)]$. Hence the quadrupolar Hamiltonian in the secular approximation takes the form

$$\mathcal{H}_Q = \mathrm{Q}_{20}^L T_{20} = \frac{\mathrm{Q}_{20}^L}{\sqrt{6}}[3I_z^2 - I(I+1)]. \tag{1.42}$$

If the PAS frame is obtained by a rotation of the LAB frame characterized by Euler angles $\alpha, \beta, \gamma$

$$\mathrm{Q}_{20}^L = \sum_{m=-2}^{2} \mathrm{Q}_{2m}^{PAS} e^{-im\alpha} d_{m0}(\beta). \tag{1.43}$$

In the PAS the relevant spherical tensor components are $\mathrm{Q}_{2,-2}^{PAS} = \mathrm{Q}_{2,2}^{PAS} = -\frac{1}{2}(\mathrm{Q}_{xx}^{PAS} - \mathrm{Q}_{yy}^{PAS})$, $\mathrm{Q}_{2,-1}^{PAS} = \mathrm{Q}_{2,1}^{PAS} = 0$, and $\mathrm{Q}_{20} = \sqrt{3/2}\mathrm{Q}_{zz}^{PAS}$. Taking into account the Wigner matrix elements,

$$\mathrm{Q}_{20}^{L} = \sqrt{3/8}\mathrm{Q}_{zz}^{PAS}[3\cos^2\beta - 1 - \eta\sin^2\beta cos2\alpha],$$

where the asymmetry parameter $\eta = \left[\mathrm{Q}_{yy}^{PAS} - \mathrm{Q}_{xx}^{PAS}\right]/\mathrm{Q}_{zz}^{PAS} = \left[V_{yy}^{PAS} - V_{xx}^{PAS}\right]/V_{zz}^{PAS}$, and the secular quadrupolar Hamiltonian becomes

$$\mathcal{H}_Q = \frac{\omega_Q}{4}[3\cos^2\beta - 1 - \eta\sin^2\beta\cos 2\alpha][I_z^2 - I(I+1)/3]$$

with $\omega_{\mathrm{Q}} = 3e\mathrm{Q}V_{zz}^{PAS}/2I(2I-1)\hbar$ is the quadrupolar angular frequency. The quadrupolar coupling constant is, $C_Q = e^2Qq/\hbar = V_{ZZ}^{PAS}eQ/\hbar$, where $eq = V_{ZZ}$ represents the z component of the EFG tensor in the quadrupolar PAS. The Euler angles $\beta$ and $\alpha$ are in fact the polar angles $\theta$ and $\phi$ of describing the direction of the static magnetic field in the PAS. From here onwards we use angles $\theta$ and $\phi$ such that

$$\mathcal{H}_Q = \frac{\omega_Q}{4}[3\cos^2\theta - 1 - \eta\sin^2\theta\cos 2\phi][I_z^2 - I(I+1)/3]. \qquad (1.44a)$$

In order to calculate the signal after a $90^{\mathrm{o}}$ pulse, the density operator has to be evaluated at time t during detection. If $I = 1$ it can be shown that

$$\rho(t) = e^{-i\mathcal{H}_Q t}I_x e^{i\mathcal{H}_Q t} = I_x\cos(\omega_Q' t) + \left[I_yI_z + I_zI_y\right]\sin\left(\omega_Q' t\right),$$

where

$$\omega_Q' = \frac{\omega_Q}{4}[3\cos^2\theta - 1 - \eta\sin^2\theta\cos 2\phi]. \qquad (1.44b)$$

The corresponding signal is

$$S(t,\theta,\phi) \propto Tr\{\rho(t)I_x\} = \cos\left(\omega_Q' t\right)Tr\{I_x^2\} = 2\cos\left(\omega_Q' t\right). \qquad (1.45)$$

Fourier transform of this signal results in a spectrum containing two peaks of equal intensities located at $\pm\omega_Q'$. Since a powder spectrum is a summation over crystallite orientation it follows that the powder spectrum is also symmetric. In case of the powder, the signal has to be integrated over $\theta$ and $\phi$ according to Eq. (1.30). Because of the dependence of $\omega_Q'$ on $\theta$ and $\phi$, the spectrum of a quadrupolar spin in a powder display a characteristic lineshape. The span of the spectrum depends on $\omega_Q$ whereas the lineshape depends on $\eta$ as illustrated in Figure 1.4.

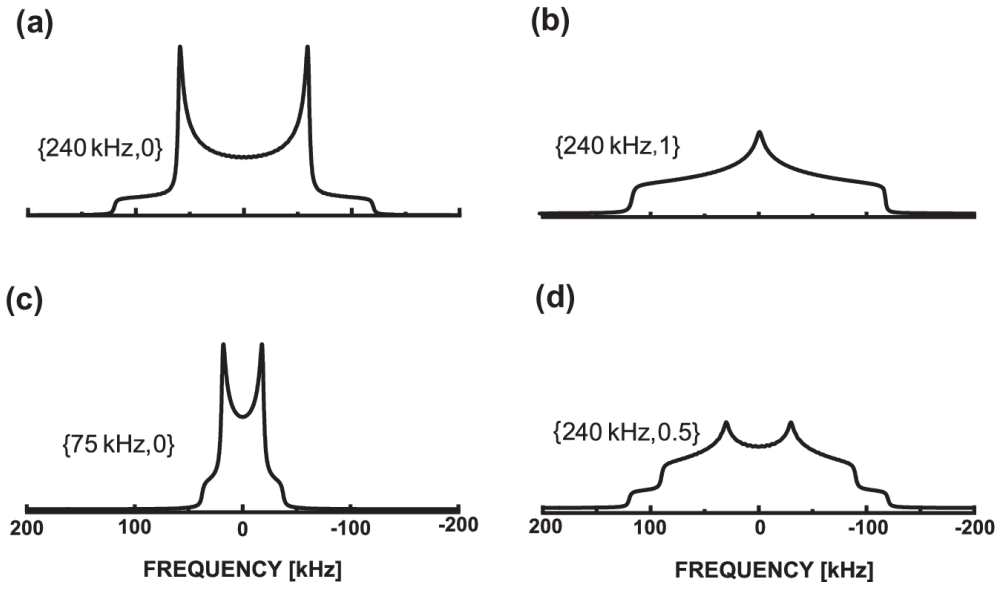


**Figure 1.4** SIMPSON simulated spectra of $^2$H nucleus with different $\nu_Q = \omega_Q/2\pi$ and $\eta$.

The secular Hamiltonian given in Eq. (1.44a) constitutes an excellent approximation if $\omega_Q$ is sufficiently small in comparison to $\omega_0$, like in deuterium ($^2$H, $I$=1) where the maximum quadrupolar coupling strength is of the order of 260 kHz while $\nu_0 \cong 92\ MHz$ for 600 MHz NMR spectrometer. $^2$H has low gyromagnetic ratio and low natural abundance hence requires isotopic enrichment which is costly. Another spin-1 quadrupolar nucleus with 99% natural abundance and present in all amino-acids and proteins is $^{14}$N. The $^{14}$N quadrupolar coupling is within 1-5 MHz and a correction called the second-order quadrupolar interaction has to be added to Eq. (1.44a). For quadrupolar coupling constants in the MHz range the second-order quadrupolar interaction is in the kHz range. For half-integer nuclear spins the signal can be divided into two contributions. Part of it arises from coherences involving states $|1/2\rangle$ and $|-1/2\rangle$ (the so called central transition). These coherences are affected by second-order quadrupolar interaction but are not affected by the first order quadrupolar interaction; hence the central transition lineshapes spans only a few kHz. All other coherences contributing to signal (e.g. coherences involving states $|3/2\rangle$ and $|1/2\rangle$ termed as satellite transitions) are affected by first order quadrupolar interaction and the corresponding lineshapes are much broader, from hundreds of kHz up to a few MHz. As a result the NMR spectrum of half-integer nuclear spins is dominated by the central transition [12,13]. Experiments and theoretical methods specifically designed for quadrupolar nuclei are under constant development and have enriched the field of solid state NMR [11,12]. A few

commonly occurring and widely studied half integer quadrupolar nuclei in the solid state are $^{7}$Li (I=3/2), $^{27}$Al (I=5/2), $^{23}$Na (I=3/2) etc.

### 1.1.4 Sensitivity Enhancement Techniques

**Magic angle spinning (MAS)**: The nuclear spin interactions described above are anisotropic, thus orientation dependent, hence spectra acquired in polycrystalline samples are broad. This results in poor resolution and sensitivity of the NMR spectrum when compared with solution NMR. Powder spectra are rich in structural information, but information is hard to retrieve due to lack of sensitivity and resolution.

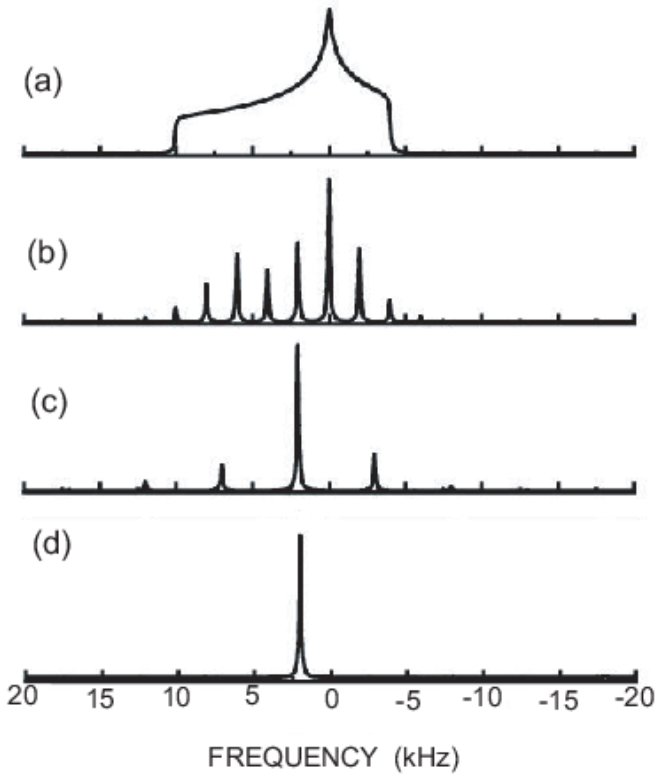


**Figure 1.5** SIMPSON simulated spectra showing the effect of MAS on the anisotropic line shape due to chemical shift interaction at (a) static case and various MAS rates, (b) $\nu_R$ = 2 kHz, (c) 5 kHz, and (d) 10 kHz. The parameters considered corresponds to a $^{13}$C nucleus, with $\sigma_{iso} = 2$ kHz and $\Delta_{CS} = 8$ kHz.

Therefore for solid samples requirement of high resolution spectra enabling sensitivity and resolution is a necessity. As discussed before, all interaction Hamiltonians have a spatial part, $A_{kl}$, and a spin part, $T_{kl}$. By careful manipulation of the anisotropic spatial part, high resolution solid state NMR spectra can be achieved. One of the important and widely used techniques to remove the orientation dependent anisotropy in polycrystalline samples is to

rapidly spin the sample at an angular frequency $\omega_R$, about an axis inclined at 54.7$^o$, termed as magic angle, with respect to the applied magnetic field [14-16]. Due to MAS the spatial part of the spin Hamiltonian becomes time-dependent and the anisotropic part is averaged out, resulting in high resolution NMR spectra.

When the sample is spun, PAS changes its orientation periodically with respect to the lab frame, rendering the spatial part of the interaction Hamiltonian time-dependent [17]. The chemical shift Hamiltonian given in Eq. (1.27a) becomes time-dependent as

$$\mathcal{H}_{CS}(t) = \omega_{CS}(\alpha,\beta,\gamma;t)I_z = \big(\omega_{ISO} + \omega_{CSA}(\alpha,\beta,\gamma;t)\big)I_z =$$

$$\omega_{ISO}I_z + \gamma B_0 \frac{\Delta_{CS}}{2}[C_1\cos(\omega_R t+\gamma) + C_2\cos(2\omega_R t+2\gamma) + S_1\sin(\omega_R t+\gamma) + S_2\sin(2\omega_R t+2\gamma)]I_z.$$

$$C_1 = -\sqrt{2}\sin 2\beta(1+\tfrac{\eta}{3}\cos 2\alpha);\ C_2 = \sin^2\beta - \tfrac{\eta}{6}(1+\cos^2\beta)\cos 2\alpha;$$

$$S_1 = \tfrac{\eta}{3\sqrt{2}}\sin\beta\sin 2\alpha\ ;\ S_2 = \tfrac{2}{3}\eta\cos\beta\sin 2\alpha$$

where $\alpha,\beta,\gamma$ are the Euler angles corresponding to rotation from rotor frame to the PAS frame. Since the Hamiltonian is commuting with itself at different times, the propagator is

$$U(t,0) = \exp\left(-i\int_0^t \mathcal{H}_{CS}(t')dt'\right) = \exp\left(-iI_z\int_0^t \omega_{CS}(\alpha,\beta,\gamma;t')dt'\right).$$

For a given crystallite orientation, the evolution of the density matrix in the rotating frame and after 90$^o$ excitation can be written as

$$\rho(t,0) = U(t,0)I_X U(t,0)^+ = I_X\cos\left(\int_0^t \omega_{CS}(\alpha,\beta,\gamma;t')dt'\right) + I_Y\,sin\left(\int_0^t \omega_{CS}(\alpha,\beta,\gamma;t')dt'\right).$$

It can be shown that

$$\exp\left(i\int_0^t \omega_{CS}(\alpha,\beta,\gamma;t')dt'\right) = e^{i\omega_{ISO}t}\sum_{n=-\infty}^{\infty} I_n(\alpha,\beta,\gamma)\,e^{in\omega_R t}.$$

This is an infinite series of terms oscillating at $n\omega_R$ of amplitude $I_n$ [10]. The signal for a given crystallite orientation is

$$S(\alpha,\beta,\gamma,t) = Tr\big(I_X\rho(t)\big) + iTr\big(I_Y\rho(t)\big) = e^{i\omega_{ISO}t}\sum_{n=-\infty}^{\infty} I_n(\alpha,\beta,\gamma)\,e^{in\omega_R t}. \qquad (1.46)$$

The signal from a powder sample can be calculated as

$$S(t) = \frac{1}{8\pi^2} \int_0^{2\pi} d\alpha \int_0^{\pi} sin\beta d\beta \int_0^{2\pi} S(\alpha, \beta, \gamma, t) d\gamma \,.$$

From Eq. (1.46) it can be seen that the spectrum for a single crystallite orientation consists of a centre-band positioned at the isotropic frequency $\omega_{ISO}$, and spinning sidebands placed symmetrically at frequencies $\omega_{ISO} + n\omega_R$. This holds also for a powder and in addition Fourier transform of $S(t)$ result in sharp spinning sidebands that are in-phase with respect to each other [11]. If spinning frequency $\nu_R$ (Hz) is considerably less than the anisotropy, spinning sidebands occur within the width of the corresponding static spectrum, as shown in Figure 1.5. With increasing spinning frequency, the intensities of the sidebands decrease and at spinning frequencies comparable to or larger than the chemical shift anisotropy the spectrum consists of a single line appearing at the isotropic frequency $\omega_{ISO}$, as illustrated in Figure 1.5(d). Though MAS results in high resolution solid state NMR spectra, the information on anisotropic interactions, which depends on molecular structure, is lost. Nevertheless, by spinning slow or by using specially designed pulse techniques for reintroducing these interactions (termed as recoupling sequences) [12,13], structural information can be retrieved selectively. Thus MAS together with multi-dimensional experiments that correlate various interactions and selectively reintroduce anisotropic interaction has become the state-of-art in solid state NMR for deriving structural information. A detailed derivation of the intensity of the sidebands and the time-dependent Hamiltonian corresponding to chemical shift anisotropy can be found in the literature [10].

**Deuterium MAS NMR:** In the context of deuterium NMR, referring to Eq. (1.44a) in section 1.1.3, static quadrupolar Hamiltonian under MAS becomes [10,11],

$$\mathcal{H}(t) = \omega_Q f(t)[I_z^2 - I(I+1)/3] \,, \qquad (1.47)$$

where for $\eta = 0$,

$$f(t) = \left[\frac{1}{4}\sin^2(\beta) cos(2\omega_R t + 2\gamma) - \frac{1}{2\sqrt{2}}\sin(2\beta)\cos(\omega_R t + \gamma)\right],$$

and $\beta$ and $\gamma$ are the polar angles of the Z axis of the quadrupolar PAS with respect to the rotor frame. For $I = 1$ the quadrupolar frequency $\omega_{\mathrm{Q}} = 3e\mathrm{Q}V_{zz}^{PAS}/2I(2I-1)\hbar$ is related to quadrupolar coupling constant as $C_Q = \frac{2}{3}\omega_Q$. Since $[\mathcal{H}(t), \mathcal{H}(t')] = 0$ the propagator can be written as

$$U(t,0) = \exp\left(-i[I_z^2 - I(I+1)/3]\int_0^t \omega_Q f(t')dt'\right)$$

and, similarly to the static case,

$$\rho(t) = U(t,0)I_x U(t,0)^+ = I_x \cos(\phi_Q(t,0)) + \left[I_y I_z + I_z I_y\right]\sin(\phi_Q(t,0)),$$

where

$$\phi_Q(t,0) = \int_0^t \omega_Q f(t')dt'.$$

The corresponding signal is

$$S(t,\theta,\phi) \propto Tr\{\rho(t)I_x\} = \cos\left(\phi_Q(t,0)\right) Tr\{I_x^2\} = 2\cos\left(\phi_Q(t,0)\right).$$

Similar to the chemical shift anisotropy

$$\cos\left(\phi_Q(t,0)\right) = \sum_{n=-\infty}^{\infty} I_n(\beta,\gamma)\, e^{in\omega_R t}.$$

The corresponding spectrum consists of sidebands located at $n\omega_R$.

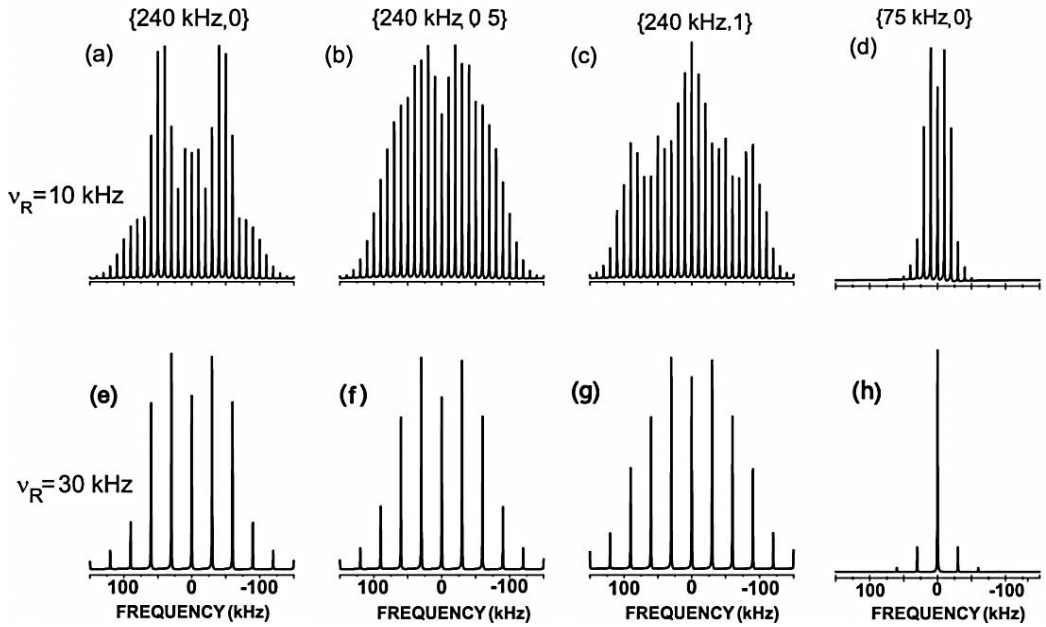


**Figure 1.6** SIMPSON simulated spectra showing the effect of MAS on anisotropic lineshape with different $\{\nu_Q, \eta\}$, for $\nu_R = 10$ kHz and $\nu_R = 30$ kHz. The quadrupolar parameters are indicated in the figure.

For a powder the relative intensities of the sidebands depend on $\nu_Q$, $\eta$, and $\omega_R$. Thus, analysis of experimental spinning-sideband patterns can lead to the quadrupolar parameters $\nu_Q$ and $\eta$. A few deuterium MAS NMR spectra, simulated using SIMPSON with different quadrupolar parameters, at two different MAS rates are shown in Figure 1.6. It can be seen that spectral

features are altered with change in MAS rates. Comparison of experimental and simulated spectra provides the quadrupolar parameters. This best-fit procedure is reliable only when there are no molecular dynamics present in the system. With molecular dynamics, the spectral features become more complex, suiting the nature of dynamics. Numerous motional models and computational schemes have been proposed and developed over decades in order to understand molecular dynamics and its impact on deuterium MAS NMR spectra [11]. A description of dynamic modulated deuterium MAS NMR spectra is given in section 1.3.

**Proton MAS NMR:** Proton solid state MAS NMR spectra consist of broad centre band and sidebands, similar to Figure 1.5. The spin Hamiltonian contains pairwise dipolar terms besides the Zeeman interaction:

$$\mathcal{H}(t) = \sum_i \omega_0^i I_z^i + \sum_{\substack{i,j \\ i \neq j}} \omega_D^{ij}(t)\left(2I_z^i I_z^j - I_x^i I_x^j - I_y^i I_y^j\right).$$

Dipolar terms corresponding to different proton spin pairs do not commute with each other at different times, thereby resulting in broad features in the proton MAS NMR spectra. As a consequence distinct proton chemical shifts $\omega_0^i$ are not resolved for most rigid samples at

MAS rates below 30 kHz. With the introduction of ultra-fast MAS ($\nu_R > 60$ kHz) well resolved proton spectra can be achieved especially for small molecules [38-41]. A partial narrowing of the broad proton MAS spectra NMR occurs when molecular motion is present. This is detailed in section 1.2 and in chapters 2 and 3. MAS NMR spectra of other nuclei ($S$) in samples containing proton dipolar network also exhibit broad centre band and sidebands hindering resolution of different chemical shifts. This broadening is a consequence of the fact that the $I - S$ heteronuclear and $I - I$ proton homonuclear dipolar terms do not commute at different times. The broadening can be removed by irradiating the protons during the detection of $S$ nuclear spins. This technique is known as heteronuclear decoupling [23] and currently there exists several efficient irradiation schemes in solid state MAS NMR [42-45]. Heteronuclear decoupling has become an integral part of many solid state NMR experiments, for example experiments involving $^{13}$C and/or $^{15}$N etc.

**Cross Polarization (CP)**: Direct 90$^o$ pulse excitation and detection of dilute or rare nuclei, which in addition may have low gyromagnetic ratio, suffer from low signal-to-noise ratio (SNR). In an NMR experiment the excitation-detection scheme is performed several times and signals from individual scans are added in order to enhance the signal-to-noise ratio [6].

The inter-scan delay ensures that excited nuclear spins relax back to equilibrium before beginning of the next scan. Longer longitudinal relaxation times lead to large inter-scan delays (100's of seconds to hours) and hence increased experimental times. Increase in SNR of low-abundance and/or low gyromagnetic ratio spins can be obtained by cross polarization [20], a widely used technique in solid state NMR. CP initiates polarization transfer from abundant (*I*) spins (typically $^{1}$H) to dilute or rare spins *S* (e.g. $^{13}$C), the signal of which is subsequently detected.

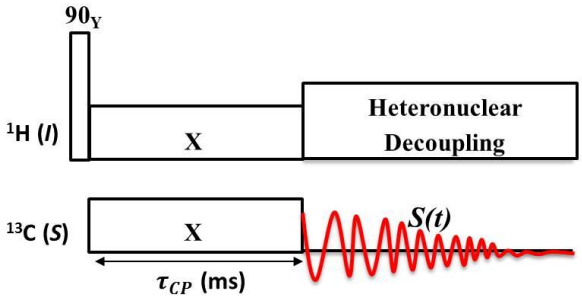


**Figure 1.7** Schematic of a cross polarization pulse sequence. CP contact time is shown as $\tau_{CP}$.

In CP experiments magnetization transfer is mediated through the *I*-*S* dipolar interaction. The CP pulse sequence (Figure 1.7) starts with a 90$^{o}$(Y) excitation pulse on *I* spins which tilts the *I*-spin magnetization to the X axis. Subsequently *on-resonance* RF irradiation of strength $\nu_{1I}$ and phase X is applied on the *I* spins for a duration $\tau_{CP}$. Simultaneously RF irradiation of strength $\nu_{1S}$ is applied on the *S* spins. Polarization transfer occurs during $\tau_{CP}$ when the *I* and *S* RF strengths satisfy the so-called Hartmann-Hahn matching condition [20-22]. For CP experiments on static samples Hartmann-Hahn matching condition is

$$\nu_{1I} = \nu_{1S} \tag{1.48}$$

Theoretically, CP provides a sensitivity enhancement of *S* spins by a factor of $\gamma_I/\gamma_S$ when compared with single pulse excitation. We have seen in the previous section that MAS averages the dipolar interaction. Since CP is mediated through heteronuclear dipolar interaction, in order to reinstate polarization transfer under MAS, the dipolar interaction needs to be recoupled. This is achieved by modifying the matching condition given in Eq. (1.48) as below,

$$\nu_{1I} = \nu_{1S} \pm n\nu_R, \tag{1.49}$$

with $n = 1, 2$. Since dipolar couplings are stronger for shorter internuclear distances and are also averaged by molecular dynamics, by tuning the duration of $\tau_{CP}$, CP can be used to selectively polarize nuclear spins at certain chemical sites of interest in both static and non-spinning samples. The basic CP/CPMAS pulse sequence has been developed over years in-order to ensure uniform and efficient polarization transfer for a broad range of chemical shifts or offsets [46-48]. Due to high selectivity and sensitivity, CP/CPMAS has become an important element of many solid state NMR experiments. Wherever suitable, we have employed CPMAS to obtain structural characteristics of the materials under study.

## 1.2 Mesoporous Materials

This section provides a general introduction about the properties of materials employed in this study. Description of mesoporous materials, their synthesis and characterization, properties of water molecules under confinement within the pores of these materials studied by NMR, are discussed. A brief overview of recent literature employing solid state NMR to study properties and characteristics of these materials is also furnished.

Material science witnessed a breakthrough in 1992 by Mobil Corporation laboratory, with the discovery of mesoporous materials, the M41S silicates [49]. Since then, the field has undergone impressive progress in the development of new mesoporous materials based on different synthesis conditions. Depending on the composition of materials used for synthesis, the properties of synthesised materials differ from those of M41S. Mesoporous materials can be classified as silica based and otherwise. Silicon-based mesoporous materials are termed as mesoporous silicates and all others are termed as non-siliceous mesopores. Mesoporous nanoparticles have ordered cylindrical pores with tunable range of pore diameters. According to International Pure and Applied Chemistry, the pore diameters of mesoporous silicate materials range within $2.0 - 50$ nm. The family of M41S materials composed of amorphous silica network, have large channels from 1.5 to 10 nm, ordered in hexagonal (Mobil Crystalline Materials: MCM-41), cubic (MCM-48), and laminar (MCM-50) arrays [49-52]. Their long-range order, large surface area >700 $m^2/g$, high thermal, hydrothermal, and chemical stability made them potential candidates for adsorption, catalysis and various other biotechnology applications. Following M41S materials, other type of mesoporous silica materials were synthesized such as SBA-15 (Santa Barbara Amorphous) [50] with hexagonal array of pores, and larger pore size ranging within 4.6 – 30 nm.

MCM-41 and SBA-15 are considered as potential materials for controlled drug release because of properties such as hexagonal ordered structure, high surface area and non-cytotoxic properties. When synthesised below 130 $^{o}$C, pore structures studied using X-ray diffraction, high-resolution transmission electron microscopy, etc. revealed microscopic differences between these two materials [51-64]. In SBA-15, as revealed by $^{129}$Xe NMR [53,54], the hexagonal mesopores are inter-connected by micropores, which facilitate adsorption at very low concentration when compared with MCM-41 where these channels remain unconnected. Thicker silica pore walls in SBA-15 provide higher thermal stability under irradiation with high energy electron beams in comparison with MCM-41 [55,57-59]. To conclude, the micropore - mesopore structure in SBA-15 has a strong influence on facile desorption, fast adsorption kinetics, its efficacy in different catalytic transformation reactions and so on, thereby providing a vast scope of molecular engineering of the silica surface through surface functionalization [60-64]. A large percentage of SBA-15 (MCM-41) framework consists of –Si-O-Si linkage, termed as siloxanes, which are hydrophobic (Figure 1.8) [65]. Inner pore walls or surface have germinal, vicinal silanols, or isolated (free) silanols, which are hydrophilic. Increasing the concentration of hydroxyl groups is essential as they interact with other chemical species, aiding in adsorption and functionalization. Therefore, synthesis and calcination is carried out at different temperatures and at various pH levels, in order to tune the micropore - mesopore structure, silanol concentration etc.

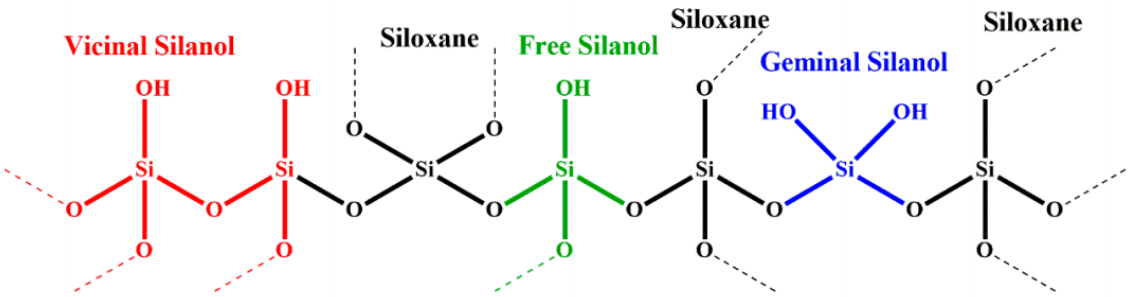


**Figure 1.8** Silicon-oxygen types present in SBA-15 (taken from Ref. [65]).

Subsequently, additional efforts were invested in enhancing the functionality of mesoporous silica materials by expanding the framework composition. Compatibility of functionality was broadened by the development of hybrid organic-inorganic mesoporous interfaces [66-69]. In 1999, Ozin et al., Inagaki et al. and Stein et al. independently developed a novel class of materials known as periodic mesoporous organosilicates (PMOs) with

varying pore size in 2 - 30 nm range [66-69]. In PMO's the organic bridge (-R-) is situated within the channel as (-Si-O-Si-R-Si-O-Si-) [70]. These bridged mesoporous materials were further developed to form xerogels and aerogels of increased transparency and porosity. These materials are of light weight due to increased porosity. This extended their applications as matrices for growing metal semiconductor nano-clusters, in optical applications such as waveguides and laser etc. The organic-inorganic bridges in PMO's permit tuning of hydrophilicity, hydrophobicity, and adsorption of guest molecules resulting in modification of bulk properties [70].

Surface polarity influences adsorption and hence the catalytic activity of these materials. In certain cases, by changing chemical composition of the catalyst, polarity can be changed. Other major factors that affect the polarity and morphology of the mesoporous material are: the extent of confinement of guest molecules, number density of active sites, and the features of these active sites [71-75]. For possible catalytic application, one has to understand the transport phenomena of confined guest molecules which need efficient transport channels in and out of the silica channels. Efficiency of catalysis is closely related to transport phenomena as they allow the guest molecules to react and leave the surface afterwards. The peculiar features of these materials have triggered several studies to understand dynamics of molecules near mesoporous silica surfaces [76-79].

Insight on the features of mesoporous materials and the dynamics of confined guest molecules or functionalized molecules is hence essential to understand the functions of these materials. We have focused our study on two important molecular sieves in this thesis, SBA-15, with and without functionalization, and periodic mesoporous organosilicates with ethane as organic bridge ($PMO_E$) [80].

### 1.2.1 Synthesis and Characterization of Mesoporous Materials

Synthesis of mesoporous materials involves two branches of chemistry, sol-gel and micelle chemistry [52,52,56,57,70,73,75]. The template used for synthesis is liquid crystalline self-assembled surfactant molecules. Due to the large scale industrial applications of these materials, the hydrothermal and mechanical stability are critical. Therefore, up to now there are many publications in the literature which offer different synthesis mechanisms, investigates the cooperative assembly of micelles and silicates, optimize the synthesis conditions and physical properties. Various synthesis methods have been established using bridged organosilica precursors, by incorporating a large variety of organic moieties, from

simple bridges containing methylene, ethylene, phenylene, etc., to long hydrocarbon chains containing N, S or O, metal complexes, and so on [75]. Apart from synthesis of the materials used in the work, a few important synthesis mechanisms and their outcome, are listed in the references and will not be discussed further [71-88].

Several methods are used to characterize these materials in terms of adsorption, surface properties, and structure [52,53,56,61,63,66,70,74,77]. Surface functionality is usually studied by a combination of techniques such as, elemental analysis, Fourier transform infrared spectroscopy (FTIR) [56,57,70], solid state NMR [85-88], thermogravimetry and adsorption [62,71,78]. Surface area, mean pore size, pore connectivity, surface heterogeneity, and mean pore volume are provided by the gas ($N_2$, $O_2$, Ar) adsorption technique [89]. Pore order can be estimated by X-ray diffraction (XRD) [90] and transmission electron microscopy (TEM) [61]. Scanning electron microscopy (SEM) [90] is used to estimate pore morphology and pore structure. FTIR is used to study functional groups covalently bonded to the pore walls of these materials. Alternation of porosity manifests in pore size, its accessibility and pore size distribution, and can be efficiently studied using $N_2$ gas adsorption data at 77K for relative pressure ranging from ~0.05 to ~0.3. This helps to evaluate the monolayer capacity according to Brunauer-Emmet-Teller (BET) [91] method. The outcome of adsorption measurement is plotted in a sorption isotherm with the amount of gas adsorbed in the solid sample versus relative pressure. The calculations assume that (i) adsorbent surface and all adsorption sites are uniform, (ii) intermolecular interactions of adsorbed molecules are absent, (iii) at maximum adsorption only monolayers are formed, (iv) all molecules are adsorbed through the same mechanism, and (v) adsorbate molecule is immobile [92-94]. Adsorption isotherms are analysed using the following equation,

$$\frac{P/P_o}{V_a(1-P/P_o)} = \frac{1}{V_m C} + \frac{(C-1)}{V_m C}\frac{P}{P_o}$$

where $V_a$ and $V_m$ are the volume of the adsorbed molecules and maximum adsorbed molecules respectively, $P/P_o$ is the relative pressure (equilibrium pressure $P$ versus saturation pressure $P_o$, at the temperature of adsorption), and $C$ is a constant reflecting the strength of the interaction between the gas and the surface. $V_m$ and $C$ are calculated from the sorption graph. Therefore, the total surface area $A$ can be expressed by the following equation, where $N_A$ is the Avogadro number, $a_m$ is the cross section area of the adsorbate ($0.162\ nm^2$ for an adsorbed $N_2$ molecule) and $m = 22414\ mL$ is the molar volume:

$$A = \frac{V_m N_A a_m}{m}.$$

Pore size distribution and pore volume from the nitrogen sorption isotherms are determined most commonly by the Barrett-Joyner-Halenda (BJH) [95] method. The method assumes that all pores have cylindrical shape, and there is no interaction between the fluid and the pore wall. Using Kelvin equation [96] that correlates pore diameter and pore condensation pressure,

$$\ln\left(\frac{P}{P_o}\right) = -\frac{2\gamma V_L}{r_p RT}$$

where $\gamma$ is the surface tension of liquid nitrogen, $V_L$ is the molar volume, $r_p$ is the pore radius, $T$ is the temperature, and $R$ is the universal gas constant. Considering also the fluid-pore wall interaction, the modified Kelvin equation reads, $r_p = r_k + t$, where $r_k$ is the critical radius and $t$ is the statistical thickness. The shape of the isotherm depends on the porosity and the differences of the thermodynamic states between the confined and bulk liquid.

We have employed both BET and BJH methods to calculate the pore diameter, pore surface area and pore volume of the mesoporous materials studied here.

### 1.2.2 Solid State Nuclear Magnetic Resonance Studies on Mesoporous Systems

Solid state NMR is a non-invasive, non-destructive technique which can differentiate chemical compositions, and can probe intramolecular motions, motions such as rotation, diffusion, etc. One of the major challenges while studying adsorbed molecules on surfaces is sensitivity and resolution of NMR spectra [97]**.** Since adsorbed molecules are close to the pore surface, NMR spectra of these molecules may exhibit line broadening. Since position and intensity of spectral lines are very crucial in identifying binding sites, high resolution spectra are desirable. Magic angle spinning has addressed sensitivity and resolution issues to a larger extent for adsorbed molecules on silicate materials. Proton spectra are in most cases severely broadened by $^{1}$H-$^{1}$H homonuclear interactions. However, if molecular motion is present, the resulting spectral lines may be sufficiently narrow, and thus may provide sufficient chemical shift discrimination [98-102].

$^{29}$Si which is an integral part of the mesoporous framework is a 4.7 % abundant spin-1/2 nucleus [103,104]. Since the associated oxygen atom is NMR inactive due to spin zero,

an isotopic enrichment to $^{17}O$, spin 5/2, is needed for any correlation studies involving oxygen; hence $^{17}O$ studies are not commonly pursued. Characterization of the mesoporous framework is usually done by analysing $^{29}Si$ MAS or $^{1}H$-$^{29}Si$ CPMAS/2D correlation experiments. Figure 1.9(a) displays a template of SBA-15, modelled using Materials Studio [105] with quartz-alpha as the unit cell [106-108].

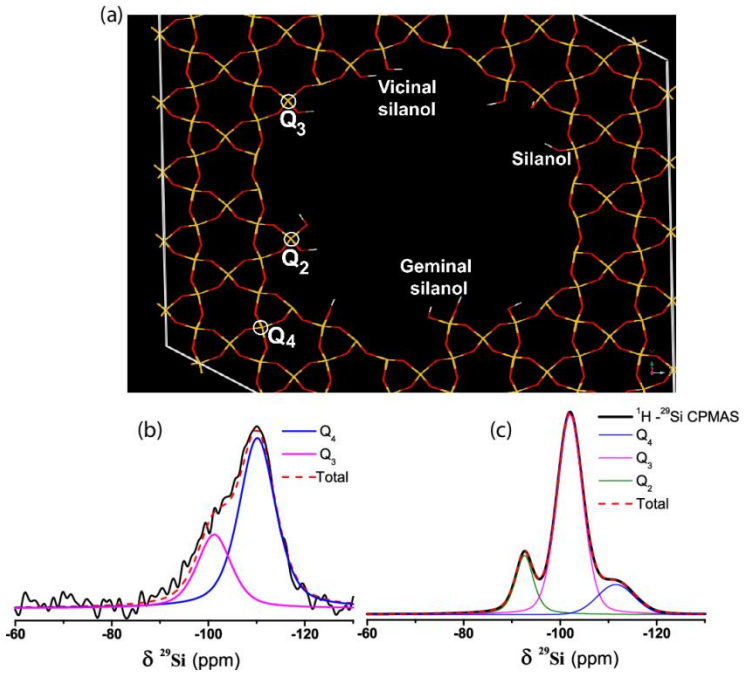


**Figure 1.9** (a) SBA-15 template, modelled using Materials Studio, starting with quartz-alpha. Geminal, vicinal and isolated silanol are shown. The various silica species, $Q_2$, $Q_3$, and $Q_4$ at -92.5, -102, and -112 ppm respectively are also marked. $^{29}Si$ spectrum of SBA-15 recorded at 10 kHz, (b) MAS and (c) CPMAS spectra and their deconvoluted components. The CP contact time was 5 ms. The colour code for molecules shown in (a) is, yellow for silicon atoms, red for oxygen atoms, and white for hydrogen atoms.

A supercell of dimension 8 x 8 x 5 is formed and a pore is made to mimic the mesopore. Geminal, vicinal, and isolated silanols on the pore surface are shown along with the silica species, termed as $Q_2$, $Q_3$, and $Q_4$, which resonate at ~ -90, -100, and -110 ppm in a $^{29}Si$ MAS (CPMAS) spectrum [109]. Each $^{29}Si$ species differ in relaxation rates, with the longest $T_1$ for $Q_4$. A $^{29}Si$ spectrum of SBA-15 recorded at 10 kHz MAS and its deconvoluted spectral components are shown in Figure 1.9(b). The MAS spectrum displays $Q_4$ and $Q_3$ as the dominant silica species. The activity of the pore surface depends on the percentage of $Q_2$ sites [99-102]. Though quantification of the signals from CPMAS spectra is not possible, the

presence of $Q_2$ silica species can be verified using a CPMAS spectrum. Figure 1.9(c) shows a $^{29}Si$ CPMAS spectrum where $Q_2$ silica species appears and $Q_3$ becomes well resolved. Due to polarization transfer from vicinal silanols, for a CP contact time of 5 ms, it can be seen that $Q_3$ gains more intensity than $Q_2$.

Water is the medium for most naturally-occurring reactions and interaction of water with silica surfaces is under constant study in order to understand confinement effects in environmental studies, biological applications etc. Since mesoporous silicate materials have hybrid organic-inorganic interface, large void pore volume, high surface area per unit volume and broad pore size distribution, they are used in diverse applications like molecular transport, surface catalysis, bio-mineralization etc., where water is the most widely used solvent. In particular, study of dynamics of confined water is important as water is found in nanoscopic confinements and it is known that properties of water under confinement differ from those of free water [99-102]. Confined water can experience hydrophilic/hydrophobic interactions or form hydrogen bonds. Different interactions of water molecules, among themselves or with the surface, result in distinct and well-defined chemical shifts in $^{1}H$ MAS NMR spectra. Depending upon the strength of hydrogen bonding the NMR relaxation mechanisms differ. Hence, proton relaxation experiments can be employed to distinguish between different proton species on the surface.

Extensive studies using solid state $^{1}H$ and $^{2}H$ MAS NMR spectroscopy were performed by various groups in order to understand the host–guest interactions in MCM type materials (pore size 2-6 nm) and SBA type materials (pore size 5-10 nm). Grünberg et al. [99] have systematically analysed different water environments in the pores of SBA-15 and MCM-41 by analysing the $^{1}H$ MAS and static NMR spectra. Recently, $^{1}H$ MAS NMR spectroscopy was employed to monitor the specific course of water in MCM-41, initially existing in a bulk-like form inside the pores and then distributing itself through the pores by hydrogen bonding to surface silanol groups [110-112]. Apart from proton NMR, dielectric relaxation spectroscopy (DRS) [113], FTIR, and high resolution quasi elastic neutron scattering, have revealed unusual hydrogen bonding networks of confined water. Subsequently, Trébosc et al. [85] have performed a systematic study of MCM-41 type mesoporous silica nanoparticles under low surfactant concentration using high solid state NMR at high MAS rates (~45 kHz). The structural characterization was performed by employing one-dimensional and two-dimensional $^{1}H$, $^{29}Si$, $^{13}C$, $^{1}H$-$^{1}H$ and $^{1}H$-$^{29}Si$ experiments. Studies performed by Trébosc et al. on organically functionalized mesoporous

silica materials provided detailed structural information through heteronuclear correlation experiments under fast MAS.

Amitay-Rosen et al. [101,102] have studied the slow exchange dynamics of selectively deuterated adsorbed amino acids (alanine, methionine etc.) close to silica surfaces in aqueous environment. Proton and deuterium MAS NMR spectra were recorded as function of temperature and hydration for characterizing surfaces and for studying dynamics. They have also developed a spectroscopic methodology for quantifying the number of water molecules per $nm^2$ in the pores of mesoporous materials. Azais et al. [114] has extended solution NMR techniques to study the confinement of guest molecules in MCM-41. The sample is characterized through J-coupling based experiments under MAS. Cross-relaxation techniques were employed to achieve signal enhancement of $^{13}C$ nuclear spins of the confined benzoic acid.

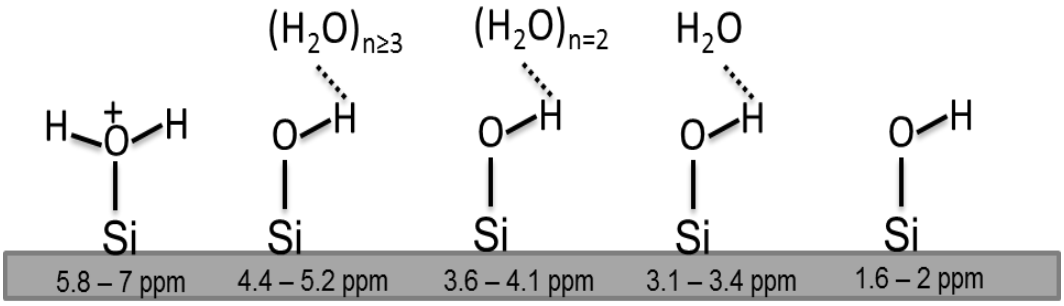


**Figure 1.10** Schematic of possible hydrogen bonding configurations of a few water molecules near the pore wall of mesoporous $SiO_2$ surface is shown along with the proton chemical shift ranges.

A schematic illustration of different proton species based on the model derived from proton MAS NMR study is shown in Figure 1.10 [98-102]. At very low hydration levels, when a few water molecules are adsorbed on the inner pore surface of mesoporous silicates, the adsorbed water molecules can engage in hydrogen bonding exhibiting characteristic resonances within a few distinct chemical shift ranges in the proton spectrum. Following Grünberg et al. and A-Rosen et al., these proton - oxygen structures situated near oxygen sites of the silica surface are termed as clusters [99-102]. With increase in water loading, different clusters undergo fast dynamics leading to sufficiently resolved proton spectra with characteristic chemical shift ranges. Such chemical shift ranges can be used to track different clusters present on the surface as a function of hydration, and their contribution to materials under study, in terms of

surface-guest interaction and pore-filling. The characteristic chemical shift ranges are [99-102]: (i) 5.8-7 ppm corresponding to protons that are strongly hydrogen bonded to the silica surface termed as acidic protons, (ii) 4.4-5.2 ppm corresponding to bulk water where more than two water molecules are hydrogen bonded, (iii) 3.1-3.4 ppm corresponding to a single water molecule hydrogen bonded to –Si-OH-, (iv) 3.6-4.1 corresponding to a situation where two water molecules are hydrogen bonded to -Si-OH-, and (v) 1.6-2 ppm corresponding to isolated silanols. In certain cases, chemical shifts in the range 0.8-1.5 ppm were also observed, arising from water molecules trapped in surface inhomogeneity, called as monomers [99,115]. A representative proton MAS NMR spectrum from SBA-15 is shown in Figure 1.11 [115]. The spectrum is deconvoluted using DMFIT [116] into components with chemical shifts in the characteristic ranges discussed above.

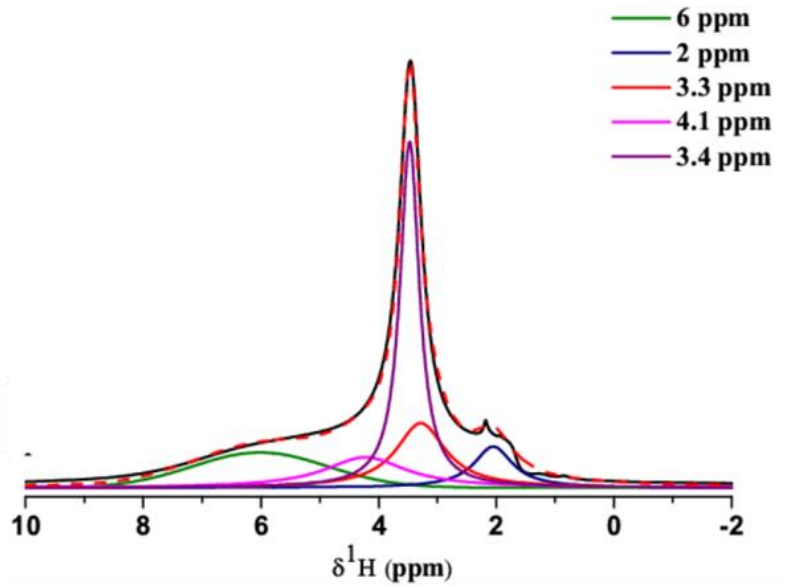


**Figure 1.11** Proton NMR spectrum of SBA-15, recorded at 10 kHz MAS rate. Various spectral components deconvoluted using DMFIT and the corresponding chemical shift is shown.

## 1.3 Dynamic Deuterium MAS NMR and Molecular Dynamic Simulations

Second part of the work presented in the thesis investigates dynamics induced by adsorbed water molecules on functionalized SBA-15, with the aid of deuterium MAS NMR. In order to comprehend the correlation between molecular motion and deuterium spectra, a brief introduction to dynamic deuterium MAS NMR is provided in this section. Towards the

end, a general introduction to molecular dynamic studies and in particular its pertinence to the thesis is given.

Molecular motions in the range of microsecond to second are of particular interest in dynamic studies, as this is the time scale of many significant biological events, chemical reactions, catalysis, protein folding etc. [11]. Slow dynamics is particularly sensitive to differences in structure as seen from polymer behaviour at glass transition, transport of ions or charges in viscous media etc. Dynamic studies provide crucial information about polymer morphology like chain organization and mobility, and heterogeneities in structure and dynamics of amorphous polymers [11, 117,118]. In solution state, due to molecular tumbling, only dynamics slower than the Brownian motion is detected, mainly through isotropic chemical shift exchange experiments. Therefore, nanosecond-microsecond dynamics information is lost. The inherent limitations of solution state NMR also include the need of solubility of molecules in solution, and broadening of spectral lines due to slower motion with increase in molecular size thereby reducing sensitivity and resolution of NMR spectrum.

Solid state MAS NMR does not have these inherent limitations and hence emerged with time as an important and efficient tool for the study of motional processes. With increase in size of molecules, the MAS spectral lines can acquire broadening due to non-averaged anisotropic interactions [11-13]. Nevertheless, the advancements in hardware and different pulse techniques have succeeded over years to provide atomic-level structural and dynamic information in non-crystalline samples, insoluble systems, or even large molecules like nuclei acids and membrane proteins. Since picosecond to microsecond dynamics in proteins determines $^{13}C$ and $^{15}N$ $T_1$ relaxation times, site-resolved internal dynamics in proteins can be obtained through relaxation-based experiments on isotopic enriched solid samples [41]. Internal motions in the range of hundreds of microsecond reduce $^{1}H$-$^{13}C$ or $^{1}H$-$^{15}N$ dipolar couplings as the bond orientation changes randomly due to dynamics. Analysis of $^{13}C$ chemical shift anisotropy or $^{2}H$ quadrupolar powder spectra provides detailed insights about molecular reorientations and a large number of one-dimensional and two-dimensional studies are reported in the literature till date [11,12]. Molecular motion can be characterized by motional amplitude which can change with tensile stress and temperature. Rotational jumps and angular fluctuations in molecules often happen as a function of temperature or when a phase transition occurs [11]. Phenylene ring flip by $180^{o}$ [11, 120,121] is a well-known example (discussed below) and, apart from solid state NMR, electron paramagnetic resonance (EPR) [117,118] and quasi elastic neutron scattering experiments are employed to

study these molecular flips. Tuning these large amplitude motions is very important for tailoring host-guest systems for specific applications.

### 1.3.1 Deuterium Lineshape Analysis and Motional Model

Deuterium, a quadrupolar nucleus with $I = 1$, is particularly useful for studying dynamics due to the following reasons. The z axis of the PAS of the quadrupolar tensor is fixed in the bond direction. With molecular mobility, the PAS reorients with time resulting in averaging of the quadrupolar interaction in the lab frame [11,122]**.** Therefore $^{2}$H NMR spectra naturally reflect molecular mobility [11,101,102]. Deuterium solid state NMR lineshapes are highly sensitive to motional timescales ranging from $10^{-11}$ to $10^{-2}$ s. Even with two deuterons spatially correlated, due to the low gyromagnetic ratio, the homonuclear dipolar interaction between deuterons is negligible (< 1 kHz) and hence spin diffusion is slow. This results in purely motional-induced relaxation times. Numerous analytical and numerical tools are available for the analysis of deuterium dynamic spectrum [123-126]. The maximum deuterium quadrupolar coupling is about 260 kHz arising from a rigid C-D group. Hence a single pulse would be able to excite the entire spectral range.

In functionalized materials, an organic linker is covalently bonded to the silica surface thereby altering or enhancing the function of mesoporous materials. This process is termed as grafting. If grafting concentration is low, 1 molecule/nm$^2$, even with isotopic labelling, static deuterium NMR spectra lack sensitivity [127]. Conversely, low concentration is necessary to avoid intermolecular interactions. In such cases, $^{2}$H MAS NMR is preferred over its static counterpart as sensitivity is significantly increased and at the same time information about quadrupolar interaction is retained. Even with the merits mentioned above, owing to the low deuterium natural abundance, 0.02 %, isotopic enrichment is necessary. Nevertheless, due to its sensitivity to a broad range of dynamic time scales, deuterium is a valuable nucleus for probing dynamics in diverse systems, ranging from proteins to materials. Among the type of motions that may affect quadrupolar interaction in a solid are (a) torsion oscillations, where a molecule makes small amplitude motion about a stable equilibrium and (b) hindered rotations, [3] where the molecule may undergo transition between several positions, separated by potential barrier, at a certain rate.

Molecular motional timescales are characterized by correlation time $\tau_c$ and corresponding rate of exchange, $k$. Based on this, dynamics is categorized as slow (rates up

to $10^4$ $s^{-1}$, for deuterium $k < C_Q$), intermediate ($10^4$ to$10^6$ $s^{-1}$, $k \cong C_Q$) and fast (>$10^6$ $s^{-1}$, $k > C_Q$) [3,11,101,102]. Pronounced changes of the solid state NMR spectrum occur when $1/\tau_c$ is comparable to the anisotropy, MAS rate or magnitude of the RF field. In this case dynamic time scale is termed as intermediate and interference between molecular dynamics and coherent evolution result in reduction of intensity of the spectrum. For slow motion, the resultant spectrum is largely free from motional effects. This is often termed as rigid limit or static limit, and motion-independent quadrupolar parameters, $C_Q$ and $\eta$, can be estimated from analysis of the spectrum [122]. With the presence of molecular mobility (angular fluctuations, jumps between discrete molecular sites or molecular flips) in the intermediate or fast motion limit, quadrupolar parameters corresponding to the rigid limit are averaged, and the dynamic MAS NMR spectrum is characterized by a reduced *effective* quadrupolar coupling constant and possibly modified asymmetry parameter [11,101,102,117-127].

Dynamic studies often involve comparison of rigid-limit quadrupolar coupling parameters $\{C_Q, \eta\}$ with the dynamic average $\{\bar{C}_Q, \bar{\eta}\}$. Such comparisons may suggest or support a specific molecular motional model. The motionally averaged quadrupolar lineshapes are dependent only on two parameters, $\bar{\eta}$ and $\bar{C}_Q/C_Q$. However knowledge of $\{\bar{C}_Q, \bar{\eta}\}$ is not capable to discriminate different types of motion, as for example diffusive processes, discrete jumps, etc., may result in identical lineshapes [11]. Localized motions in liquid crystalline polymers and polymer model membranes are investigated by Spiess and co-workers through analysis of deuterium spectra of deuterated phenyl groups [11,117-119]. Utilizing deuterated phenyl groups is particularly informative as they undergo fast, discrete jumps between well-defined geometries. The changes in $^2$H MAS NMR theoretical lineshapes due to possible types of dynamics are illustrated using the example of deuterated phenylalanine ($d_5$) [120,121]. Figure 1.12 shows a schematic of a phenylalanine ($d_5$) with the phenyl ring undergoing dynamics about the $C_\beta - C_\gamma$ axis. The spectrum in the rigid limit, $\{C_Q, \eta\} = \{180\text{ kHz}, 0\}$, the spectrum corresponding to 180° flips about $C_\beta - C_\gamma$ axis, $\{112.5\text{ kHz}, 0.6\}$, and the spectrum superimposing both rigid (20%) and 180° flip (80%) components is shown. When phenyl ring undergoes fast rotation about the $C_\beta - C_\gamma$ axis, the $V_{zz}$ of the $C_\epsilon$ - bonded deuterium is aligned along $C_\epsilon - D$ bond direction and makes 60° with the axis of rotation. The resultant dynamic averaged quadrupolar parameters become $\{22.5\text{ kHz}, 0\}$ and the corresponding spectrum is shown in (e). Since $C_\zeta - D$ lies along the axis of rotation, the experimental spectrum should have a rigid contribution. A rigid

contribution may also arise from those phenyl rings which are not undergoing dynamics. As shown by Gall et al., [120] since the dynamic averaged and the rigid components exhibit different relaxation times, experimental parameters can be chosen in order to select only the dynamic components. The spectra shown in Figure 1.12 are simulated using NMR-WEBLAB, [125] and for 180$^o$ fast flip a two site jump model on a cone is assumed with cone angle $\theta = 60^o$ and jump angle $\Delta\phi = 180^o$. A discussion of the cone model is given below.

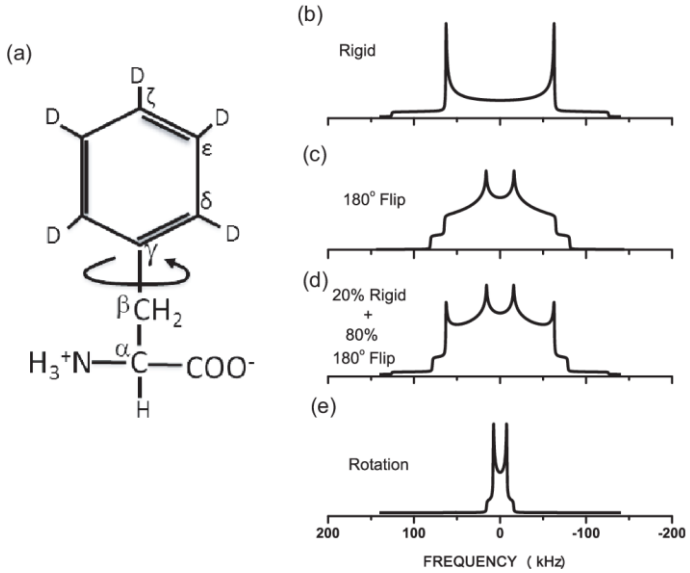


**Figure 1.12** (a) Schematic representation of phenylalanine ($d_5$). Spectra simulated using NMR-WEBLAB for (b) rigid limit, with $\{C_Q, \eta\} = \{180\text{ kHz}, 0\}$ (c) 180$^o$ flip about $C_\beta - C_\gamma$ axis resulting in $\{\bar{C}_Q, \bar{\eta}\} = \{112.5\text{ kHz}, 0.6\}$, (d) sum spectrum of (a) and (b) with 20% of rigid and 80% of dynamic components, and (e) free uniaxial rotation with rotation axis making 60$^o$ with $C_\epsilon - D$ bond direction resulting in $\{\bar{C}_Q, \bar{\eta}\} = \{22.5\text{ kHz}, 0\}$.

**Dynamic Model:** The simple and most commonly encountered molecular motional model is restricted to motion of bonds or segments on a cone [124,125]. For motion on a cone, it is assumed that the principal values of the quadrupolar tensor remain constant during motion. If part of the molecule rotates about a fixed bond, or if the motion takes place about a $C_n$ axis, it can be categorized as motion on a cone. Schematic of a two site jump on a cone for a C-D bond is shown in Figure 1.13. where the vertical axis of the cone, assigned as $Z_{CF}$, can be aligned with the rotation axis, and $X_{CF}$ axis points along the symmetry axis. In this coordinate system, the jump positions are characterized by $\{\theta, \phi_1\}$ and $\{\theta, \phi_2\}$, where $\theta$ is half the apex angle of the cone, and the jump angle, $\Delta\phi = \phi_1 - \phi_2$. By a coordinate

transformation by means of Wigner matrices, from the PAS to the cone frame (CF), the components of the quadrupolar interaction tensor, $\bar{\bar{Q}}$, in the CF can be determined. Effective quadrupolar parameters are calculated by averaging $\bar{\bar{Q}}$ over $\phi$ angles.

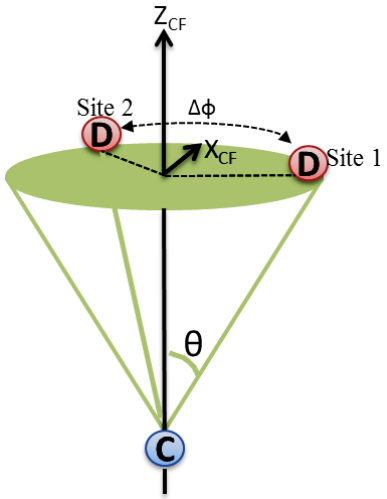


**Figure 1.13** (a) Schematic representation of a two site jump for a C-D group, modelled on a cone [125].

Conformational transitions, e.g. trans-gauche, are often encountered in alkyl chains or molecules with tetrahedral symmetry. In such cases, rapid molecular motion often combines small angle librations around equilibrium positions combined with occasional discrete jumps, or discrete jump between $n$ sites, $n \geq 2$, possibly with change in conformation [11]. Due to deviation from local symmetry, the $n$ sites may be characterized by unequal potential wells and unequal populations [3,11]. Angular fluctuations for discrete jumps between multiple sites can result in a spectrum containing both axial and non-axial quadrupolar contributions. Linewidth of the spinning sidebands, quadrupolar parameters extracted from the spectrum, their variation with temperature, etc. can be utilized to associate the NMR derived information to molecular mobility. When several dynamic components are present the powder lineshape becomes more complex as illustrated in Figure 1.14, where static and MAS spectra are sums of axially-symmetric rigid, $(C_Q = 160\,\text{kHz}, \eta = 0)$ and asymmetric dynamic components, $(C_Q = 80\,\text{kHz}, \eta = 0.6)$. Equal and unequal populations are considered, as specified in the figure captions. Molecular motions may also involve a range of dynamic timescales at the same time resulting in complex spectrum. Relaxation studies are particularly important in the fast motional regime [123], where relaxation times of

quadrupolar order reflect dynamics. A few experimental techniques have also been developed to address dynamics through deuterium solid state NMR.

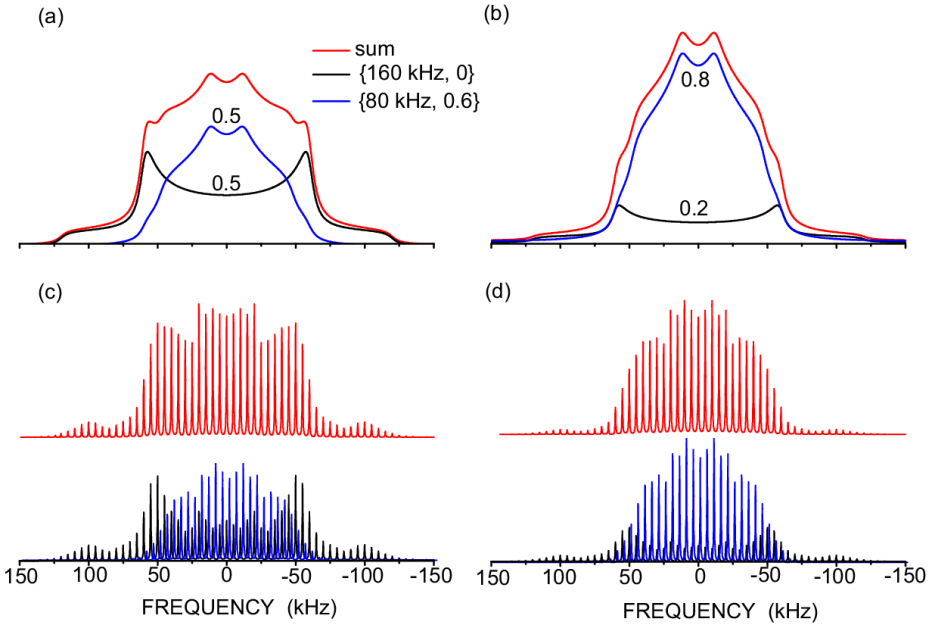


**Figure 1.14** Simulated static and MAS (5 kHz) spectra of deuterium arising from the sum of rigid and dynamic components, with (a, c) equal and (b, d) unequal populations. In (c) and (d), the blue spectral lines are shifted towards left for better visibility.

Amitay Rosen et al. [101,102] have employed Bloch-McConnel [128] equations to retrieve kinetic parameters associated with molecular dynamics. Since deuterium is known for its sensitivity towards molecular dynamics, they have employed $^{2}$H MAS NMR to understand the slow exchange motion of the adsorbed solute guest molecules in mesoporous silicates. Floquet theoretical approach was used to simulate the dynamic deuterium MAS NMR spectra and the simulated spectra were compared with the experimentally analysed $^{2}$H MAS NMR spectra so as to derive kinetic parameters. Based on the analysis of the kinetic parameters a motional model for exchange dynamics was suggested. The system under consideration consisted of deuterated small molecules adsorbed in mesoporous materials like SBA-15, MCM-41 etc. The dynamic model assumed a two-site exchange process, where the solute molecule is exchanging between an isotropic free state and a bound state. Deuterium dynamic studies of adsorbed guest molecules were also conducted time and again by Buntkowsky and co-workers for various systems [166]. There exists several software tools for deuterium dynamic modelling, NMR-WEBLAB, EXPRESS (exchange program for relaxing spin

systems) [125], KLDMAS (lysine (K) leucine (L) dynamic MAS) [126] are a few among them.

Distorted quadrupolar lineshapes may introduce errors in the estimation of quadrupolar parameters. Hence in most cases, a quadrupolar echo [124,125] sequence is utilized which provides lineshapes largely free from artefacts. However, with samples containing less number of deuterons utilization of quadrupolar echo is not recommended due to sensitivity loss. In our studies we have recorded dynamic deuterium MAS spectra using the $90^{o}$ pulse-acquisition and the time domain signal was shifted to first echo before Fourier transform. Along with removing artefacts produced by the probe/electronics, shifting to the first echo also removes any fast decaying, intermediate dynamic, components. Molecular dynamics involved in the systems under study (chapter 3) is mostly in the fast dynamic regime; hence shifting the signal by first echo has not introduced substantial errors in the analysis.

### 1.3.2 Molecular Dynamic Simulations

In fact, no single approach is capable to provide a complete picture of molecular dynamics and usually multi-technique approaches are employed. Within this strategy, nowadays computer assisted simulations and molecular modelling have become an integral part of NMR studies of structure and dynamics in proteins and microcrystalline systems. The field of materials science, catalysis and mesoporous materials in particular, benefits now from the multidisciplinary point of view which aligns computational modelling with synthesis and characterization. Efficient algorithms, parallel computing, improvement in computer memory, machine learning, and newly developed visualization tools make computer modelling useful to many fields.

Catalysis deals mostly with mesoporous materials which are amorphous. Understanding amorphous silica systems is challenging due to heterogeneity in its composition and local structure. As mentioned earlier, the structure and properties of the amorphous materials strongly depend on synthesis protocol. This poses difficulty in modelling them and often crystalline materials are used as approximate amorphous support. $\alpha$-quartz and $\beta$-crystabollite are the most used candidates for building amorphous silica surface models [106-108]. Quest for improved models including the thermodynamic properties of hydrogen bonded and non-hydrogen bonded silica surfaces was addressed by

Prof. Uglienco [129]. Based on density functional theory (DFT) [131], they introduced a model capable to predict properties of MCM-41 more accurately. In DFT, the computational complexity associated with the many-body Schrödinger equation is sidestepped by focusing on the electron density and representing the total energy of the system as a unique functional form of electron density. The problem of computing ground state energy and particle density of N-coupled electron system has been addressed by Kohn and Sham [130]. The Kohn-Sham equations consist of N single particle three dimensional equations with a modified effective potential which is function of particle density. The modified potential is also a function of quantum-mechanical exchange and correlation (XC) of the particles, and is relatively small when compared with single particle kinetic energy or Coulomb potential. Finding approximations to the XC terms defines the success of DFT. Further improvements and combinations of DFT with other classical molecular modelling have enriched the computational arena [131-133].

Rimola et al. studied the adsorption of glycine on silica surface using a crystalline silica surface model [107]. Costa et al. studied the interaction of glycine with an amorphous hydrophilic silica surface by means of a periodic DFT [131-133]. In these computational studies, Costa et al. propose a binding model according to which carboxylate in glycine facilitates the main anchor of the amino acid while ammonium is pendent. This is contrary to the observations derived from solid state NMR experimental studies performed by Ben Shir et al. [134]. They reported that the adsorbents, glycine and L-alanine, interact with silica surface (SBA-15, MCM-41) via their amine moiety while their carboxylate end is pendent. The proposed model based on their experimental observations suggests a positively charged ammonium moiety interacting with the negatively charged Si-$O^-$ on the surface. This further highlights the importance of employing experimentally-derived MD constraints whenever possible. A correlation between the characteristics of silanols at silica surfaces in the presence of solvents has been studied with ab-initio molecular dynamics (AIMD) [135] simulations of the full silica-water interface. Pioneering work on amorphous silica-water interface has been investigated by Cimas et al. using DFT based molecular dynamic simulations [135]. Jayanthi et al. [127,135,137] have utilized MD simulations to provide a model supporting the adsorption-desorption kinetics, of a deuterated di-peptide on hydrated silica surface.

MD study relevant to the work utilizes Dassault's Materials Studio [105] and follows the work reported by Vega and co-workers in grafted mesoporous systems. In MD, simulation of a system amounts to choosing a potential, $V(r_1, r_2, .. r_N)$, where $r_1, r_2, .. r_N$

defines the position of N atoms in the system. Potential energy of a system is the sum of bonded energy, non-bonded energy, and energy associated with intermolecular interactions, called the cross-terms energy. The total energy can hence be represented as

$$E_{total} = E_{bonded} + E_{non-bonded} + E_{cross\ terms}.$$

$E_{bonded}$ includes bond stretching, bond bending, and dihedral angle energy terms. $E_{cross\ terms}$ includes the effect of neighbouring atomic positions on bond lengths, valance angles and torsion angles. The energy of interaction between non bonded atoms includes van der Waals and electrostatic terms. Van der Waals interaction uses the Lennard-Jones 9-6 function and Ewald summation is used to calculate Coulombic interaction. Within the Materials Studio package, DISCOVER for minimalization and COMPASS (Condensed phase Optimized Molecular Potentials for Atomistic Simulation Studies) [138] forcefield for dynamics are used for the study presented in the thesis. Minimalization or optimization is an integral part of any MD simulation where optimal atomic coordinates, bond-lengths, dihedral angles of atoms are obtained by minimizing the energy. This will avoid any local distortions in the structure resulting in unstable simulation during a dynamic run. In Materials Studio, within DISCOVER, smart minimizer starts with the method of steepest descent, and we have chosen the conjugate gradient method for minimization. Method of steepest descent generates low energy structures irrespective of the initial structure and conjugate gradient method improves the minimum-line search direction by an iterative process. For large systems, conjugate gradient is the method of choice [105].

In this study, equilibration was achieved within 10,000 steps in time steps of 1 fs. Time evolution of the model system was computed using the classical MD approach which involves simultaneous integration of Newton's equations of motion for all atoms in the system. Simulations were performed at constant volume and temperature (NVT) ensemble, simulation temperature was controlled by Anderson thermostat. Dynamic runs were carried out for about 1-2 ns, and each $1000^{th}$ configuration, corresponding to changes at 1 ps, was saved as a trajectory file. We have imposed periodic boundary conditions while performing simulations where a volume containing N particles is treated as a primitive cell of an infinite periodic lattice of identical cells.

Host silica surface is modelled following Chaffe [108]. Construction of the MD template and analysis of the trajectories extracted from MD runs follows the details in Ref. [127]. The initial structure is generated from $\alpha$ quartz with unit cell dimensions $a = b =$

4.91 Å , and $c = 5.402$ Å. A periodic $16 \times 16 \times 16$ supercell is created and a hexagonal pore is formed by removing silicon and oxygen atoms. After attaining a pore diameter of ~ 3.8 – 4.0 nm, all the vacant silicon atoms are saturated with hydroxyl (OH) groups and vacant oxygen are saturated with hydrogen (H) atoms. The template is subjected to DISCOVER minimization, followed by dynamic runs of ~500 ps. After each MD calculation water molecules are consecutively removed**,** when the distance between the hydrogen bonded OH and H in adjacent Si-OH---HO-Si is $< 2.5$ Å. Subsequent removal of water results in Si-O-Si linkage and also introduces slight deviations form hexagonal pore geometry. The surface was dehydrated so as to achieve surface hydroxyl concentrations of ~ 2.5 OH/nm$^2$. The template thus modelled forms the mesoporous surface in our study to which the linear molecule to be grafted, after structural minimalization using DISCOVER program, is covalently bonded. The template along with the grafted molecule is subjected to a few more DISCOVER minimalizations so as to get a stable energy minimized equilibrium model, to be considered for further dynamic simulations. For dynamic simulations, hydroxyls are randomly distributed, near the grafted molecule mimicking a real scenario, yet maintaining the silanol concentration as ~2.5 OH/nm$^2$. Figure 1.15 shows an MD simulation template used in this study.

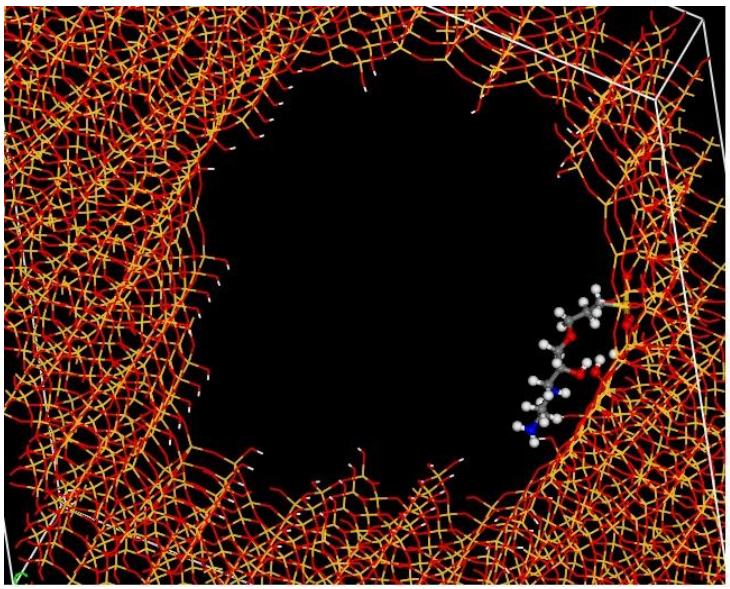

**Figure 1.15** Mesoporous template with grafted linker (diamine-GPTMS in $T_3$ configuration) used in this study.

Dynamic simulation output provides trajectory file with the instantaneous coordinates of all the atoms belonging to the grafted molecule. The molecular coordinates are extracted

from Materials Studio, and are analysed using already existing MATLAB$^{@}$ (Mathworks Inc.) code. For an axially symmetric deuterium quadrupolar coupling, in a C-D bond, the Z component of the PAS of the EFG tensor points along the bond direction. With molecular mobility this PAS randomly changes orientation. The expression of moving EFG tensor in a fixed coordinate system is given by

$$\boldsymbol{V'} = \frac{V_{zz}^{PAS}}{2}\begin{pmatrix} 3\sin^2\theta\cos^2\phi - 1 & 3\sin^2\theta cos\phi sin\phi & 3sin\theta cos\theta cos\phi \\ 3\sin^2\theta cos\phi sin\phi & 3\sin^2\theta\sin^2\phi - 1 & 3sin\theta cos\theta sin\phi \\ 3sin\theta cos\theta cos\phi & 3sin\theta cos\theta sin\phi & 3\cos^2\theta - 1 \end{pmatrix}$$

where $(\theta, \phi)$ represents the *time-dependent* polar angles that correlate the fixed frame to the moving frame and $V_{zz}^{PAS}$ is the Z principal value of the EFG tensor. From each trajectory file, $(\theta, \phi)$ are calculated with respect to a fixed coordinate (F) system and $V_{zz}'$ is obtained. Taking the average of $V_{zz}'$ for 1-2 ns MD run and diagonalizing the averaged matrix provides dynamic averaged $\{\bar{C}_Q, \bar{\eta}\}$ parameters. All MD simulations provided in chapter 3 are analysed in this manner by assuming a fixed coordinate system. A fixed coordinate system was defined with respect to the pore wall of the template. The line connecting any two oxygen atoms, O1 and O2, bonded to the –Si- atom, through which the molecule is anchored to the pore wall, is taken as the reference line, say $X^F$ axis. The line which contains the –Si- atom and the centre *O* of the O1-O2 segment is considered as $Z^F$ axis. The axis $Y^F$ is the line perpendicular to $X^F$ and $Z^F$ which passes through *O*. All coordinates extracted from the dynamic run are subjected to a coordinate transformation and the dynamics is interpreted with respect to this fixed coordinate system. The spatial variation of C-D bond direction with respect to this coordinate system is analysed for dynamic information. Coordinates extracted from trajectories are also used for calculating dihedral angles which can provide information on conformational changes associated with molecular mobility if any.

Similar to the previous studies [127,135], dynamic studies are free from any motional model hence called *a-priori*.

## 1.4 Objectives of the Study

The work presented in this thesis is distributed in two chapters. Chapter 2 analyses the distribution of water in the pores of mesoporous materials of interest as revealed through proton MAS NMR. Chapter 3 discusses dynamics of linkers, induced by a few water

molecules/nm$^2$, analysed using proton and deuterium MAS NMR and MD simulations, in functionalized mesoporous hybrid materials of interest. The main objectives are as follows.

(i) **To understand surface characteristics of a hydrophobic-hydrophilic silica surface through proton solid state MAS NMR**: In chapter 2, we investigate the connection between the characteristics of pore surface and the concentration of –OH groups, under controlled hydration of a mesopore containing both hydrophilic and hydrophobic sections. This type of studies is extended to a complex system for the first time. We provide a pore filling model through the study of distribution of confined water in ethane substituted periodic mesoporous organosilicate ($PMO_E$) materials. Proton spectra acquired at different hydration levels are analysed and interpreted in terms of water clusters of various sizes and distributions of water layers on the pore surface. The challenges encountered while analysing the surface under water adsorption, and the manner in which they were overcome are discussed.

(ii) **To understand water-induced dynamics of inkers in amine-functionalized mesoporous hybrid materials using proton and deuterium MAS NMR and MD simulations**: In chapter 3, we present a deuterium MAS NMR analysis on amine-functionalized hybrid materials (3-glycidyloxypropyl)trimethoxysilane (3-GPTMS) and 3-(trimethoxysilyl)propylmethacrylate (3-MATMS) grafted on SBA-15. Proton and deuterium solid state NMR experiments under MAS were performed at two hydration levels and temperatures ranging from 253 to 315 K. Changes in deuterium MAS lineshapes are analysed and information related to molecular dynamics is derived. From the NMR spectral analysis, we could suggest a relation between mobility and length of the linkers, steric hindrance, and grafting concentration. By correlating proton and deuterium MAS NMR spectral analysis, the role of a few water molecules in inducing dynamics of the linkers is investigated. MD simulations support the experimental analysis and provided molecular conformations associated with dynamics.

# 2
# Dynamic studies on Periodic Mesoporous Organosilicates

A number of studies have been reported in which different types of PMOs have been characterized, mostly by X-ray diffraction and transmission electron microscopy as mentioned in section 1.2. Nevertheless, these techniques do not provide a molecular level picture similar to the one obtained through solid state NMR techniques where information about bonding, nearest neighbour correlations, interaction strengths and dynamics, etc. can be derived. Grűning et al. employed surface enhanced NMR spectroscopy (SENS) [139] using dynamic nuclear polarization (DNP) to study functionalised PMOs. The organic part of a PMO and that of the surface functionalization of PMOs by Cp*Ir(III) derivatives were characterized using DNP-SENS. $^{13}C$, $^{29}Si$ and $^{15}N$ CPMAS as well as $^{1}H$–$^{13}C$ and $^{1}H$–$^{29}Si$ heteronuclear correlation experiments on PMO derivatives were performed at natural abundance using the above technique for structural characterization. Their observations not only confirmed the proposed four-layer structure found by XRD and TEM studies, but also allowed the reactivity of the surface groups to be quantified, which was difficult otherwise. Additional evidence for the formation of surface complexes was obtained through a 2D $^{1}H$–$^{13}C$-HETCOR (heteronuclear correlation) experiment. F. Lin et al. [140] studied an ethane PMO using EPR, through the nitroxyl radical. EPR line shapes displayed differences due to the mobility of the radical in the presence or absence of adsorbed water. Jones et al. [141] investigated the structural heterogeneities depending on different pre-hydrolysis treatments of organic silica precursors in $CH_2$–$CH_2$ and CH=CH PMOs using $^{1}H$ fast MAS (25 kHz), $^{13}C$ and $^{29}Si$ CP-MAS and 2D HETCOR ($^{1}H$–$^{29}Si$ and $^{1}H$–$^{13}C$) experiments. Kinetic studies were performed using $^{13}C$ and $^{29}Si$ variable contact time (VCT) CP-MAS experiments. Distributions of organic functional groups within the PMOs were analysed using solid state NMR observations. Recently, Mietner et al. [142] used the potential of solid state NMR to understand the molecular mobility of water confined in periodic PMOs. Their observations show that the mobility of confined water is influenced by the polarity of the organic moiety. 2D HETCOR ($^{1}H$–$^{29}Si$ and $^{1}H$–$^{13}C$) NMR experiments at high, medium and low water loading were performed and subsequently a pore filling model was proposed. Through solid state NMR observations, they concluded that pore size and polarity contribute equally to the confinement effects of water, thereby resulting in drastic changes in the dynamic properties.

In the present study, using the methods described in chapter 1, we monitor the distribution of water molecules near the pore surface in two different mesoporous materials, an ethane-PMO ($PMO_E$) and SBA-15, through one pulse $^1H$ MAS NMR spectroscopy. The major difficulty in extending similar approach to study $PMO_E$ is the presence of $-CH_2-CH_2-$ group in the bulk of $PMO_E$ which will subsequently interfere with the dynamic proton analysis. We have employed 2D wide-line separation (WISE) [11,167] technique to obtain information on proton homonuclear dipolar interactions associated with $-CH_2-CH_2-$ which was subsequently used for analysing the proton MAS NMR spectra.

## 2.1 Materials and Methods

**2.1.1 Synthesis of SBA-15 and $PMO_E$**:- Mesoporous silica SBA-15 was synthesized by using Pluronic 123 (P123) as the surfactant and tetraethylorthosilicate (TEOS) as the silica precursor in acidic medium through a sol–gel hydrothermal method. In a typical procedure, 19.8 g of P123 was dispersed in 135 g of water in a one litre beaker and stirring was continued for up to 1.5 h. To this dispersed solution, 540 g of 2 M HCl was added with constant stirring and the reaction was continued for a further 2 h. After 2 h, 40.5 g of TEOS was added to the solution in a drop wise manner and the reaction was extended for one day. The colloidal reaction mixture was transferred to a 1 L autoclave for ageing at 100 $^oC$ for 48 h. The residual solution was filtered, washed with water, and dried at 70 $^oC$ for 12 h. Finally, the as-synthesized material was calcined at 540 $^oC$ for 6 h to obtain the white powdered SBA-15 (Figure 2.1(a)) [50].

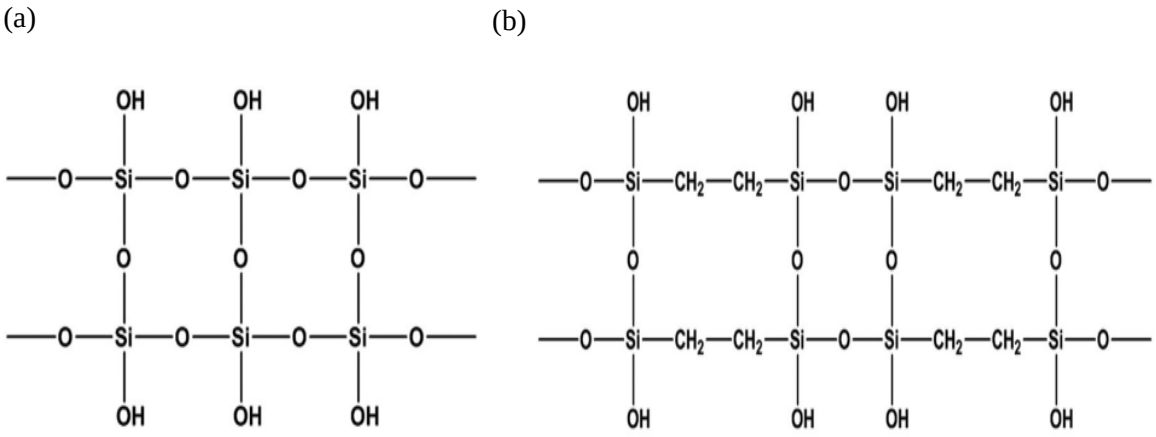


**Figure 2.1** Schematic representation of (a) SBA-15 and (b) ethane substituted organosilica ($PMO_E$)

The synthesis of ethane containing periodic mesoporous organosilica was carried out by using trimethyloctadecylammonium bromide ($C_{18}$-TAB) as the surfactant and 1, 2-bis-(triethoxysilyl) ethane (BTEE) as the silica precursor. In a typical synthesis, 3.36 g of $C_{18}$-TAB was dissolved in an aqueous (96 ml of water) NaOH (1.62 g) solution. The reaction mixture was stirred for 20 minutes and to this solution, 4.5 g of BTEE was added in a drop-wise manner. Stirring of the solution was continued for up to 20 h at room temperature. The colloidal solution was transferred to a round bottom flask and kept at 95 $^{o}$C for 40 h for ageing with vigorous stirring. After 40 h, the solution was filtered, washed with water and ethanol and dried at 70 $^{o}$C for 12 h. The resultant material was solvent extracted by acidified ethanol (0.5 ml of conc. HCl in 60 ml of ethanol for 1 g of as-synthesized material) at 70 $^{o}$C for 12 h. The solvent extracted material was filtered, washed and dried at 50 $^{o}$C for 10 h (Figure 2.1(b)) [67].

**2.1.2 Sorption Analysis**:- $N_2$ adsorption–desorption isotherms, pore size distributions (inset) and the textural properties of $PMO_E$ and SBA-15 were determined by using a Micromeritics Tristar II, USA and the results are plotted in Figure 2.2. Both materials exhibit a type-IV isotherm with a H1 hysteresis loop, which indicates the existence of mesoporous integrity. The BET surface area, pore diameter and pore volume of SBA-15 and $PMO_E$ are given in Table 2.1.

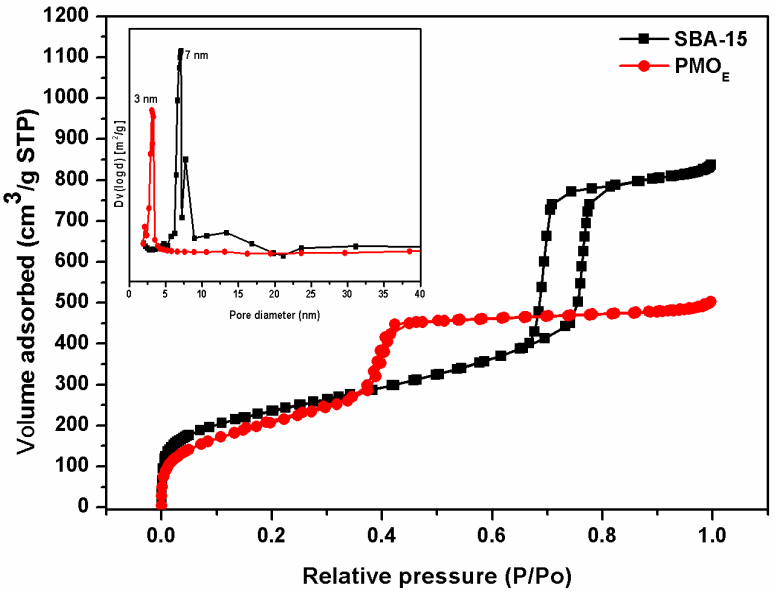


**Figure 2.2** $N_2$-Sorption isotherm and pore size distribution curves (inset) of SBA-15 (black) and $PMO_E$ (red).

**Table 2.1:** Textural properties of SBA-15 and $PMO_E$

| Sr.No. | Materials | BET Surface area [$m^2/g$] | Mean pore diameter (nm) | Mean pore volume [$cm^3/g$] |
|---|---|---|---|---|
| 1 | SBA-15 | 841 | 7 | 1.24 |
| 2 | $PMO_E$ | 775 | 3 | 0.83 |

**2.1.3 Sample Preparation**:- The solvent extracted, dried $PMO_E$ and SBA-15 packed in a 4 mm rotor may have had some amount of adsorbed water. The samples were subjected to vacuum to reach their driest possible states. In order to increase the hydration level within the packed samples, the rotors with cap open were kept in separate closed environments along with exposing them to a definite amount of double distilled water. The weight gains of the rotors containing the samples were measured within an accuracy of ±0.1 mg, and 1D $^1H$ MAS NMR spectra of the samples were recorded under identical experimental conditions as explained in the next section. In order to prepare samples with different hydration levels in a controlled manner, the hydrated samples inside the rotors were subjected to a vacuum line by removing the rotor cap and by pumping for specific time periods. After each pumping period, the weight of the rotor containing the sample was measured and a $^1H$ MAS NMR spectrum of the sample was recorded.

## 2.2 NMR Measurements

The $^1H$ MAS NMR spectra analysed and compared here were recorded at 298 K on a Bruker DSX 300 MHz NMR spectrometer equipped with a 4 mm MAS probe. One pulse NMR experiments were performed at a spinning rate of 10 kHz, the $^1H$ $90^o$ pulse length was 2.5 µs and the recycle delay was 1 s. $^{29}Si$ and $^{13}C$ CPMAS spectra of SBA-15 and $PMO_E$ were also recorded at a 10 kHz MAS rate. The CPMAS contact time was 5 ms for $^{29}Si$ and 1 ms for $^{13}C$. A two-dimensional $^1H$–$^{13}C$ WIde-line SEparation experiment was performed at a 10 kHz MAS rate in a DSX 300 MHz spectrometer. The incremental delay used was 5 $\mu s$ for 256 $t_1$ points, thus providing an acquisition time of 1.28 ms in the indirect dimension. The recycle delay used was 2 s and the number of scans was 128 for each $t_1$ increment. A short contact time was used during the CP transfer and the STATES [143] method was used to acquire and process the two dimensional data. We also recorded a $^1H$ MAS spectrum at 298 K at a spinning rate of 60 kHz in an AV 700 MHz spectrometer.

### 2.2.1 Characterization of the System

The surface of mesoporous silica materials can be complex due to the presence of different types of silica groups and hydroxyls. $^{29}$Si CP-MAS NMR spectra of $PMO_E$ and SBA-15 recorded for the driest states of the samples are shown in Figure 2.3(a,b) respectively. For $PMO_E$, peaks labelled $T_1$ (-47 ppm), $T_2$ (-58 ppm), and $T_3$ (-67 ppm) shown in Figure 2.3(a) arise from those silicon atoms that are connected to the organic environment [$CH_2Si(OH)_2(OSi)$], [$–CH_2Si(OH)(OSi)_2$], and [$–CH_2Si(OSi)_3$], respectively. The $^{29}$Si CP-MAS NMR spectrum shown in Figure 2.3(b) exhibits the well characterized $Q_2$, $Q_3$ and $Q_4$ resonances of SBA-15 with chemical shift values of -92, -103, and -113 ppm, respectively. $^{13}$C CP-MAS NMR spectra of $PMO_E$ and SBA-15 recorded for the driest states of the samples are shown in Figure 2.3(c and d), respectively. The $^{13}$C peak shown in Figure 2.3(c) at 5.3 ppm is due to the bulk $–CH_2–CH_2–$ carbons of $PMO_E$, whereas there was no $^{13}$C signal from SBA-15, as expected. The peaks marked with '*' are from the surfactants.

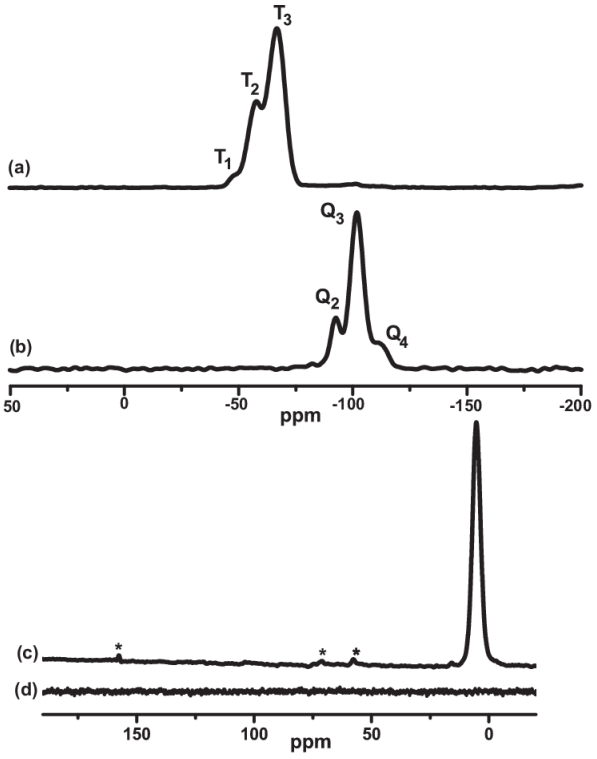


**Figure 2.3** $^{29}$Si and $^{13}$C CPMAS spectra of $PMO_E$ and SBA-15 recorded at 10 kHz are shown in (a and b) and (c and d) respectively. Surfactant peak in the $^{13}$C spectrum are denoted by *.

**2.2.2 Data Analysis**:- All $^1$H proton MAS NMR spectra analysed were deconvoluted into distinct spectral components using the DMFIT program. The total integrated intensity

provided by DMFIT program was used further to estimate the number of protons per $nm^2$ in the pores of the materials under study, as discussed below.

## 2.3 Results and Discussion

### 2.3.1 Analysis of Proton MAS NMR Spectra of $PMO_E$ and SBA-15

In this study, we investigate the distribution of adsorbed water in $PMO_E$ at different hydration levels through proton one pulse MAS NMR spectroscopy. The proton density within the pores is characterised by the parameter *p*, which describes the proton concentration per $nm^2$ at each hydration level of the sample [98,101,102]. With the prior knowledge of the pore surface area (Figure 2.2 and Table 2.1) and the integrated intensity derived from proton MAS NMR spectra at different hydration levels, we calculated the corresponding *p* values. The total integrated intensity was calculated and correlated with the weight loss for both samples, as shown in Figure 2.4(a,b). While increasing or decreasing the hydration levels, we observed that the recorded proton MAS NMR spectra at room temperature for both samples were reproducible, in terms of the chemical shift pattern and total integrated intensity. Based on this observation and the linear dependence of weight loss on the total integrated intensity, we conclude that the hydration process is reversible in the pores of $PMO_E$ and SBA-15.

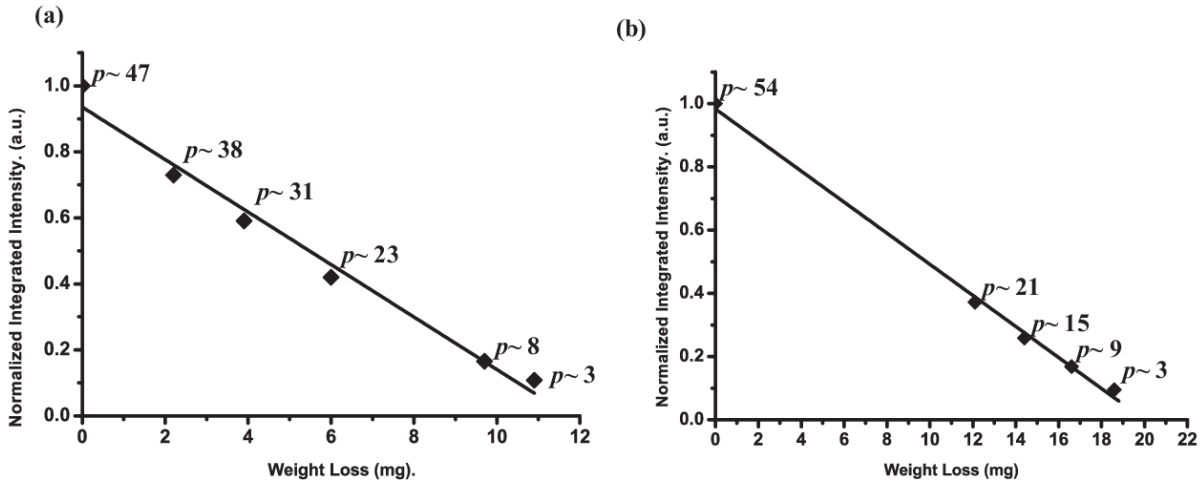


**Figure 2.4** Linear variation of the total integrated intensity of the proton spectrum with respect to weight loss (mg) at various levels of pumping in $PMO_E$ (a) and SBA-15 (b). The corresponding *p* values were calculated at each stage and are shown

The normalized total integrated intensity vs. weight loss shown in Figure 2.4 was plotted and analysed using the linear fit program in Origin@. The program provided the slope and intercept as (-0.079 ± 0.005, 0.93 ± 0.03) for $PMO_E$ and (-0.049 ± 0.002, 0.98 ± 0.03) for SBA-15, respectively. The intercept with the x-axis was 11.7 mg for $PMO_E$ and 20 mg for SBA-15 from which the amounts of dry $PMO_E$ and SBA-15 present in the rotor were calculated as 21.5 mg and 29.6 mg, respectively. Using these values, the total pore surface areas of the samples were estimated as 1.66 x $10^{19}$ $nm^2$ for $PMO_E$ and 2.49 x $10^{19}$ $nm^2$ for SBA-15. From the total pore surface areas, for any hydration level, the number of protons per $nm^2$ was finally evaluated. In this study, for SBA-15, as a function of hydration, the *p* values vary between 3 and 54 H $nm^{-2}$ and for $PMO_E$, the variation is between 3 and 47 H $nm^{-2}$. We approximated the calculated *p* values to the nearest integer.

In contrast to SBA-15, $PMO_E$ has a dipolar $–CH_2–CH_2–$ proton network in its bulk. Therefore, the proton spectra at all hydration levels exhibit a 'broad base' arising from proton–proton dipolar interactions. Hence, for $PMO_E$, the total integrated intensity of the proton spectra also includes the intensities arising from the bulk proton network. The contribution from the bulk $-CH_2-CH_2-$ network does not depend on hydration level, hence information related to its position, line width, and percentage needs to be known in order to estimate *p* and for further analysis of the spectral contributions of bulk water and surface protons in $PMO_E$. In order to extract approximately the dipolar-broadened proton line shape associated with the $–CH_2-CH_2-$ protons, a two dimensional $^1H$-$^{13}C$ wide-line separation experiment was performed at 10 kHz MAS with a short cross polarization contact time. In the WISE experiment, after initial proton excitation, transverse proton magnetization is made to evolve freely during $t_1$ and is transferred to $^{13}C$ through a CP process, followed by $^{13}C$ detection. WISE experiment is widely used in polymers in order to derive heterogeneity of molecular dynamics. In this experiment, the wide $^1H$ NMR lines, overlapping in the 1D spectrum can be well resolved according to the chemical shift of the bonded $^{13}C$ nuclei. Hence, the heterogeneity of mobility is directly extracted from the $^1H$ lineshapes in the $F_1$ dimension.

The projection extracted from the two dimensional wide-line MAS spectrum shown in Figure 2.5 was used to estimate the line width and position of the resonance associated with the $–CH_2-CH_2$ protons in the $PMO_E$ bulk. The proton centreband is located at 2 ppm with a full width at half maxima (FWHM) of ~3200 Hz. Subsequently, the 1D proton spectrum

corresponding to the driest state, with $p$~3H/nm$^2$, of the $PMO_E$ sample has been deconvoluted by incorporating, besides the bulk water and surface proton components, a component centred at ~2ppm and FWHM of ~3200 Hz whose amplitude was optimized, together with the amplitudes and lines widths of all the other components, to get the best fit model. The proton spectrum of the driest state of the sample has been selected for optimization because the signal intensity due to $–CH_2$-$CH_2$-is significant in this case due to less percentage of bulk water and surface protons. Since the amount of $–CH_2$-$CH_2$ protons is constant in the sample at all hydration levels, all $PMO_E$ spectra are deconvoluted by incorporating the broad lineshape component with the same position, amplitude, and linewidth determined for the driest sample. In all deconvolutions, the broad dipolar lineshape at 2 ppm is referred as the 'base'. The spectrum with the best fit at $p$~3 H/nm$^2$ is shown in Figure 2.6.

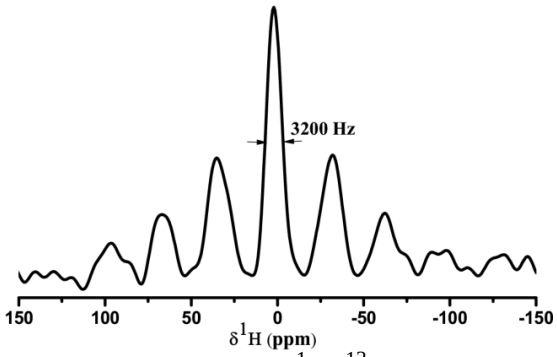


**Figure 2.5** Proton $F_1$ projection extracted from a $^1H\{^{13}C\}$ 2D Wide-line Separation spectrum of $PMO_E$ ($p$ ~ 3 H/nm$^2$) acquired at 10 kHz MAS with a DSX 300 MHz spectrometer at room temperature. The centreband is positioned at 2 ppm, with a FWHM of ~3.2 kHz. The projection is extracted at the maximum of the $^{13}C$ resonance (5.3 ppm).

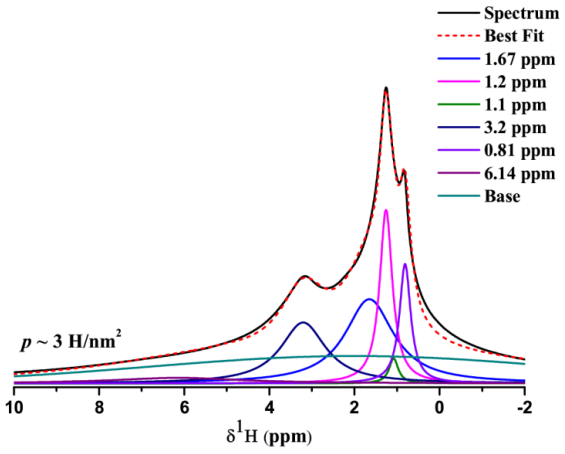


**Figure 2.6** Deconvolution of proton MAS spectrum of $PMO_E$ at $p$~3 H/nm$^2$ using DMFIT.

**2.3.2 Analysis of Proton Spectral Components**:- The inner pore surface of $PMO_E$ is composed of an –O–Si–$CH_2$–$CH_2$–Si–O– network and, upon hydration, water molecules can form hydrogen-bonding networks starting from the silicon–OH groups on the surface. Following Grűnberg et al. and Rosen et al., we refer to these proton–oxygen structures as clusters, situated near to an oxygen site on the surface [99,101,102]. At low to moderate water loading, the presence of different clusters undergoing fast dynamics leads to sufficiently resolved proton spectra displaying characteristic chemical shift ranges. Such characteristic chemical shift ranges can be used to track different cluster types and their contribution in the material under study and at different hydration levels.

The proton spectra of $PMO_E$ and SBA-15 [99,101] exhibit characteristic resonances within a few distinct chemical shift ranges: (i) 5.8–7 ppm, corresponding to protons that are strongly hydrogen-bonded to the silica surface and termed acidic protons, (ii) 4.4–5.2 ppm, corresponding to bulk water, (iii) 3.1–3.4 ppm, corresponding to water molecules that are hydrogen bonded to the surface silanols (–Si–OH + $H_2O$), termed surface protons, (iv) 3.6–4.1 ppm, corresponding to clusters of larger size, (v) 1.6–2.0 ppm, corresponding to isolated Si–OH, and (vi) 1.0–1.1, corresponding to isolated water molecules termed monomers [99].

**(a) $PMO_E$**. The proton spectra of $PMO_E$ at different $p$ values are shown in Figure 2.7(i–v). A representative deconvoluted spectrum along with the total fit (dotted red) is shown in Figure 2.8 for a $p$ value of 29 H $nm^{-2}$ and a few more deconvolutions at various hydration levels are presented in the Appendix Figure A2.1–A2.4. The relative percentages of isolated silanols and water proton resonances at different $p$ (H $nm^{-2}$) values and the ratio between the volume of adsorbed water and the pore volume (%) are given in Table 2.2. This ratio is estimated as $(V_W/V_P) \times 100$, where $V_W$ is the volume of water in the mesopore at a given hydration level and $V_P$ is mean pore volume of the amount of dried sample under study. Starting from the minimum $p$ (H $nm^{-2}$) value of 3, the surface distribution of water at different hydration levels is discussed below. The proton spectrum at $p$ ~ 3 H $nm^{-2}$ was deconvoluted into four lines corresponding to (i) isolated silanols (~42%), (ii) surface water (40.2%), (iii) acidic protons (14.6%) and (iv) monomers (3.2%). Correlating 100% of the protons to a $p$ value of 3 H $nm^{-2}$, we have a maximum of 1.26 isolated silanols per $nm^2$ on the surface, 1.21 surface protons per $nm^2$, and 0.44 and 0.09 protons per $nm^2$ for acidic protons and monomers, respectively. At moderate to high $p$ values, two additional resonances were observed simultaneously in the chemical shift ranges of 3.6–4.1 ppm and 4.4–5.2 ppm. Finally, at the maximum $p$ value of

~47 H nm$^{-2}$, the spectrum is dominated by an asymmetric bulk water peak, which was deconvoluted into two components centred at 4.6 and 4.4 ppm, with ~71% and ~19% relative integrated intensities. The variation in relative integrated intensity of different components with respect to hydration is shown in Figure 2.9. Although the peak corresponding to isolated silanols was not visible in the spectra, assuming a component at the chemical shift value of isolated silanols was necessary for deconvolution, as the experimental spectra could not have been fitted otherwise within the 1.5–2 ppm range. Still, in order to directly confirm the presence of isolated silanols, we performed a 1D $^{1}$H MAS NMR experiment at fast MAS (60 kHz) for $p$ ~ 3 H nm$^{-2}$, and a proton resonance at 1.7 ppm was observed corresponding to the range of isolated silanols, as shown in Figure 2.10.

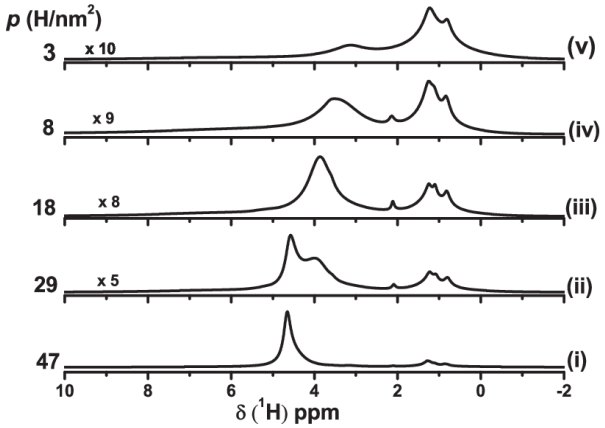


**Figure 2.7** Proton MAS spectra of $PMO_E$ for various $p$ values. The spectral intensity is scaled with respect to $p$ ~ 47 H nm$^{-2}$ and the multiplication factor is displayed on the left side of each spectrum.

**Table 2.2** Relative percentages of isolated silanols and water protons and the ratio between the volume of adsorbed water and the pore volume ($V_W/V_P$ %) (calculated with respect to the specific pore volume) in $PMO_E$ tabulated for different $p$ (H nm$^{-2}$) values. The total integrated intensity includes contribution from peaks in the 0.8-1.5 ppm range.

| $p$ (H/nm$^2$) | 1.6-1.7 ppm (%) | 3.1 -3.4 ppm (%) | 3.6-4.1 ppm (%) | 4.4-5.2 ppm (%) | 5.8-6.6 ppm (%) | $V_W/V_P$ (%) |
|---|---|---|---|---|---|---|
| 3 | 42 | 40.2 | | | 14.6 | 4.1 |
| 8 | 20.1 | 11.8 | 46.6 | | 18.5 | 11.1 |
| 18 | 11.2 | 4.5 | 66.7 | | 14.6 | 25.0 |
| 20 | 10.1 | 4.3 | 65.7 | 2.7 | 14.9 | 27.8 |
| 23 | 7.2 | 4.4 | 48.7 | 24.4 | 11.4 | 32 |
| 29 | 7.1 | 2 | 46.7 | 31.5 | 8.9 | 40.3 |
| 31 | 5.3 | | | 83.2 | 8.3 | 43.1 |
| 38 | 3.6 | | | 85.2 | 7.7 | 52.8 |
| 47 | 2.5 | | | 90.2 | 4.8 | 65.4 |

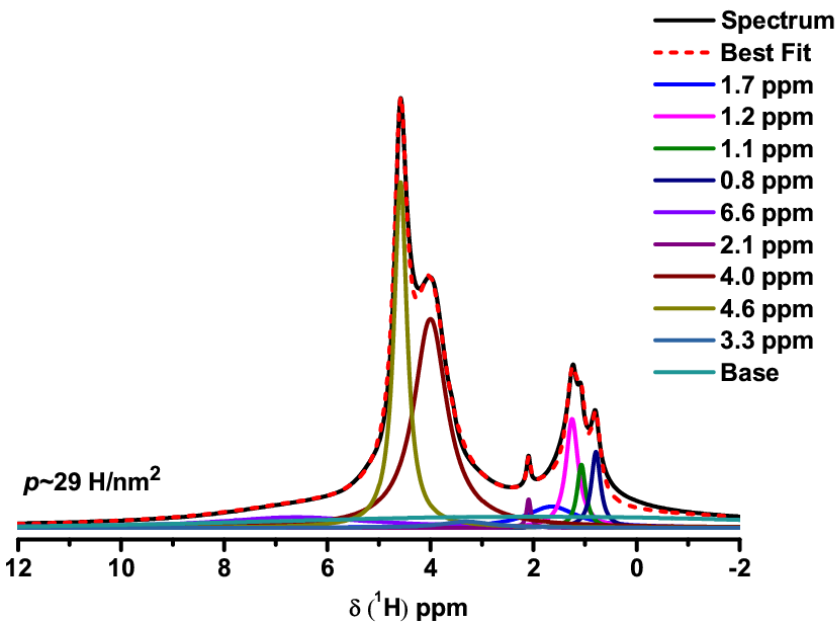


**Figure 2.8** A representative deconvolution of the proton MAS spectrum of $PMO_E$ at $p$ ~ 29 H $nm^{-2}$ using DMFIT.

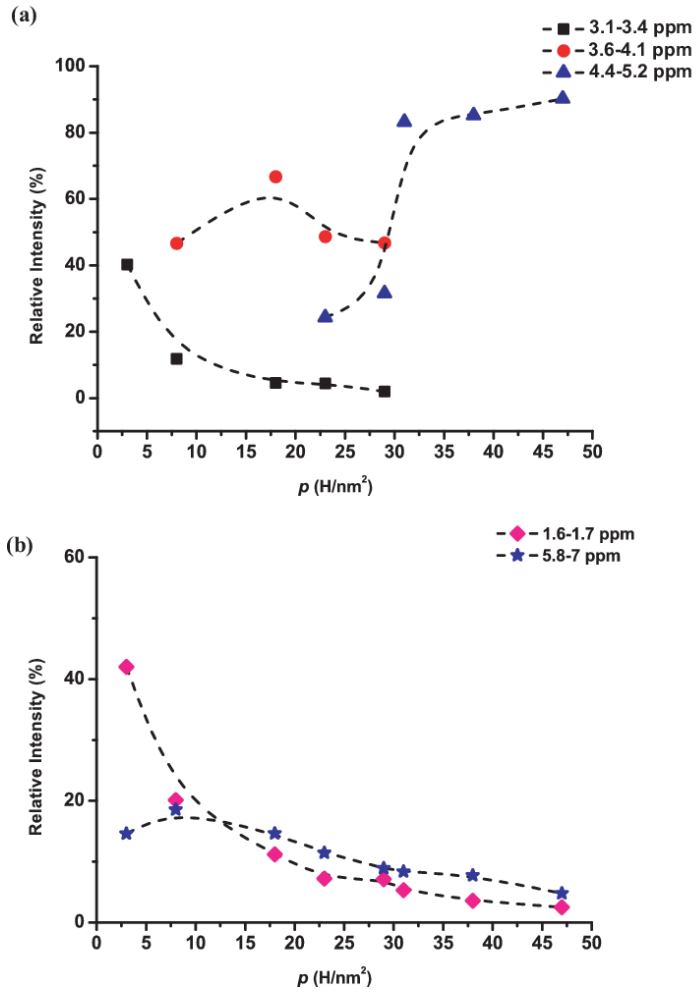


**Figure 2.9** Variation of the relative intensity percentage as a function of $p$ in $PMO_E$, for (a) bulk and surface water protons and (b) isolated silanols and acidic protons.

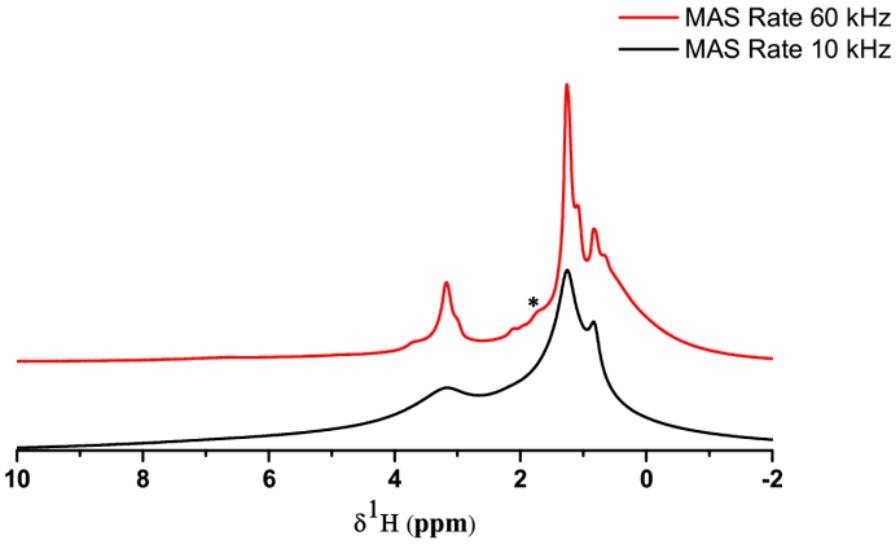


**Figure 2.10** Proton MAS spectrum of $PMO_E$ at $p$ ~ 3 H/nm$^2$ recorded at MAS rates of 60 kHz (red) in a 700 MHz spectrometer and 10 kHz (black) in a 300 MHz spectrometer. The proton resonance corresponding to 1.7 ppm is marked by (*).

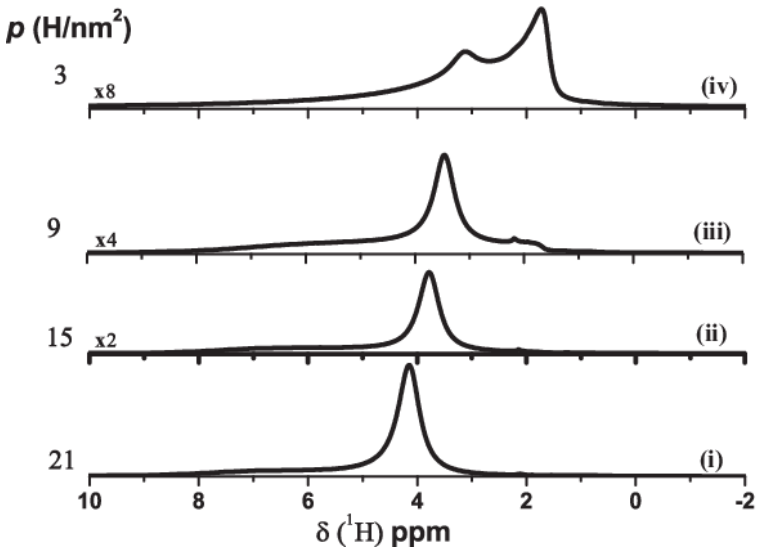


**Figure 2.11** Proton MAS spectra of SBA-15 at different $p$ values.

**(b) SBA-15**. Figure 2.11(a(i–iv)) shows the proton MAS NMR spectra of SBA-15 recorded at different hydration levels, with $p$ (H nm$^{-2}$) values ranging from 3 to 21. The relative percentages of the isolated silanols and water proton resonances given in Table 2.3 are plotted in Figure 2.12(a, b) as a function of $p$ (H nm$^{-2}$). A few deconvolutions of SBA-15 spectra for various hydration levels are given in Appendix Figure A2.5–A2.8. At the lowest $p$ value of ~3 H nm$^{-2}$, SBA-15 contains about 57.2% isolated silanols, 31.7% surface water and

11.1% acidic protons. Therefore, on the surface of SBA-15, at $p$ ~ 3 H nm$^{-2}$, we have a maximum of 1.72 silanols per nm$^2$, 0.95 surface protons per nm$^2$ and 0.33 acidic protons per nm$^2$. With an increase in $p$ value, the resonance observed in the 3.1–3.4 ppm range gradually shifts to a lower field. Finally, at $p$ ~ 54 H nm$^{-2}$, the spectrum is dominated by an asymmetric resonance in the bulk water range, which we deconvoluted into two components centred at 4.6 ppm and 4.4 ppm, with 56% (FWHM 0.2 ppm) and 41% (FWHM 0.4 ppm) relative intensity, respectively.

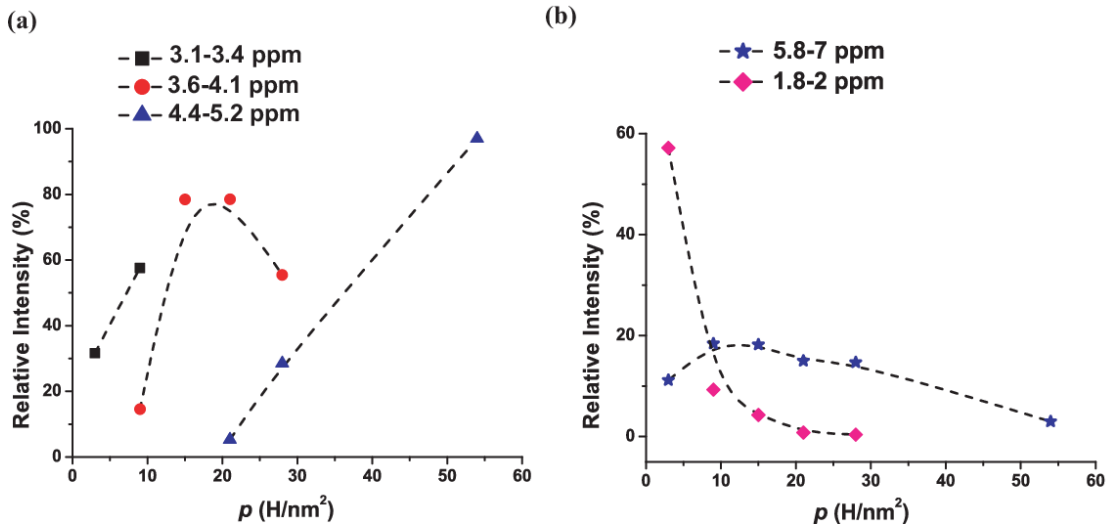


**Figure 2.12** Variation of the relative intensity percentage as a function of $p$ in SBA-15 for (a) bulk and surface water protons and (b) isolated silanols and acidic protons

**Table 2.3**. Relative percentages of isolated silanols and water protons and the ratio between the volume of adsorbed water and the pore volume ($V_W/V_P$ %) (calculated with respect to the specific pore volume) in SBA-15 tabulated for different $p$ (H nm$^{-2}$) values.

| $p$ (H/nm$^2$) | 1.8-2 ppm (%) | 3.1-3.4 ppm (%) | 3.6-4.1 ppm (%) | 4.4-5.2 ppm (%) | 5.8-7.0 ppm (%) | $V_W/V_P$ (%) |
|---|---|---|---|---|---|---|
| 3 | 57.2 | 31.7 | | | 11.1 | 3.0 |
| 9 | 9.3 | 57.7 | 14.6 | | 18.4 | 9.1 |
| 15 | 4.3 | | 78.5 | | 18.2 | 15.2 |
| 21 | 0.8 | | 78.5 | 5.3 | 15.4 | 21.2 |
| 28 | 0.4 | | 55.5 | 28.6 | 14.7 | 28.3 |
| 54 | | | | 97 | 3 | 54.6 |

**(c) Dynamics of Water Clusters**. Based on the analysis of the proton spectra of both $PMO_E$ and SBA-15, we discuss the distribution and dynamics of water molecules on the surface of these materials in terms of water clusters. At low to moderate $p$ values, the protons within the clusters are exchanging quickly, and hence the chemical shift associated with a given cluster is approximately the average of the proton chemical shifts of the protons within it. The

distinct chemical shifts of the clusters indicate that proton exchange between the clusters is slow when compared to the rapid exchange within the clusters. We define the size of a cluster, x, as the number of protons present in it. For isolated silanols (1.6–2.0 ppm), the cluster size is x = 1, whereas for monomers and acidic protons, due to the presence of single water molecules, the cluster size is x = 2. Proton resonances in the range 3.1–3.4 ppm correspond to single water molecules interacting with Si–OH protons, thus the size of the clusters for this chemical shift range corresponds to x = 3. With the addition of one or more water molecules, the average chemical shift changes due to fast exchange in the 3.6 to 4.1 ppm range. The resonances in the above range correspond to a cluster of size $x \geq 4$.

At low to moderate hydration levels, water molecules bind to the surface in clusters of smaller size. An estimate of cluster sizes and their contribution can be obtained from the integrated intensity of different spectral components at low to moderate water loading. The variation in integrated intensity of different water clusters present in SBA-15 as a function of their size is shown in Figure 2.13(a). At $p \sim 3$ H nm$^{-2}$, there is no contribution from clusters with $x \geq 4$. With an increase in $p$ from 3 to 9 H nm$^{-2}$, the intensity of the isolated silanols (x = 1) reduces, whereas the intensity of acidic (x = 2) and surface protons (x = 3) increases. As hydration increases from 3 to 9 H nm$^{-2}$, more water molecules attach to the surface through hydrogen bonding with the silanols, hence silanol intensity reduces. Simultaneously, more surface water clusters (x = 3) are formed and a small amount of clusters with $x \geq 4$ is also observed. Increasing the hydration further, at $p \sim 15$ H nm$^{-2}$, the contribution from x = 1 reduces further, and there is no observable contribution from the surface protons. Instead, we observe a significant increase in the intensity due to clusters with $x \geq 4$.

The variation of integrated intensity of different water clusters present in $PMO_E$ as a function of their size is shown in Figure 2.13(b). At $p \sim 3$ H nm$^{-2}$, the main contribution is due to isolated silanols and surface protons. There is no contribution from clusters with $x \geq 4$ at this hydration level. As $p$ increases from 3 to 18 H nm$^{-2}$, the intensity of the isolated silanols (x = 1) and surface protons (x = 3) reduces, whereas the intensity of acidic (x = 2) protons increases. The observed intensity due to clusters with $x \geq 4$ increases significantly from $p$ = 8 to 18 H nm$^{-2}$. We would expect a significant decrease in isolated silanol intensity with hydration, but instead, we observe a moderate decrease in intensity. This may be due to the existence of isolated silanol sites or pore segments that are not accessible to water molecules [140]. Further experimental evidence is needed to elucidate the nature of this behaviour. Inspection of Figure 2.13 shows that $PMO_E$ pores get filled with water at lower $p$

values in comparison to those of SBA-15. This observation is supported by the lower pore diameter in $PMO_E$ when compared with that of SBA-15.

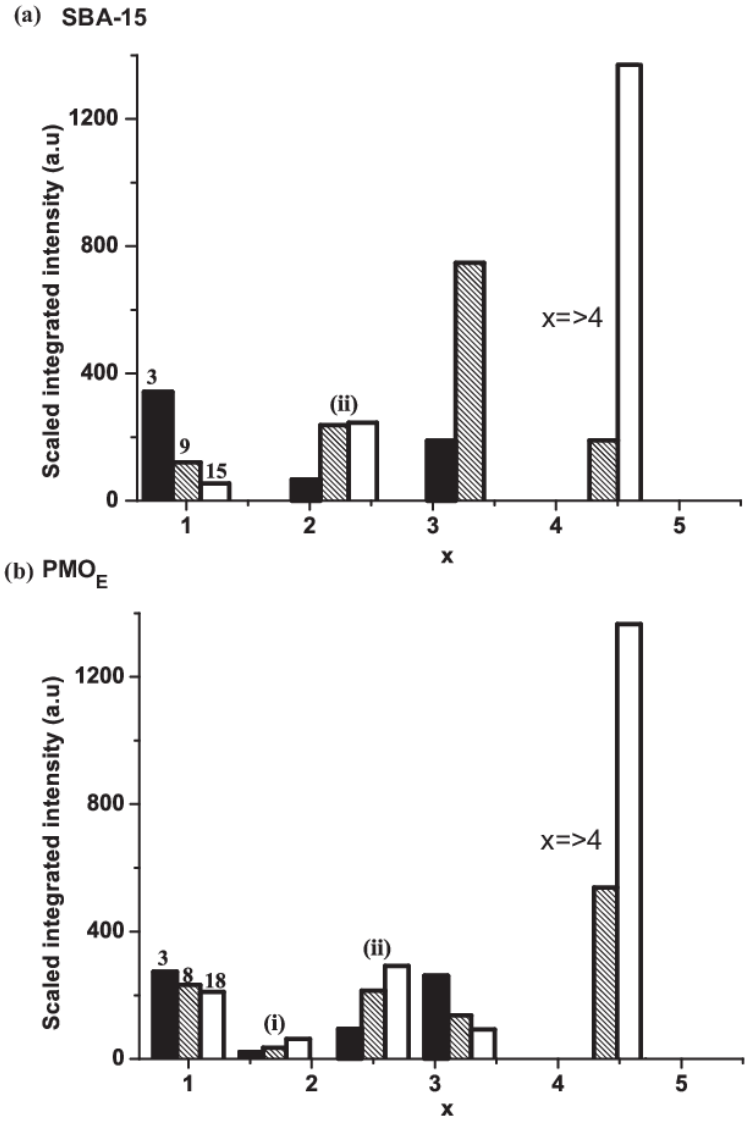


**Figure 2.13**

Cluster distribution in (a) SBA-15 at $p$ ~ 3 (solid), ~9 (lines) and ~15 (white) and in (b) $PMO_E$ at $p$ ~3 (solid), ~8 (lines) and ~18 (white). Monomers are represented by (i) and acidic protons by (ii). For $PMO_E$ and SBA-15, the proton spectra at $p$ ~ 18 H $nm^{-2}$ and $p$ ~ 15 H $nm^{-2}$, respectively, are scaled to an arbitrary value (2000 a.u.). Intensities of all spectra are scaled accordingly.

To justify the above statement we have calculated the maximum number of water molecules that could accommodate within SBA-15 and $PMO_E$ pores. From BET measurements the total pore surface area corresponding to the amount of dried sample within the rotor is estimated as $24.893*10^{18}$ $nm^2$ for SBA-15, and $16.6*10^{18}$ $nm^2$ for $PMO_E$. Since one water molecule corresponds to an area of 10.6 $Å^2$ [168], irrespective of the sample under study, ideally 9 water molecules/$nm^2$ are required for monolayer formation, amounting to $p = 18\ \mathrm{H/nm^2}$.

The above results emphasis the presence of 6 silanols/$nm^2$ in the sample, a value which is significantly higher than the generally accepted silanol density (3-4 silanol/$nm^2$) for

fumed silicas [131]. In this study we have estimated that a maximum of 2 and 1.6 silanol/nm$^2$ is present in SBA-15 and $PMO_E$ respectively. Accordingly in SBA-15, two water molecules can form hydrogen bonding with them, resulting in a $p$ value of $\sim 6\ H/nm^2$. From this, we may conclude that, at $p \sim 6\ H/nm^2$ monolayer may be formed and for any higher $p$ values, cluster formation may be observed. This is further confirmed by the SBA-15 proton MAS NMR spectrum from $p \sim 9\ H/nm^2$ on wards (Fig. 2.12 & 2.13). For SBA-15 it is estimated that about 60 water molecules ($p \sim 120\ H/nm^2$) are required to completely fill the pore volume enclosed in a pore cylinder of 1 nm$^2$ lateral surface area. Similarly, in the case of $PMO_E$, about 26 water molecules ($p \sim 52\ H/nm^2$) are required to fully fill the pore volume enclosed in a pore cylinder of 1 nm$^2$ lateral surface area. In our experimental samples, at highest hydration level, the pores of $PMO_E$ are 90% filled whereas for SBA-15 the pores are 45% filled. Therefore the pores of both materials are partially filled, but at lower $p$ values the pores of $PMO_E$ are filled more when compared with SBA-15. In the case of $PMO_E$ because of the presence of $–CH_2$-$CH_2$- in the silica network, the surface density of silanols is reduced when compared with SBA-15. This may result in the cluster formation at lower $p$ values. This can be seen from the experimental observation provided in Fig. 2.13, at $p$~ 8 H/nm$^2$.

### 2.3.3 Dynamics, Water Layers, and Pore Filling in $PMO_E$ and SBA-15

Based on Figure 2.9, 2.12, and 2.13, we now compare the dynamic behaviour of protons in both samples. We can picture the pores or pore segments in the samples as covered with water layers of different thickness. Generally, one can expect a distribution of layers with respect to thickness, the change of the distribution with hydration, and that this distribution (with its characteristic centre, width, and line shape) has a signature in the proton NMR spectrum. For example, a broader distribution would lead to a larger line width of the observed resonance. We show below that important information can be gathered about the distribution of water layers at different hydration levels from the analysis of the proton spectra.

In SBA-15, starting from the dry state of $p$ ~ 3 H nm$^{-2}$, the proton resonance at 3.1 ppm with a relative intensity of 31% shifts to 3.4 ppm at $p$ ~ 9 H nm$^{-2}$. A further gradual shift of the proton line to a lower field is observed with an increase in $p$ from 15 to 54 H nm$^{-2}$. Finally, at $p$ ~ 54 H nm$^{-2}$, an asymmetric peak can be observed, which we deconvoluted into two components centred at 4.6 ppm and 4.4 ppm. For a water layer of a given thickness, the fast exchange results in an average proton chemical shift. A thicker layer would result in an

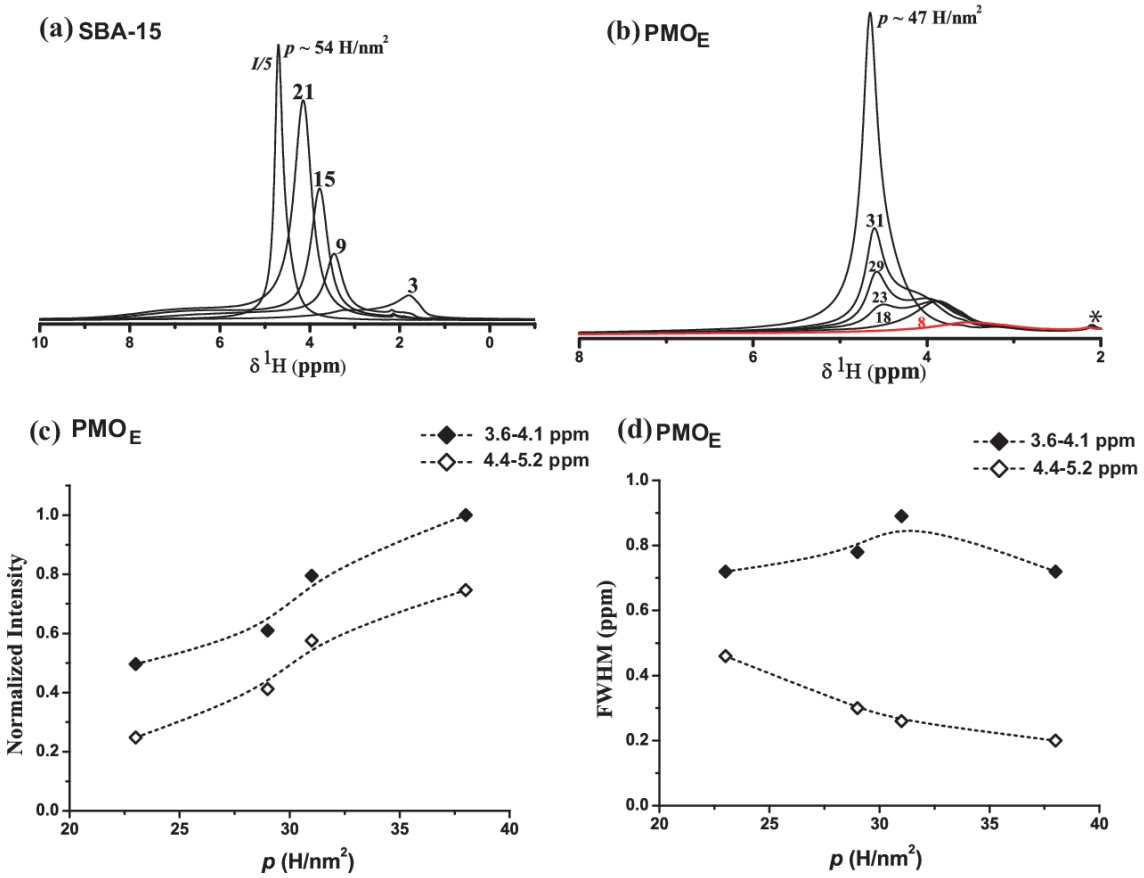


**Figure 2.14** Overlaid normalized proton spectra of (a) SBA-15 and (b) $PMO_E$ acquired at various *p* values. The impurity peak at 2.1 ppm is shown with a (*). (c) Normalized intensities as a function of *p* for the 3.6–4.1 ppm and 4.4–5.2 ppm resonances in $PMO_E$. (d) Corresponding FWHM as a function of *p* value.

average chemical shift positioned more towards the bulk water chemical shift (4.4–5.2 ppm). The smooth variation in proton chemical shift to a lower field shown in Figure 2.14(a) can thus be attributed to a gradual increase in the thickness of water layers with an increase in hydration. This gradual increase in thickness of water layers with hydration also suggests that the pore filling mechanism is predominantly radial. The resonance observed in the range 3.6–4.1 ppm thus corresponds to a distribution of water layers of different thickness centred on some average layer thickness. For SBA-15, this model was already proposed by Buntkowsky and co-workers based on analysis of $^1$H MAS NMR spectra [99]. The distribution of adsorbed water on the pore surface of SBA-15 studied here is similar to that reported by Buntkowsky et al., which is reasonable as the pore diameters of SBA-15 in both studies are very similar (7 *vs*. 8 Å).

In $PMO_E$, the proton resonance observed at 3.1 ppm in the dry state ($p$ ~ 3 H $nm^{-2}$) shifted to 3.9 ppm at 18 H $nm^{-2}$ and its intensity increased (Figure 2.14(b)). With a further increase in $p$ to 23 H $nm^{-2}$, besides the 3.9 ppm peak, a new resonance appears at 4.5 ppm. Increasing the level of hydration further towards 47 H $nm^{-2}$, the 4.5 ppm resonance shifts very slightly towards a lower field with an increase in relative intensity while the 3.9 ppm peak shifts significantly towards the 4.5 ppm resonance and decreases in relative intensity. At $p$ ~ 47 H $nm^{-2}$, only one peak is present at around 4.5 ppm and it exhibits an asymmetric line shape. The asymmetric peak was deconvoluted into two components at 4.4 and 4.6 ppm, similar to SBA-15 at $p$ ~ 54 H $nm^{-2}$.

The resonance in the 3.6–4.1 ppm range behaves similarly to that observed in SBA-15, therefore it can be attributed to a water layer distribution showing a gradual increase in the average water layer thickness with an increase in hydration. The fact that the second resonance is observed in the range of bulk water implies that it corresponds to fully or almost filled pores or pore segments. The simultaneous presence of both resonances and their behaviour upon hydration imply that at moderate to high water loadings, the layer thickness distribution must be the sum of two contributions. One of them corresponds to fully or almost fully filled pores and the other one is peaked at an average thickness, which increases on hydration.

A similar behaviour was observed in MCM-41 by Buntkowsky and co-workers [99], where the coexistence of partially filled and fully filled pore segments was inferred from $^1H$ MAS NMR spectra. They also proposed that the pore filling process is predominantly axial in MCM-41. Their conclusions are relevant to $PMO_E$ as the pore diameters of MCM-41 (3.3 nm) and $PMO_E$ (3.0 nm) are similar. Based on the analysis of the $^1H$ MAS NMR studies on $PMO_E$, we observed that from low to moderate $p$ values, the proton resonance corresponding to 3.1–3.4 ppm steadily shifts to a lower field. Although its relative percentage decreases, the absolute intensity of this resonance steadily increases which suggests a radial pore filling mechanism. As $p$ increases above 18 H $nm^{-2}$, this resonance continues to shift and grow in intensity, as shown in Figure 2.14(c), such that radial filling must still take place. However, the presence of the 4.5 ppm resonance that corresponds to filled or almost filled pore segments and its increase in intensity with hydration (Figure 2.14(c)) suggests that axial filling must also occur. Inspection of Figure 2.14(c) shows that the rates of increase for both resonances are very similar, which indicates that the rates of radial and axial filling are also similar. Therefore, we conclude that in $PMO_E$, both axial and radial filling play a significant

role in the process of hydration at moderate to high *p* values. In Figure 2.14(d), the line widths of the two main resonances are displayed at moderate to high hydration levels. The increase and subsequent decrease in line width of the 3.6–4.1 ppm resonance may indicate that the contribution to water thickness distribution of partially filled pore segments becomes broader and subsequently narrower with an increase in hydration in the considered *p* value range. On the other hand, the steady decrease in line width of the 4.4–5.2 ppm resonance suggests a monotonous decrease in 'line width' of the contribution to water thickness distribution corresponding to filled or almost filled pore segments. However, a change in line width of NMR resonances can also be due to changes in the genuine relaxation process due to a change in molecular dynamics, etc.

## 2.4. Conclusions

The adsorption of water in two different mesoporous materials, $PMO_E$ and SBA-15, has been studied using proton MAS solid state NMR spectroscopy. Through the analysis of the NMR spectra, we have systematically studied the distribution of bulk and surface water protons in both materials as a function of hydration.

By correlating the weight gain of the samples to the total integrated intensity of the recorded proton spectra at each hydration level, we have calculated the number of protons per $nm^2$ ($p$ H $nm^{-2}$) on the pore surface. Proton resonances observed at various hydration levels have been deconvoluted within several chemical shift ranges corresponding to (a) isolated silanols, (b) surface protons, (c) protons undergoing fast exchange within clusters of larger size, (d) bulk water, (e) acidic protons, and (f) monomers. The variation in relative integrated intensity of bulk and surface water components has been interpreted in terms of clusters and distributions of water layers.

We performed an analysis of the NMR spectra in terms of water cluster size and their contributions for both samples at low to moderate *p* values. We observed that clusters of larger size are formed at lower *p* values in $PMO_E$ in comparison to SBA-15. This means that the pores of $PMO_E$ are getting filled with water at lower hydration levels. The smaller pore diameter of $PMO_E$ supports this conclusion. The formation of clusters on the surface of $PMO_E$ eventually leading to pore filling results from the interplay between the hydrophobic methylene bridges that reduce the effective adsorptive surface area and the lower pore diameter

. Contrary to our expectations and in contrast to SBA-15, with an increase in hydration in $PMO_E$, we did not observe a significant decrease in the intensity of isolated silanols. This may be due to the existence of isolated silanol sites or pore segments that are not accessible to water molecules in $PMO_E$. Further experimental evidence is needed to elucidate the nature of this behaviour.

For $PMO_E$ at moderate to high *p* values, the simultaneous presence of two major resonances (at 3.6–4.1 ppm and 4.4–5.2 ppm) and their behaviour upon hydration imply that the water dynamics can be described in terms of a water layer distribution that is a sum of two contributions, one corresponding to fully or almost fully filled pores and the other one being peaked at an average layer thickness that increases on hydration. The asymmetry of the bulk water peak observed at the highest hydration level of the sample can be attributed to the gradual overlap of the two contributions with increasing hydration. The similar increase in intensity of resonances situated in the 3.6–4.1 ppm (corresponding to partially filled pore segments) and 4.4–5.2 ppm ranges (corresponding to fully or almost filled pore segments) suggests that both radial and axial filling mechanisms play a significant role in the hydration process. For SBA-15, the smooth variation in proton chemical shift to a lower field has been attributed, in agreement with previous studies, to the gradual increase in the average thickness of water layers with an increase in hydration and to a pore filling mechanism that is predominantly radial. For $PMO_E$ at low to moderate *p* values, the main dynamic resonance observed gradually shifts to a lower field in the range 3.1–3.8 ppm and increases in intensity. Therefore, for $PMO_E$ at low to moderate p values, the pore filling mechanism must also be predominantly radial.

We have proposed a connection between spectral line widths and the water thickness distribution in $PMO_E$ according to which narrowing or broadening of the two major resonances is due to narrowing or broadening of the water thickness distribution. Further information is needed to confirm this. The information on surface water distribution, cluster dynamics, pore filling mechanism etc. derived from proton MAS NMR study may be further used for understanding the catalytic properties of $PMO_E$. Similar approaches can be useful in the context of understanding the properties of other periodic mesoporous organosilicates and other similar systems as they may provide information about the surface inhomogeneity, mobility of guest molecules on the surface, etc.

# 3

# Dynamics in Amine-Functionalized Hybrid Materials

Grafting of organic components to the silica network of organosilane-based materials plays an important role in the development of new materials [144-146]. The existence of efficient ways to introduce organic groups onto the surface of mesoporous materials as a means to tailor their properties has widened their industrial applications and enriched the research avenues [147,148]. Such hybrid materials have the potential to outperform the current biomaterials in terms of their mechanical properties and have played a major role in orthopaedic and dental applications, cancer therapy etc.

One of the commonly used precursors for the preparation of functionalized groups is 3-glycidoxypropyltrimethoxysilane (GPTMS) because of its versatile applications, such as antiscratch coatings, solid electrolytes, anticorrosion coatings, etc. [149-151]. GPTMS is also used as part of hybrid materials in optical wave guides, optical limiting, structured layers in microelectronics, and electrically conductive films, and for the preparation of second order nonlinear materials [152]. Because of the wide range of applications, the physicochemical properties of GPTMS are under continuous investigation [153-156]. The dynamic behaviour of water molecules in hydrated polymethacrylate has been examined by Yamada-Nosaka et al. [155]. The above studies highlight the correlation between function and molecular structure or dynamics. For correlating and widening the possibilities of these materials for varied applications, it is very important to understand the changes in dynamics under different conditions in host−guest systems.

The aim of the study presented in this chapter is to understand the molecular dynamics of amine functionalized mesoporous materials through deuterium and proton solid state MAS NMR. Polyfunctional amines are popular curing agents for fabrication of organic polymers based on the epoxy-amine system [157,158]. Amine functionalized hybrid materials are in wide use for $CO_2$ capture and in biomimetics where the functional efficiency depends on the kinetics of the linkers and the rate of adsorption of the mesoporous materials [159,160]. Understanding of the physical microstructure of amine functionalized mesoporous materials is important in assessing the $CO_2$ transport behaviour. It has been reported that in various amine functionalized mesoporous silica, the $CO_2$ uptake is governed by hindering or un-hindering of the amine groups by Si−OH on the surface [159,160]. In hemodialysis, usage

of mesoporous silica with amine functionalization has enabled the adsorption of more layers of urea within the mesopores. Amine functionalized propyl hydrocarbon chains help in better packing of chemisorbed urea and hence have high potential in the design of an artificial kidney [161].

In this study, we have covalently bonded methylene-deuterated diamines as tethered groups in two widely used functionalized materials to monitor its dynamics. Two samples were synthesized by grafting 3-GPTMS or 3-(trimethoxysilyl)propyl methacrylate (3-MATMS) as an organic linker on SBA-15, and through post grafting a methylene *deuterated diamine* is attached as a pendent group to both. Proton and deuterium solid state one pulse NMR experiments under magic angle spinning (MAS) were performed at two hydration levels and temperatures ranging from 253 to 315 K. Since deuterium is selectively introduced through the diamines, deuterium MAS NMR lineshape analysis is performed for obtaining molecular dynamic information. Further, molecular dynamic simulations are performed to understand the conformations associated with dynamics and the results are compared with NMR observations.

## 3.1 Materials and Methods

**3.1.1 Synthesis of Mesoporous Deuterated Organofunctionalized SBA-15 Catalysts.** SBA-15, a mesoporous silica, was synthesized by sol−gel hydrothermal method by using Pluronic 123 (P123) as surfactant and tetraethylorthosilicate (TEOS) as silica precursor in acidic medium and detailed procedure is mentioned in previous literature. The surface modification of SBA-15 has been performed by the anchoring of (3-glycidyloxy propyl)trimethoxysilane (3-GPTMS) [157,158] or 3-(trimethoxysilyl)propyl methacrylate (3-MATMS) as organic linker on SBA-15 through postgrafting method [162]. The synthetic procedure is explained as 0.5 g of pretreated SBA-15 at 110 °C for 3 h in 10 mL toluene was reacted with 0.25 and 0.5 milli moles of GPTMS and MATMS organic linkers respectively at 95 °C for 10 h under inert atmosphere. After 10 h, the reaction mixture was cooled, filtered, and washed with toluene followed by dichloro-methane. The material was dried at 70 °C for 12 h and solvent extracted with a Soxhlet apparatus by using dichloromethane as a solvent to remove the unreacted organic modifiers.

The surface modified SBA-15 materials, glycidyloxy-functionalized SBA-15 (GP@SBA-15) or methacrylate-functionalized SBA-15 (MA@SBA-15), were treated with

ethylene-d4-diamine (0.25 and 0.5 mmol respectively; taken in a ratio 2:1 with respect to the moles of organic linkers) in 8 mL of toluene at 70 °C for 16 h under $N_2$ conditions. The material was filtered, thoroughly washed with an excess amount of toluene and dichloromethane to remove the excess amount of deuterated diamines, dried at 50 °C for 12 h, and designated as d4-GPN@SBA-15 (Scheme 1) and $d_4$-MAN@SBA-15 (Scheme 2).

**Scheme 1**. Synthesis of Deuterium-Based Glycidyloxy-Functionalized SBA-15 Catalyst

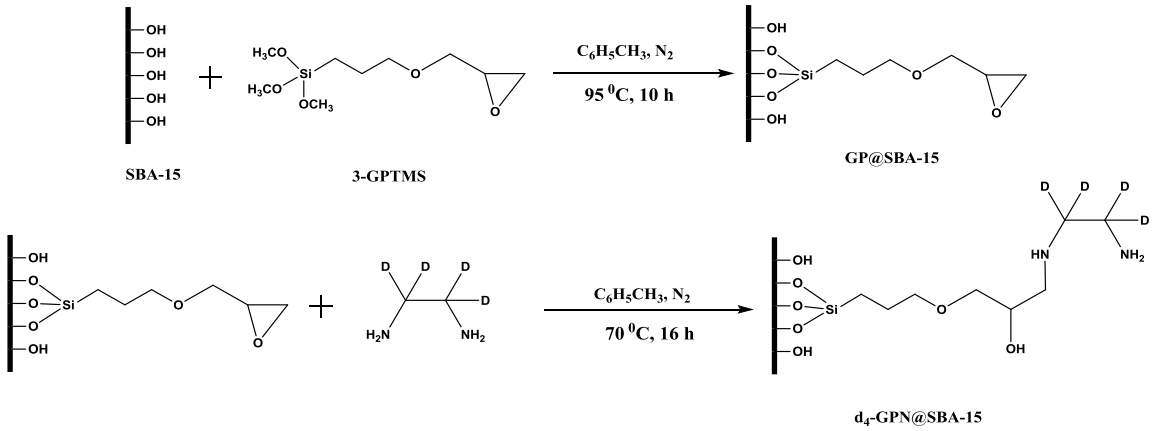


**Scheme 2.** Synthesis of Deuterium-Based Methacrylate-Functionalized SBA-15 Catalyst

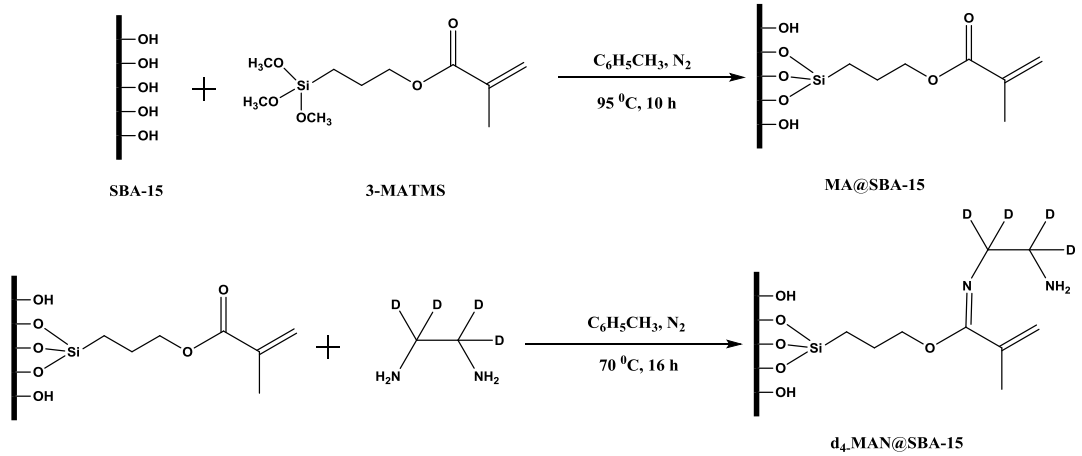


**3.1.2 Sample Preparation**. The samples were vacuum-dried and packed in two separate 4 mm rotors. The wetting of the sample and further drying was similar as in previous publications [1001,102,127,135,137,163]. The rotors with cap open were kept in a separate closed environment and were exposed to a definite amount of double distilled water (a few microliters) for more than 24 h. The proton NMR spectra recorded subsequently were reproducible when correlated to sample weight gain and loss. Hence, we conclude that adsorbed water molecules are uniformly distributed within the sample. We made four

samples, two each for diamine-GPTMS and diamine-MATMS, respectively. We refer the samples as "dry" or "wet", depending on the relative degree of water adsorption. The schematics of the two linkers bonded in $T_3$ configuration are shown in Figure 3.1(i, iv) respectively.

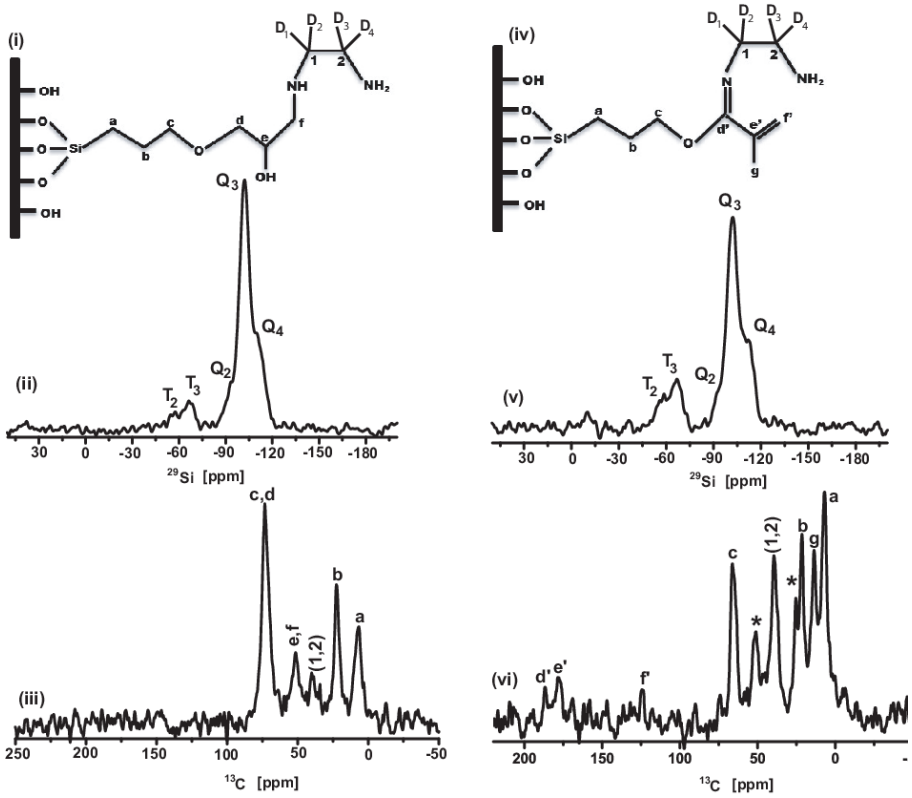


**Figure 3.1** Schematic of (i) diamine-GPTMS, and (iv) diamine-MATMS linkers in $T_3$ binding configuration to SBA-15 surface. Position of the deuterated methylene carbons in the linkers are marked as (1, 2). $^{29}$Si and $^{13}$C CPMAS spectra of post grafted diamine-GPTMS (ii, iii) and of post grafted diamine-MATMS (v, vi), recorded at 298 K and 10 kHz MAS in the dry state.

**3.1.3 Solid State NMR**. $^{1}$H and $^{2}$H MAS NMR spectra were recorded with a 700.13 MHz Bruker Avance$^{+}$ NMR spectrometer equipped with 4 mm MAS probe. Proton one pulse experiments were performed at a spinning rate of 10 kHz, $^{1}$H 90° pulse length was 2.5 μs, and the recycle delay was 4 s. $^{2}$H spectra were recorded with a recycle delay of 1 s, MAS rate of 6666 Hz, and a 90° pulse length of 3.5 μs. $^{29}$Si and $^{13}$C CPMAS spectra of both the samples post grafting of the deuterated diamines were recorded with a DSX 300.13 MHz Bruker

NMR spectrometer, at a MAS rate of 10 kHz, and high power proton decoupling. The CP contact time for $^{13}C$ and $^{29}Si$ was 1 and 5 ms, and the number of transients acquired was 40,000 and 30,000 respectively. All deuterium spectra were processed using MatNMR [164]. Time domain data was left shifted until the first echo and Fourier transformed with a line broadening of 100 Hz.

**3.1.4 Basic Setup of Molecular Dynamic Simulations**. MD simulations were performed using Materials Studio [105]. The basic setup of MD is explained in chapter 1, section 1.3 and in [127,136]. Care was taken to sparsely distribute silanols along the accessible region of anchored diamine-GPTMS and diamine-MATMS.

## 3.2 Results and Discussion

**3.2.1 Spectral Analysis.** $^{29}Si$ CPMAS spectra of diamines-GPTMS and diamine-MATMS, at the driest state are shown in Figure 3.1. Apart from the well reported $Q_2$, $Q_3$, and $Q_4$ configurations of silicon in mesoporous silicates with chemical shifts −92 ppm, −103 ppm, and −112 ppm, additional peaks are observed at −58 ppm and −67 ppm corresponding to molecules which are covalently bonded to a silicon atom and anchored to the surface through two oxygen atoms ($T_2$) and three oxygen atoms ($T_3$) respectively. $T_2$ corresponds to an intermediate state during synthesis, $[(OH)(O)_2Si\text{-}(CH_2)_3OCH_2CH(OH)\text{-}CH_2NH\text{-}(CD_2)\text{-}(CD_2)\text{-}NH_2]$, or it may arise from the ethoxy $[-O-CH_2-CH_3]$ which was used (TEOS) during the synthesis of SBA-15. $T_3$ corresponds to the molecular formula $[(O)_3Si(CH_2)_3OCH_2CH(OH)CH_2NH\text{-}(CD_2)\text{-}(CD_2)\text{-}NH_2]$. Direct covalent binding of deuterated diamine as $-(O)_3Si\text{-}NH\text{-}(CD_2)\text{-}(CD_2)\text{-}NH_2$ and its variants is another possibility, but the $^{29}Si$ CPMAS spectra of both the samples did not show additional vicinal and geminal (−85 ppm, −75 ppm) chemical shifts of silylamines [165]. Even though a quantitative estimation is not possible from the CPMAS spectra, since the percentage of grafting is low, the relative percentage of the $T_n$ sites can be compared. The relative percentage of $T_3(T_2)$ in diamine-GPTMS *vs* diamine-MATMS is 7.54(4.59) versus 12.6(8.3). This is reasonable as the grafting concentration of linkers and diamines in MATMS is twice when compared with diamines-GPTMS. In the present work we have not estimated the grafting and diamine coupling efficiencies. In both cases, more linkers are grafted in $T_3$ configuration, and the ratio of $T_3/T_2$ in both samples is comparable, ∼1.6. The relative percentage of $Q_2$ in diamine-GPTMS is about 11.6%, whereas in diamines-MATMS it is 5%. The relative percentages

obtained from deconvolution of $^{29}$Si CPMAS spectra of both the samples are given in Table 3.1.

$^{13}$C CP-MAS spectra of post grafted diamine-GPTMS and diamine-MATMS of the deuterated diamine are shown in Figure 3.1. The chemical shifts corresponding to diamine-GPTMS are (a) 71 ppm, (b) 22.7 ppm, (1, 2) 39.6 ppm, (e, f) 51.4 ppm, and (c, d) 73.2 ppm. For diamine-MATMS, the $^{13}$C chemical shifts are (a) 6.91 ppm, (g) 13.56 ppm, (b) 21.3 ppm, (1, 2) 39.5 ppm, (c) 66.2 ppm, (f') 124 ppm, (e') 178 ppm and (d') 186 ppm. Though $^{29}$Si CP-MAS spectra of both samples show the presence of $T_2$ conformation, the $^{13}$C CPMAS spectrum of diamine-GPTMS does not show the presence of ethoxy. This may be due to the lower grafting concentration in diamine-GPTMS and hence reduced intensity of these peaks.

**Table 3.1**: Relative percentages of various resonances extracted using DM FIT from $^{29}$Si CPMAS spectra of SBA-15 modified with diamine-GPTMS and diamine-MATMS.

| $^{29}$Si groups in modified SBA-15 | Diamine-GPTMS (%) | Diamine-MATMS (%) |
|---|---|---|
| $Q_2$ | 11.64 | 4.99 |
| $Q_3$ | 50.93 | 47.04 |
| $Q_4$ | 25.31 | 27.07 |
| $T_2$ | 4.59 | 8.3 |
| $T_3$ | 7.54 | 12.6 |

Ethoxy peaks observed in diamine-MATMS are shown with "*" and correspond to 25.3 and 51 ppm. We have observed a considerable difference in the intensity of deuterated carbons (1, 2) for the two samples, although they are recorded under identical CP conditions. This may be due to more contribution from remote protons and less dynamics of the end group in diamine-MATMS. The reduced intensity of peaks (1, 2) may also arise due to a lower coupling yield of diamine to GPTMS when compared with diamine to MATMS. However we could not clearly identify the epoxy $^{13}$C resonances which would be present for uncoupled GPTMS.

To summarize, $^{29}$Si CPMAS analysis shows that linkers are grafted either in $T_2$ or in $T_3$ configuration, more linkers being grafted in the $T_3$ configuration in both samples. The assignment of $^{13}$C CPMAS spectra shows that ethoxy is absent in diamines-GPTMS.

### 3.2.2 Analysis of Proton Spectrum of Diamine-GPTMS and Diamine-MATMS.

When hydrated, the surface of mesoporous silica materials becomes complex due to the distribution and dynamics of adsorbed water on the pore surface. Proton NMR spectrum would be able to differentiate between water molecules which are hydrogen bonded to the surface and water molecules hydrogen bonded with themselves through chemical shift discrimination. Below, a brief description of the proton spectra and the dominant dynamic components present is given.

The $^{1}$H MAS NMR spectra of the wet and dry state of diamine-GPTMS and diamine-MATMS recorded at 298 K are shown in Figure 3.2 and 3.3 respectively. For diamine-GPTMS, the ratio of total integrated proton intensity of dry and wet samples is 0.58, whereas it is 0.6 for diamine-MATMS. The total integrated intensity of the proton spectra is correlated to the weight loss and the number of protons/nm$^2$ is calculated in both the samples. We have estimated a $p\sim9$ H/nm$^2$ and $p\sim4$ H/nm$^2$for Wet and Dry states of diamine-GPTMS and a $p\sim8$ H/nm$^2$ and $p\sim4$ H/nm$^2$for Wet and Dry states of diamine-MATMS. The spectra were deconvoluted using DMFIT to their respective dominant dynamic components, bulk water or free water with a chemical shift range of 4.4−5.2 ppm, surface water at 2.8−3.3 ppm, which may appear when the surface has a few number of water molecules which form hydrogen bonds with the surface silanols (Si−OH + $H_2O$), and isolated silanols (Si−OH) in the 1.6−1.8 ppm range. When the sample becomes dry, a fewer number of water molecules that are in the pores closer to the surface form hydrogen bonding with Si−O− resulting in the formation of isolated silanols. Resonance arising from isolated silanol is prominently visible in the proton spectra recorded at the dry state of both samples. The $p$ H/nm$^2$ values calculated are consistent with the distribution of water molecules on SBA-15 discussed in Chapter 2, where cluster formation is reported at $x \geq 4$.The variation of the relative integrated intensity of dynamic components with respect to hydration and temperature for diamine-GPTMS and diamines-MATMS is shown in Figure 3.2 and 3.3 respectively. Deconvolution of the proton spectra recorded at 298 K for both samples is shown in the Figure 3.4.

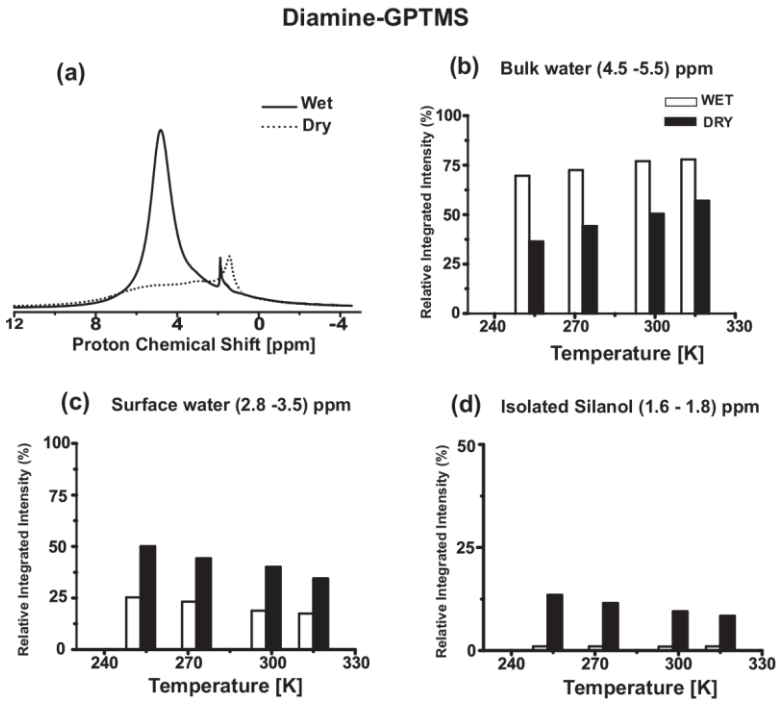


**Figure 3.2** (a) Proton spectra of diamine-GPTMS recorded at 298 K for the wet and dry state. (b−d) Relative percentage of bulk water, surface water, and isolated silanols at 253, 273, 298, and 315 K of diamine-GPTMS. The ratio of the total integrated intensities of dry and wet samples is 0.58 for diamine-GPTMS.

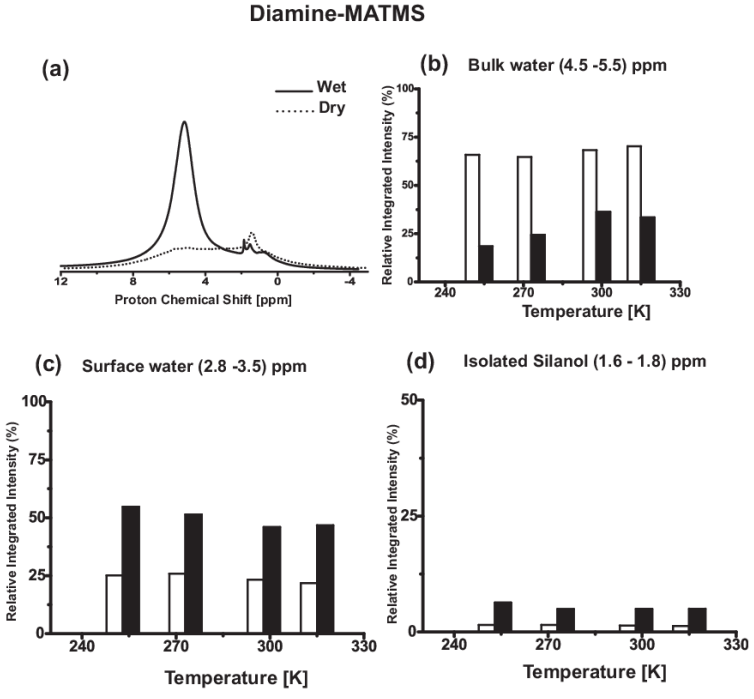


**Figure 3.3** (a) Proton spectra of diamine-MATMS recorded at 298 K for the wet and dry state. (b−d) Relative percentage of bulk water, surface water, and isolated silanols at 253, 273, 298, and 315 K of diamine-MATMS. The ratio of the total integrated intensities of dry and wet samples is 0.6 for diamine-MATMS.

Proton spectra of diamine-GPTMS and diamine-MATMS at low temperatures exhibit broad spectral features arising from homonuclear dipolar coupling of solidified bulk water. Solidified bulk water, present at low temperatures, results in a broad resonance such that the total integrated intensity over the range of interest reduces. The relative amount of surface water and isolated silanols increases at lower temperatures for both samples. At 253 K, both samples show a significant contribution from bulk water, ~35% for diamine-GPTMS and ~15% for diamine-MATMS. Bulk water not solidified at lower temperatures will contribute to the dynamics of grafted molecules. The percentage of isolated silanols in diamine-MATMS is almost half when compared to diamine-GPTMS. This is due to the higher grafting concentration in diamine-MATMS (hence less $Q_2$). In both samples, the amine protons and the dynamic methylene protons are not visible in the proton spectra even at lowest hydration levels, in spite of narrower line-widths expected due to dynamics. We attribute the absence of these peaks to low grafting concentration.

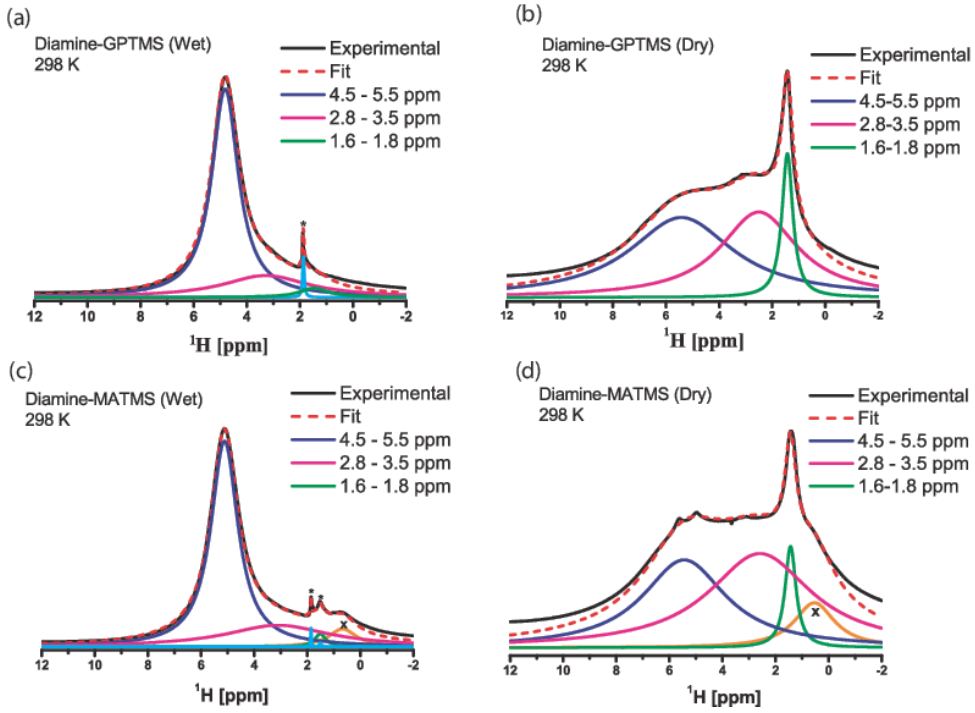


**Figure 3.4** (a,b) Diamine-GPTMS $^1$H MAS spectra recorded at 298 K and their best fit, for the wet and dry states. The spectra correspond to Figure 3.2(a) in the main text. (*) denotes an impurity peak with relative integrated intensity < 1%. Ratio of the total integrated intensities for the dry and wet samples is 0.58. (c,d) Diamine-MATMS $^1$H MAS spectra recorded at 298 K and their best fit, for the wet and dry states. The spectra correspond to Figure 3.3(a) in the main text. (*) denote impurity peaks with relative integrated intensity < 1%. The peak observed at 0.6 ppm and denoted by (x) has a constant relative integrated intensity of 5 % in both wet and dry states and is excluded from the dynamic discussion. Ratio of the total integrated intensities for the dry and wet samples is 0.6.

The above discussion provides an estimate of the relative percentage of bulk water protons, surface protons, and silanols present in the sample which may be able to induce molecular mobility of anchored molecules. The molecular conformations associated with the mobility may also depend on the length of the anchored molecule, presence of double bonds in the molecule, and presence of −OH−, N−H, etc. in the molecule which can interact with Si−OH through hydrogen bonding. The correlation between molecular dynamics initiated by the distribution of water protons on the surface of the mesoporous materials and deuterium MAS NMR spectra is discussed below.

**3.2.3 Analysis of Deuterium Spectra of Diamine-GPTMS and Diamine-MATMS.** Deuterium MAS spectra of wet and dry diamine-GPTMS, recorded at 253 and 315 K along with the best fit spectra, are shown in Figure 3.5. The spectra were deconvoluted using DMFIT to their respective dynamic components. A minimum of three components with different line widths were needed to get the best fit spectra. The errors in the quadrupolar coupling parameters $\{\bar{C}_Q, \bar{\eta}\}$ are calculated based on Monte Carlo error analysis in DMFIT. Spectra recorded at 273 and 298 K along with the best fit are shown in Appendix Figure B3.1. Representative $^2$H MAS NMR spectra along with deconvoluted components, and difference between experimental and best fit spectra, are shown in Figure 3.6.

Close observation reveals that (a) sidebands have relatively sharp linewidths, (b) frequency span is the same irrespective of hydration, and (c) spectra are not arising from a single quadrupolar coupling tensor at any temperature. The presence of relatively sharp spectral components suggests that molecules are undergoing dynamics in the fast motional limit. On the other hand, the absence of broad spectral components suggests that dynamics in the intermediate motional regime is not reflected in the spectra. Since the time domain deuterium data were processed by removing the data points until the first echo, it is reasonable to assume that components arising from slow dynamics and thus having fast transverse relaxation rates will not appear in the analysed spectra. However, one cannot overrule the possibility of slower dynamics with intermediate jump rates. While analysing the spectra, a small redistribution of the intensity of the sidebands has been incorporated wherever necessary to symmetrize the spinning sideband pattern. The quadrupolar coupling parameters $\{\bar{C}_Q, \bar{\eta}\}$ employed to get the best fit spectra are given in Table 3.2. For all spectra, the errors are below $\{\pm 1.5\ \text{kHz}, \pm 0.01\}$ for the rigid component, below $\{\pm 1.5\ \text{kHz}, \pm\ 0.02\}$

for the intermediate component and below $\{\pm 3$ kHz, $\pm 0.05\}$ for the large amplitude dynamic component.

**Table 3.2**. Best-Fit Quadrupolar Parameters for Diamine GPTMS at Various Temperatures

| Temperature (K) | (a) WET $\{\bar{C}_Q(\text{kHz}), \bar{\eta}\}$ | (b) DRY $\{\bar{C}_Q(\text{kHz}), \bar{\eta}\}$ |
|---|---|---|
| 253 | {158, 0. 09}, {85, 0.7} {43, 0.7} | {158, 0. 09}, {88, 0.58} {43, 0.7} |
| 273 | {158, 0. 09}, {83, 0.8} {43, 0.7} | {158, 0. 09}, {88, 0.64} {44, 0.7} |
| 298 | {150, 0.1}, {64, 0.99} {43, 0.7} | {158, 0. 09}, {73, 0.64} {43.3, 0.7} |
| 315 | {150, 0.1}, {62, 0.99} {43, 0.7} | {158, 0. 09}, {74.6, 0.65} {43, 0.7} |

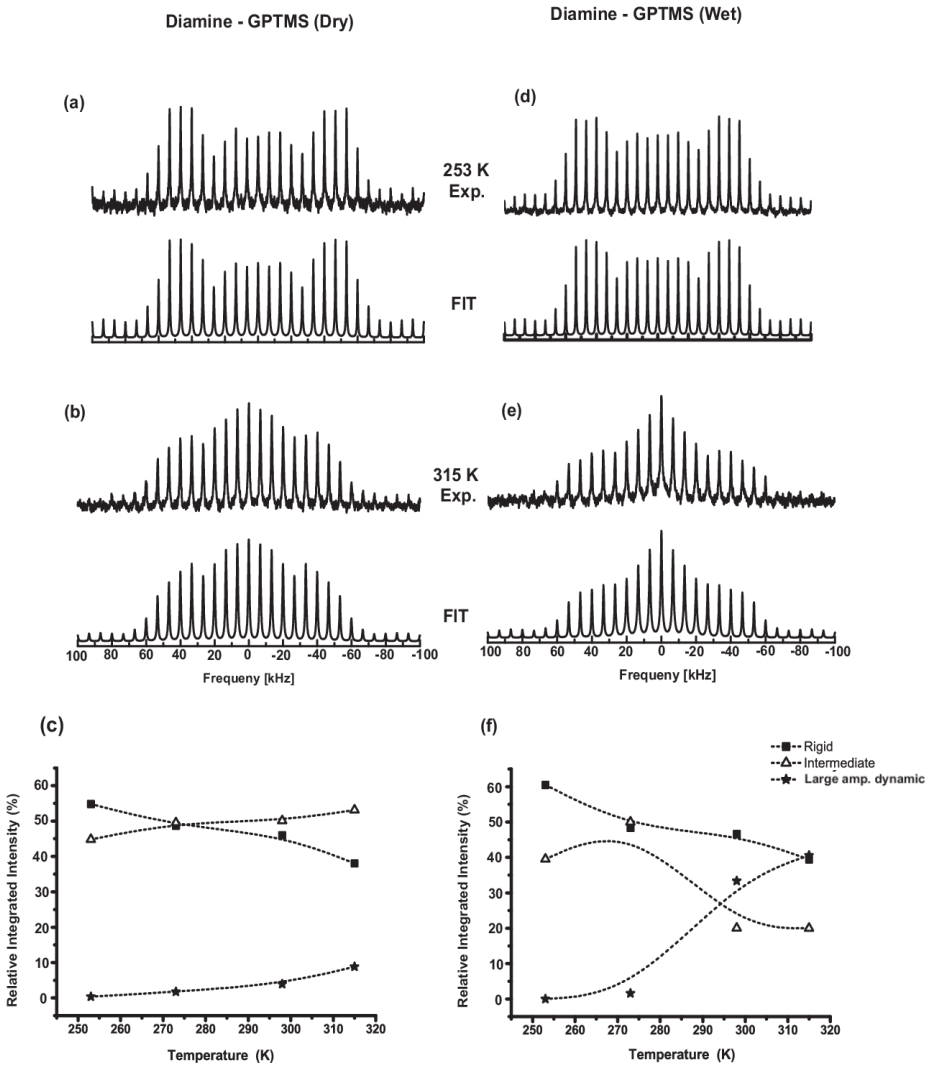


**Figure 3.5** $^2$H MAS NMR spectra of diamine-GPTMS recorded at 6666 Hz MAS, 253 and 315 K, along with the best fit for the dry (a, b) and the wet (d,e) states of the sample. Relative percentages of rigid (■), intermediate (Δ), and large amplitude (*) dynamic quadrupolar components for the dry (c) and the wet (f) states of the sample.

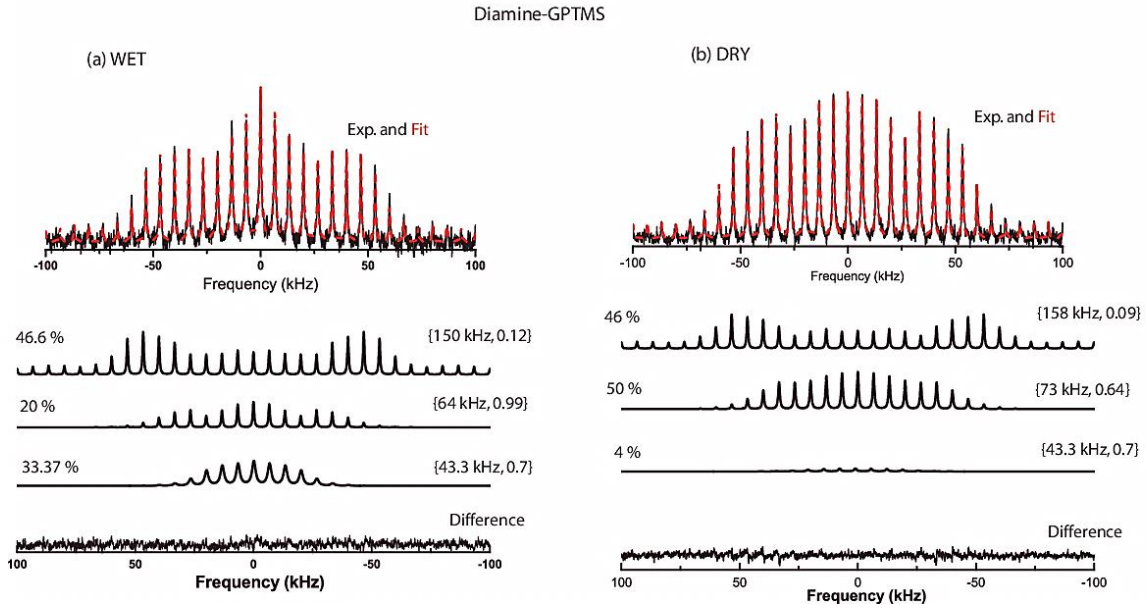


**Figure 3.6** Diamine-GPTMS $^{2}$H MAS NMR spectra recorded at 6666 Hz MAS, and 298 K for the wet and dry state. The relative percentage of integrated intensity and the averaged quadrupolar parameters of the deconvoluted components are shown in the plot.

Based on the averaged quadrupolar coupling values, the spectral components with $\bar{C}_Q = \{158 - 150\ \text{kHz}\}$, $\bar{C}_Q = \{88\ \text{kHz} - 62\ \text{kHz}\}$, and $\bar{C}_Q = \{43\ \text{kHz}\}$ are referred to as rigid component, intermediate amplitude dynamic component, and large amplitude dynamic component respectively. Intermediate amplitude and large amplitude dynamic components may correspond to two different types of molecular mobility resulting in the reduced quadrupolar couplings mentioned above. The relative percentages of all the three spectral components and their variation with respect to temperature and hydration are given in Figure 3.5. The relative percentage of intermediate and large amplitude dynamic components increases with temperature in the dry state, and the relative percentage of large amplitude dynamic component is low at all temperatures. With the wet sample, there is a significant decrease in the percentage of intermediate dynamic component and a significant increase in the large amplitude dynamic component in the 270−310 K interval. Variation with temperature of the relative percentages of the rigid component and the sum of intermediate and large amplitude dynamic components is shown in Appendix Figure B3.2.

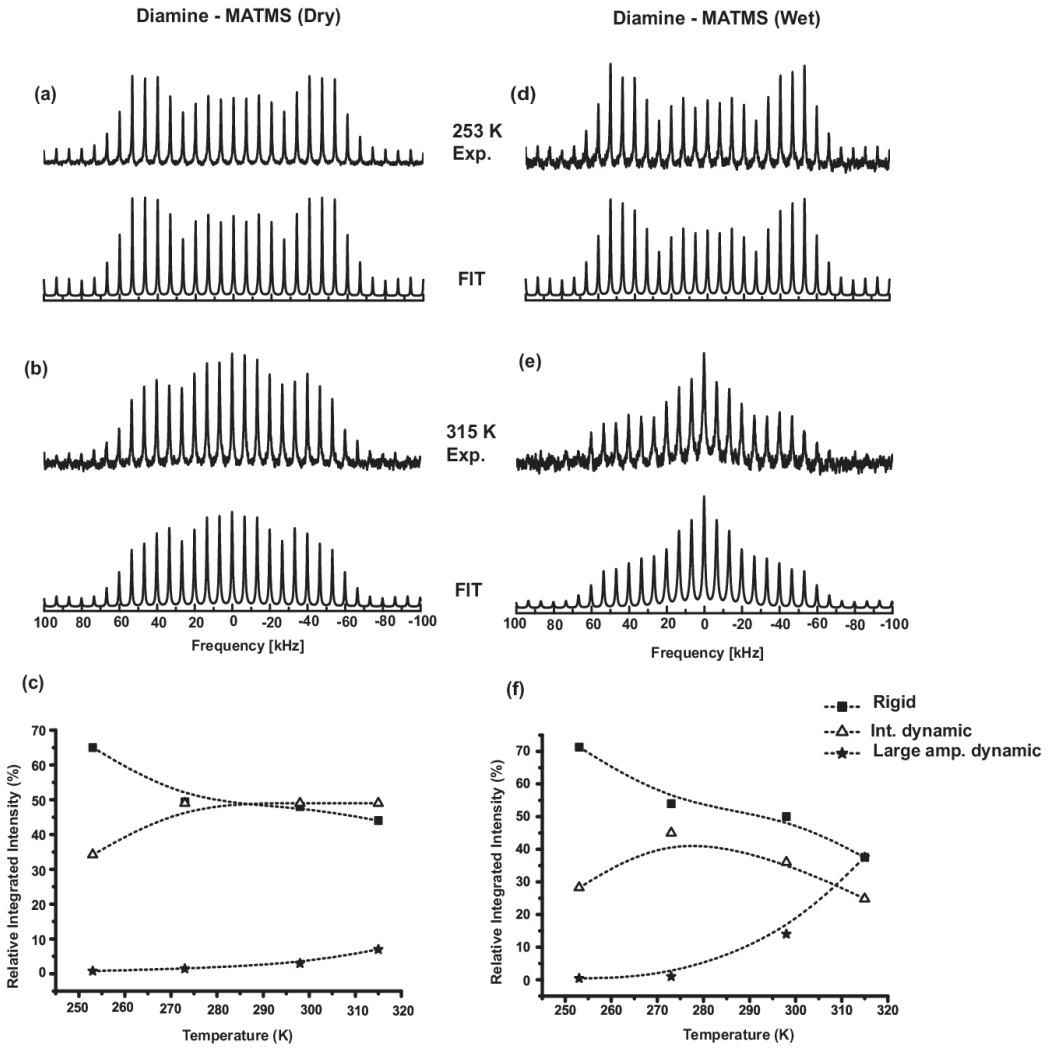


**Figre 3.7** $^{2}$H MAS NMR spectra of diamine-MATMS recorded at 6666 Hz MAS, 253 and 315 K, along with the best fit for the dry (a, b) and the wet (d,e) states of the sample. Relative percentages of rigid (■), intermediate (Δ), and large amplitude (*) dynamic quadrupolar components for the dry (c) and the wet (f) states of the sample.

Deuterium MAS spectra of wet and dry diamine-MATMS, recorded at 253 and 315 K, along with the best fit spectra are shown in Figure 3.7. Spectra recorded at 273 and 298 K along with the best fit are shown in Appendix Figure B3.3. Representative $^{2}$H MAS NMR spectra along with deconvoluted components and difference between experimental and best fit spectra are shown in Appendix Figure B3.4. The best fit values of the quadrupolar parameters are given in Table 3.3. For all spectra, the errors are below $\{\pm 1\ \text{kHz}, \pm 0.01\}$ for the rigid component, below $\{\pm 1\ \text{kHz}, \pm 0.02\}$ for the intermediate component and below $\{\pm 2\ \text{kHz}, \pm 0.03\}$ for the large amplitude dynamic component. As before, a small

redistribution of the intensity of the sidebands has been incorporated wherever necessary to symmetrize the spinning sideband pattern. The quadrupolar parameters corresponding to rigid, intermediate dynamic, and large amplitude dynamic components are $\{158-155\ \text{kHz}, 0.09\}$, $\{92\ \text{kHz}-72\ \text{kHz}, 0.7-0.6\}$, and $\{43\ \text{kHz}, 0.7\}$ respectively.

**Table 3.3**. Best-Fit Quadrupolar Parameters for Diamine-MATMS at Various Temperatures

| Temperature (K) | (a) WET $\{\bar{C}_Q(\text{kHz}), \bar{\eta}\}$ | (b) DRY $\{\bar{C}_Q(\text{kHz}), \bar{\eta}\}$ |
|---|---|---|
| 253 | {158, 0.09}, {92, 0.77}<br>{43.3, 0.7} | {158, 0.09}, {88, 0.7}<br>{43.3, 0.7} |
| 273 | {158, 0. 09}, {83, 0.78}<br>{43.3, 0.7} | {158, 0.09}, {86, 0.6}<br>{43.3, 0.7} |
| 298 | {155, 0.09}, {72, 0.7}<br>{43.3, 0.9} | {158, 0.09}, {78, 0.59}<br>{43.3, 0.7} |
| 315 | {155, 0. 09}, {64, 0.97}<br>{43.3, 0.7} | {158, 0.09}, {73.6, 0.63}<br>{43.3, 0.7} |

Variation with temperature of the relative percentages of the rigid component and of the sum of intermediate and large amplitude dynamic components is shown in Appendix Figure B3.5. The variation of relative percentages for all the three spectral components is shown in Figure 3.7. Similar to diamine-GPTMS, the relative integrated intensity of intermediate and large amplitude dynamic components increases with temperature in the dry state, and the percentage of large amplitude dynamic component is low at all temperatures. For the wet sample, there is a gradual decrease in the percentage of intermediate dynamic component and a significant increase in the large amplitude dynamic component in the 270−315 K interval. The large amplitude dynamic component may be due to the additional rotational degree of freedom about $C_1 - C_2$ bond axis of the ($D_3$, $D_4$) deuterons when compared with ($D_1$, $D_2$). This is revisited in section 3.3.2.

For both linkers, $^2$H MAS NMR spectral analysis provided similar results. Deuterium spectral line widths for diamines-GPTMS and diamine-MATMS are comparable even though the grafting concentrations are different. The change in molecular conformation due to dynamics, leading to the averaged quadrupolar parameters, can be compared across the linkers, as the change in mobility is largely due to the presence or absence of water molecules in the vicinity of the grafted molecule. Additional dynamics can arise from the steric hindrance or segmental mobility due to a difference in the length of the linkers.

### 3.2.4 Molecular Level Picture from Deuterium Solid state NMR.

In this section, the correlation between dynamics of the grafted molecules and the averaged quadrupolar parameters is addressed.

Quadrupolar parameters reported for deuterated rigid molecules having C–$^2$H are $\{C_Q, \eta\} = \{180 - 160\ \text{kHz}, 0.0\}$ [11,117-119,167-172]. However, we could not fit any of the $^2$H MAS NMR spectra recorded from diamine-GPTMS and diamines-MATMS with zero anisotropy of the rigid component. The small anisotropy of the rigid component obtained from the best fit spectra can thus be attributed to a small angle jump. This could be due to local motion of the end groups, −NH-$CD_2$-$CD_2$-$NH_2$ in diamine-GPTMS and =N-$CD_2$-$CD_2$-$NH_2$ in diamine-MATMS, with respect to the organic linker grafted. Additional changes in mobility affecting average quadrupolar parameters can also arise due to the presence of −C=N− in diamines-MATMS.

The orientation dependent NMR quadrupolar frequency is given in Eq. [1.44a,b; 1.47]. As discussed in section 1.3.1, dynamic studies often involve comparison of rigid-limit quadrupolar coupling parameters $\{C_Q, \eta\}$ with the dynamic average $\{\bar{C}_Q, \bar{\eta}\}$. When the molecules undergo a dynamic process, the angles $\{\theta, \phi\}$ which denotes the orientation of the magnetic field in the quadrupolar PAS changes with time, resulting in an averaged quadrupolar interaction characterized by averaged quadrupolar parameters $\{\bar{C}_Q, \bar{\eta}\}$. It is important to note that even if $\eta = 0$, the motionally averaged asymmetry parameter may not vanish [122]. The dynamic averaged quadrupolar parameters result in changes of the NMR quadrupolar frequency and of the $^2$H spinning sideband pattern. Therefore, analysis of $^2$H spinning sideband patterns can provide information about molecular motion.

For reorientation by small angles, the frequency changes very slightly with respect to the rigid limit. If the mobility is rapid on the time scale of $C_Q^{-1}$, the spread of angles $\{\theta, \phi\}$ over which C−$^2$H bond vector can fluctuate and can be estimated [122] by solving $\frac{\{3cos^2\theta - 1 + \bar{\eta} sin^2\theta \cos(2\phi)\}}{2} = {C_Q}/{\bar{C}_Q}$, where $C_Q$ is the isotropic rigid component. For small angle librations,

$$C_Q = (1 + \bar{\eta})\bar{C}_Q \qquad 3.1$$

and

$$\bar{C}_Q/C_Q = P_2(cos\theta_o), \quad 3.2$$

where $\theta_o$ is half the jump angle between *two* orientations. For small displacements, only one solution of $\theta_o$ is valid for a given $\{\bar{C}_Q, \bar{\eta}\}$. In both the samples, we believe that $C-^2H$ is undergoing *small angle* reorientations resulting in $\{\bar{C}_Q, \bar{\eta}\}$ in the range $\{158 - 150\ \text{kHz}, 0.12 - 0.09\}$. Line-shape analysis of the experimental spectrum provided an asymmetry parameter ~ 0.1 for all rigid components. Assuming the above model is valid in this study, we have estimated approximately the quadrupolar parameters of rigid component as $\{\sim 172\ \text{kHz}, 0.0\}$ by utilizing the experimentally observed $\{\bar{C}_Q, \bar{\eta}\}$ at 298 K from the dry state of both samples. The corresponding $\theta_o$ calculated with Eq. [3.2] is ~ 13°. The experimentally observed $\{\bar{C}_Q, \bar{\eta}\}$ values corresponding to the rigid component are thus a consequence of *small angle* libration of the $C-^2H$ bond vectors. The $C_Q$ values calculated above are further used in the molecular dynamic simulations while deriving dynamic average quadrupolar parameters.

**Table 3.4** Ratio between Populations of the Rigid Component and the Sum of Intermediate and Large Amplitude Dynamic Components.

| Temperature (K) | diamine-GPTMS ($P_{Rigid}/P_{Int.+large}$) | | diamine-MATMS ($P_{Rigid}/P_{Int.+large}$) | |
|---|---|---|---|---|
| | Dry | Wet | Dry | Wet |
| 253 | 1.21 | 1.53 | 1.86 | 2.48 |
| 273 | 0.95 | 0.94 | 0.98 | 1.17 |
| 298 | 0.85 | 0.87 | 0.92 | 1 |
| 315 | 0.61 | 0.65 | 0.79 | 0.6 |

The ratio between populations of the rigid component and the sum of intermediate and large amplitude dynamic components, $P_{Rigid}/P_{Int.+large}$, are given in Table 3.4 for both samples. For diamine-MATMS, $P_{Rigid}/P_{Int.+large} \geq 1$ for wet sample between temperatures 253-298 K. This may arise due to presence of more silanols interacting with the molecule and thus resulting in less mobility. For diamine-GPTMS, $P_{Rigid}/P_{Int.+large}$ are comparable among wet and dry samples between 273 - 315 K. It can be concluded that diamine-GPTMS is more dynamic when compared with diamine-MATMS. This may be attributed to the smaller length of diamine-MATMS and/or to more restricted motion due to the –C=N- double bond in diamine-MATMS when compared with diamine-GPTMS. In both samples $P_{Rigid}/P_{Int.+large}$

reduces with increase in temperatures. Since the associated motion is complex, and the number of data points limited, we did not employ the ratios to calculate the Arrhenius energy.

To summarize, $^{2}$H MAS NMR spectra recorded at different temperatures for wet and dry samples are deconvoluted into three spectral components. For both samples, the average quadrupolar parameters are similar, suggesting that the mechanism inducing dynamics in both samples is also similar. From the presence of ~50% relative integrated intensity of a component with large average quadrupolar coupling and small asymmetry parameter, it can be inferred that a significant fraction of the linkers is undergoing *small angle* libration. The other two spectral components, corresponding to medium and small averaged quadrupolar coupling, can be attributed to different molecular mobilities. This observation is later substantiated by molecular dynamic simulations. The sum of the dynamic components increases with temperature and hydration, whereas the rigid component reduces with temperature, but its relative percentage remains more or less in the same range at different hydration levels in both samples. A higher population ratio between the rigid and the sum of total dynamic components in diamine-MATMS indicates more restricted dynamics of the linker.

### 3.2.5 Water Induced Dynamics: A Correlation between Proton and Deuterium NMR Analysis.

Information about the role of hydration on the dynamics of linkers can be obtained by combining the analysis of proton and deuterium MAS NMR spectra. Water distributes over the surface of SBA-15 providing three distinct chemical shift regions corresponding to bulk water, surface water, and isolated silanols. In the present study, it can be seen from the proton and deuterium spectral analysis in both samples that, with an increase in the relative percentage of bulk water from the dry to wet state, the large amplitude dynamic component increases substantially, especially at 298 and 315 K. The analysis also shows an increase of the relative percentage of bulk water as well as an increase in the large amplitude dynamic component with temperature. This suggests that large amplitude dynamics is induced by bulk water in the vicinity of the linker. Following previous studies, we assume that a minimum of one water molecule adsorbed on the surface and ending in the formation of two vicinal silanols may be able to initiate dynamics of the linkers, resulting in the intermediate dynamic component. From Figure 3.2 and 3.3, it is observed that the percentage of surface water and isolated silanols is more in the dry state of both samples. Similarly, we also observe more

percentage of the intermediate dynamic component in the dry state of both samples. This supports the assumption that intermediate dynamics is induced by surface water and isolated silanols.

Molecular conformational changes of the grafted molecule resulting in averaged quadrupolar parameters are investigated below using molecular dynamic simulations.

## 3.3. Molecular Dynamic Simulations.

We have performed MD simulations on models of both samples. As averaged quadrupolar parameters are due to motional changes in the orientation of the quadrupolar PAS frame, the time evolution of all the C–$^2$H unit vectors, $[\boldsymbol{d}_i(t), i = 1-4]$, pointing along the respective C–$^2$H bond directions of the two methylene groups is traced. From the MD output, the trajectories of four $\boldsymbol{d}_i(t)$ are extracted, mapped on a unit sphere, and the time averaged quadrupolar parameters $\{\bar{C}_q, \bar{\eta}\}$are calculated [127,136]. Details of MD simulations and the analysis of the trajectories extracted from dynamic simulations are provided in chapter 1. A brief overview is given below.

### 3.3.1 MD Simulations of Diamine-GPTMS.

The linker diamine-GPTMS as shown in *Scheme 1* is made in 3D atomistic and energy minimized. A template with a pore diameter of ~40 Å is energy minimized, and the molecule is covalently bonded in the $T_3$ configuration. For $T_3$, there will be one Si−OH near the silicon atom to which the linker is bonded. In another template, the molecule has been covalently bonded in $T_2$ configuration and to the third oxygen, hydrogen is bonded to form a hydroxyl, instead of ethoxy in agreement with the $^{13}$C/$^{29}$Si CPMAS spectra. The templates with various possibilities of anchored hydroxyls, and with the molecule bonded in $T_2$ or $T_3$ configuration, are energy minimalized and equilibrated for $1-2\,ns$. Free water molecules were not included in the MD model. The conformation at the end of the run is taken as an xsd file and is further subjected to FORCITE dynamic simulation for $1-2\,ns$ using a COMPASS force field. Each 1000th molecular configuration, after 1 ps, is saved as a trajectory file. The trajectories of C–$^2$H unit vectors, $\boldsymbol{d}_i(t)$, are extracted and analysed using an already existing homewritten Perl and Matlab codes by choosing a reference coordinate system $\{X^F, Y^F, Z^F\}$ as explained at the end of section 1.3.2. The corresponding $\boldsymbol{d}_i(t)$, values i = 1−4, are plotted on the surface of a sphere. The calculated $\{\bar{C}_Q, \bar{\eta}\}$ values are provided in Table 3.5. All simulations were performed at 298 K. Deuterons $D_1$ and $D_2$ are bound to undergo the same

reorientation dynamics, likewise deuterons $D_3$ and $D_4$. The coarseness of the dynamic time steps employed in the simulations are reflected in the deviation of the quadrupolar couplings calculated from the MD output for deuterons $D_1$ and $D_2$ (and deuterons $D_3$ and $D_4$). On the other hand, it has to be noted that the differences in the average quadrupolar coupling calculated between deuterons $D_1$ and $D_2$ (and deuterons $D_3$ and $D_4$) are very small. The fact that these small differences are very small suggests that the output from the dynamic studies through MD approach is sufficiently accurate and reliable.

Silanols are positioned at various distances accessible to the linkers from the anchoring silicon atom and the corresponding $\{\bar{C}_Q, \bar{\eta}\}$ values calculated are given in Table 3.5.

**Table 3.5**. Diamine-GPTMS: Averaged Quadrupolar Parameters $\{\bar{C}_Q, \bar{\eta}\}$ Calculated from Molecular Dynamic Simulations. $\{C_1, i = 1, 2\}$ corresponds to $C_1 - D_1$ and $C_1 - D_2$ whereas $\{C_2, i = 3, 4\}$ corresponds to $C_2 - D_3$ and $C_2 - D_4$ respectively. (refer to Figure 3.1).

| no. | grafting configuration | no. of Protons anchored | $r_{Si-OH}$ ( Å) | $(C_1, i = 1, 2)$ $\{\bar{C}_Q(\text{kHz}), \bar{\eta}\}$ | $(C_2, i = 3, 4)$ $\{\bar{C}_Q(\text{kHz}), \bar{\eta}\}$ |
|---|---|---|---|---|---|
| 1 | $T_3$ | 3 | 3.631, 12.208, 12.292 | {75.4, 0.84}, {73.4, 0.84} | {74.7, 0.85}, {74.7, 0.9} |
| 2 | $T_2$ | 3 | 4.396, 4.337, 4.665 | {72, 0.8}, {75, 0.8} | {73, 0.76}, {75, 0.84} |
| 3 | $T_2$ | 4 | 3.737, 2.673, 4.308, 5.924 | {65.7, 0.78}, {66.4 , 0.87} | {65.08, 0.84}, {62.7, 0.6} |
| 4 | $T_3$ | 3 | 4.468, 4.713, 5.043 | {60.5, 0.75}, {60.5, 0.74} | {60.5, 0.8}, {60.5, 0.79} |
| 5 | $T_3$ | 3 | 3.846, 14.577, 12.215 | {46, 0.9}, {44.5, 0.7} | {44, 0.8}, {48, 0.7} |
| 6 | $T_3$ | 4 | 3.846, 12.215, 12.258, 14.016 | {41.3, 0.6}, {46, 0.6} | {41.3, 0.9}, {46.4, 0.9} |

The time dependence of dihedral angles for diamine-GPTMS anchored in $T_3$ configuration, with hydroxyls at a distance of 3.631, 12.208, and 12.292 Å with respect to the anchored silicon, is shown in Figure 3.8. For $T_2$ configuration, the time dependence of dihedral angles with hydroxyls situated at 4.396, 4.337, and 4.665 Å is also shown in Figure 3.8. The reduced quadrupolar parameters corresponding are shown in Table 3.5, model 1 and 2. For $T_3$ configuration, the variation in dihedral angles is between 180° to 60°, 180° to −60°, 180° to −120°, etc. The changes in dihedral angles may also reflect transitions between *"trans"* and *"gauche*" molecular conformation along with other staggered/ bent conformations. In the case of $T_2$, the dihedral angle changes from 180° to −60° and from 180°

to −120° for $C_dC_eC_fN$ and $C_fNC_1C_2$ respectively. $\boldsymbol{d}_i(t)$ for i = 1 and 3 are shown for $T_3$ and $T_2$ in Figure 3.9 along with the respective averaged quadrupolar parameters. For $T_2$, the trajectory (i = 1 and 3) spans three distinct regions, whereas for $T_3$ the trajectories are distributed over a broad region. Molecular conformations extracted for $T_3$ at 0.6, 0.9, and 1.3 ns and for $T_2$ at 0.3, 0.6, and 0.9 ns are shown nearby. It can be seen, for both $T_2$ and $T_3$ molecular conformations, that the molecule is stabilized with the surface through −OH---HO-Si− and/or $-NH_2$---HO-Si− hydrogen bonding. This results in restricted mobility of the linker and local mobility of the end group, as also seen from the time dependence of dihedral angles.

With respect to position of the hydroxyls in the neighbourhood of the linker, the dynamics of the linkers may differ; yet, we see that averaged quadrupolar parameters are very similar. Results of a few more molecular dynamic simulations with hydroxyls at different positions are shown in Table 3.5. Figure 3.10 displays yet another possibility for a $T_2$ configuration with hydroxyls at a distance of 3.737, 2.673, 4.308, and 5.924 Å from the anchoring silicon corresponding to model 3 in Table 3.5. Trajectory spans two distinct regions, and the transition between the two resulted in averaged quadrupolar coupling in the range of $\{62 - 66$ kHz$\}$. The molecular conformation extracted at 0.9 and 1.2 ns from the dynamic run is also shown. As before, it can be seen that the linker gets stabilized to the surface through −(H)C−OH---HOSi, −NH---HO-Si, and $-NH_2$---HO-Si hydrogen bonding.

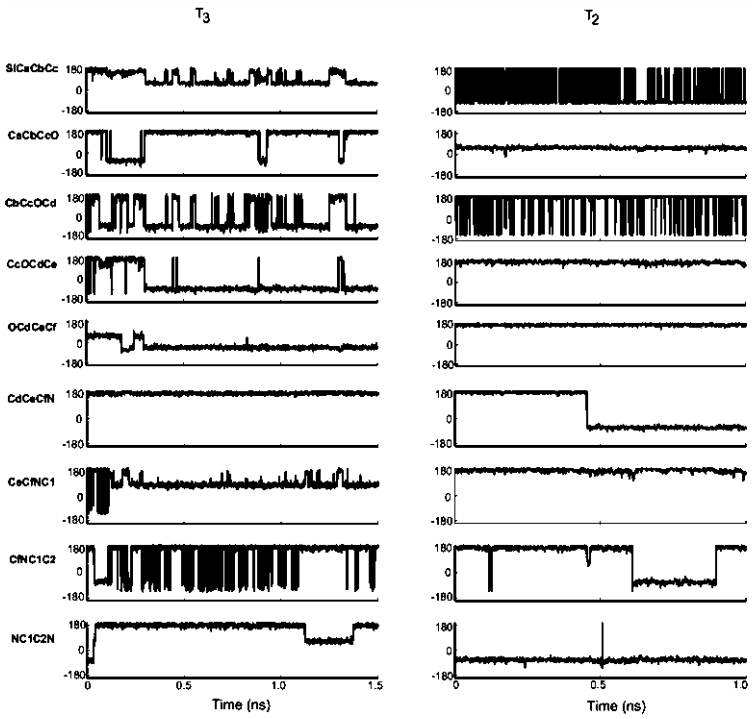


**Figure 3.8** Time dependence of dihedral angles along the length of the linker, extracted from MD simulations, for diamine-GPTMS anchored in $T_3$ and $T_2$ configurations, and the model (1, 2) in Table 3.5.

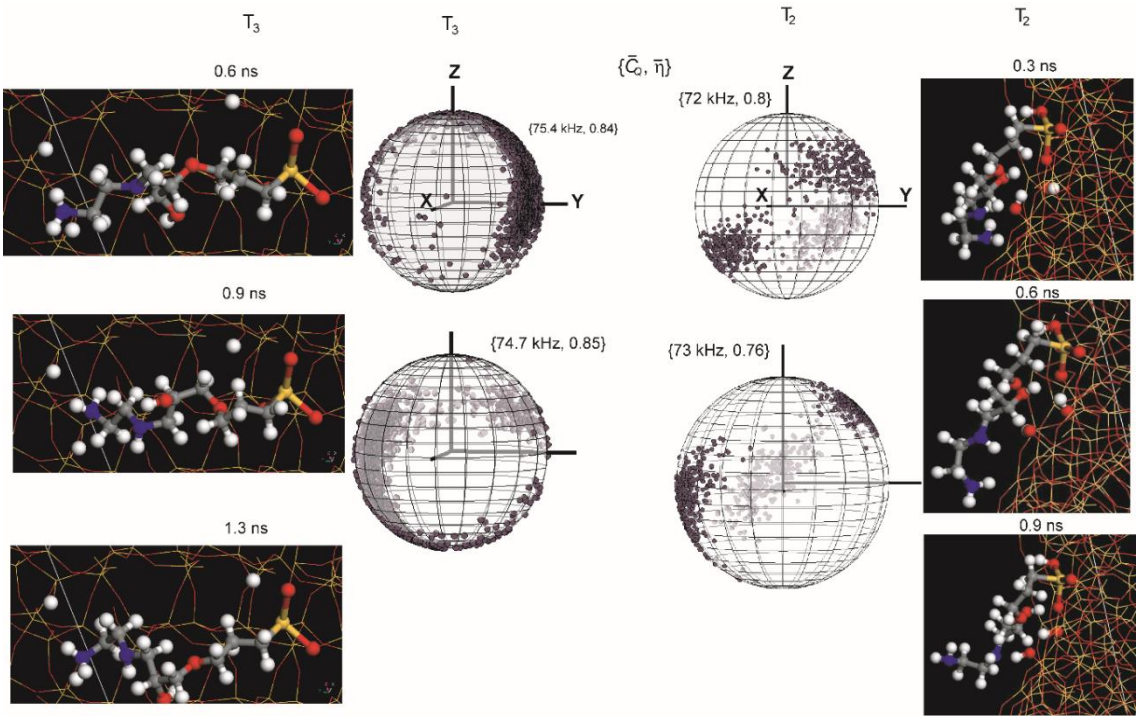


**Figure 3.9** Spatial variation of C-$^2$H vectors ($\boldsymbol{di}(t)$), corresponding to the model of Figure 3.8, drawn on a unit sphere. Out of four C-$^2$H vectors only, $\boldsymbol{d}_1(t)$ and $\boldsymbol{d}_4(t)$ are shown. The average quadrupolar coupling parameters derived from MD are shown near the spheres. Molecular conformations extracted from MD simulation are shown nearby. Yellow (Si), red (O), gray (C), blue (N), and white (H) are the colour codes for the respective atoms.

The $\{\bar{C}_Q, \bar{\eta}\}$ values derived from MD analysis of molecular models belonging to Nos. 1-4 correspond to the values for the intermediate dynamic component obtained from the deuterium MAS NMR spectra, whereas the values for models 5 and 6 correspond to the large amplitude dynamic component as shown in Table 3.2 for wet and dry samples, at 298 K. It can be seen from the spatial variation of the trajectory vectors shown in Figure 3.9 that, in the case of model-1 ($T_3$) most of the trajectory vectors are confined within a rather narrow strip on the unit sphere, whereas for model-2 ($T_2$) the trajectories are within three well-defined regions, resembling a "three site" jump motion. For model (3), shown in Figure 3.10, it can be seen that dynamics is confined in two well-defined regions, resembling a "two site" jump motion. The time dependence of the dihedral angle, and the molecular conformations corresponding to model (4) in Table 3.5, are shown in Appendix Figure B3.6. Also in this case the dynamics resembles a "two site" jump motion. The spatial distribution of trajectory vectors for model 5 (Figure 3. 11) shows dynamics over a wider range of angles and results in a reduction of the averaged quadrupolar coupling to values in the range found from the deuterium MAS NMR analysis for the large amplitude dynamic component.

In contrast to models (1-4), which show trajectory vectors spread over two or three well defined regions, the trajectory vectors for model (5, 6) spread over a single large region. For models (2-4) most of the time the trajectory vectors execute rapid jumps within one region followed by abrupt transitions of a larger jump angle to another region. The same holds for models (5-6) except that the rapid small angle jumps and the larger angle jumps bring the trajectory within a single extended region on the unit sphere. For all models, the average jump angle corresponding to the rapid motion is about 15°, and the average jump angle for large jumps is about 60°. The different geometrical arrangements of the hydroxyls considered in the simulations are just a few from the total number of possible arrangements. However, it is unlikely that qualitative differences would occur when considering additional geometrical arrangements of the hydroxyls.

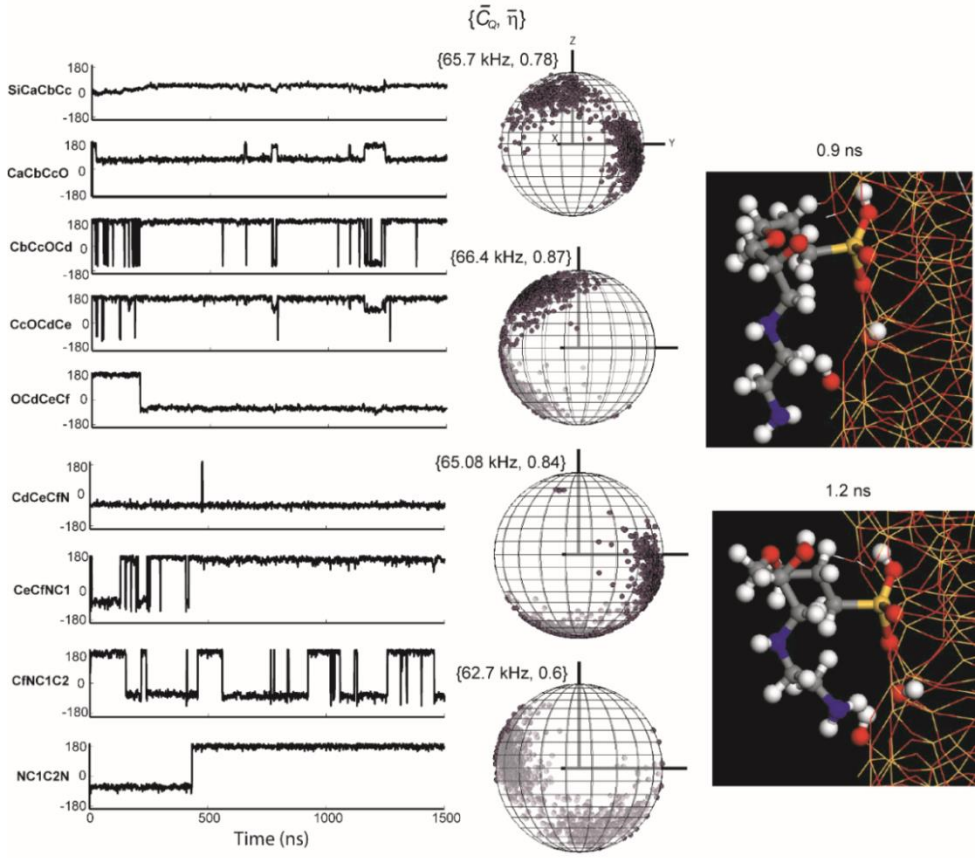


**Figure 3.10** Time dependence of dihedral angles, spatial variation of vectors C-$^2$H ($\boldsymbol{d}_i(t)$), and molecular conformations derived from MD for $T_2$ configuration of diamine-GPTMS corresponding to model (3) in Table 3.5. The average quadrupolar parameters are shown nearby. Yellow (Si), red (O), gray (C), blue (N), and white (H) are the colour codes for the respective atoms.

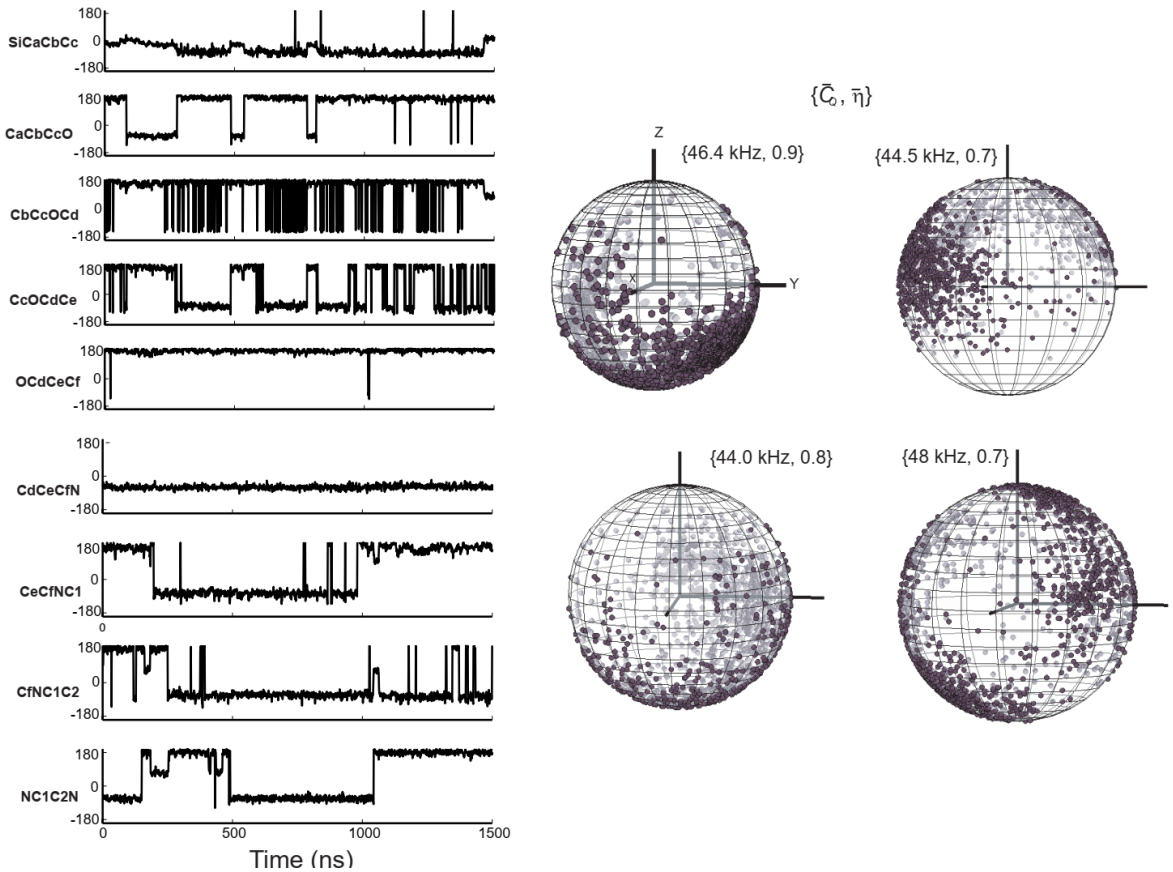


**Figure 3.11** MD calculations for diamine-GPTMS in $T_3$ configuration and three hydroxyls positioned at 3.846, 14.577, and 12.215 Å from the anchoring silicon atom (model (5) in Table 3.5 (main text)). Time dependence of dihedral angles (left), spatial variation of C-$^2$H vectors (right), and the average quadrupolar coupling parameters derived from MD are shown. Yellow (Si), red (O), gray (C), blue (N), and white (H) are the colour codes for the respective atoms.

### 3.3.2. MD Simulations in Diamine-MATMS.

Diamine-MATMS, either in $T_2$ configuration with ethoxy bonded to the third oxygen or in $T_3$ configuration, is covalently bonded in separate templates, and FORCITE dynamic simulations are performed as described above at room temperature. Averaged quadrupolar parameters are shown in Table 3.6. The major difference we derived from the MD studies is the restriction in mobility imparted by the double bond =N-$C_1(D_2)$ when compared with the end group -$(D_2)C_2$-N($H_2$). The difference in mobility is reflected in the averaged quadrupolar parameters shown in models 1, 2, and 5 in Table 3.6.

The time dependence of dihedral angles shown in Figure 3.12, arising from $T_2$, with hydroxyls placed at 3.403, 2.889, 4.381, and 6.656 Å, displays a more constrained dynamics when compared with $T_3$ where the hydroxyls are positioned at 3.435, 3.313, and 3.409 Å. The above configurations correspond to models (4) and (6) given in Table 3.6. It can be seen that

dynamics of $C_aC_bC_cO$ and $C_bC_cOC_{d'}$ in $T_3$ and $NC_1C_2N$ in $T_3$ and $T_2$ arises from a transition between various molecular conformations. In the case of $T_3$, it is evident from the molecular conformations extracted at 0.25, 0.65, and 1.35 ns shown in Figure 3.13 that the linker is stabilized with the surface through $(H_2)$CO---HO-Si and $NH_2$---HO-Si hydrogen bonding. The intermediate molecular conformation associated with $T_2$ at time periods 0.15, 0.55, and 1.42 ns displays similar hydrogen bonding as above. In both cases, the molecule is partially stabilized with the surface through -CO---HO-Si- hydrogen bonding, yet the end group undergoes dynamics. The trajectories $\boldsymbol{d}_i(t)$, for i = 1 and 3, and the averaged quadrupolar parameters arising from $T_3$ and $T_2$ are shown in Figure 3.13.

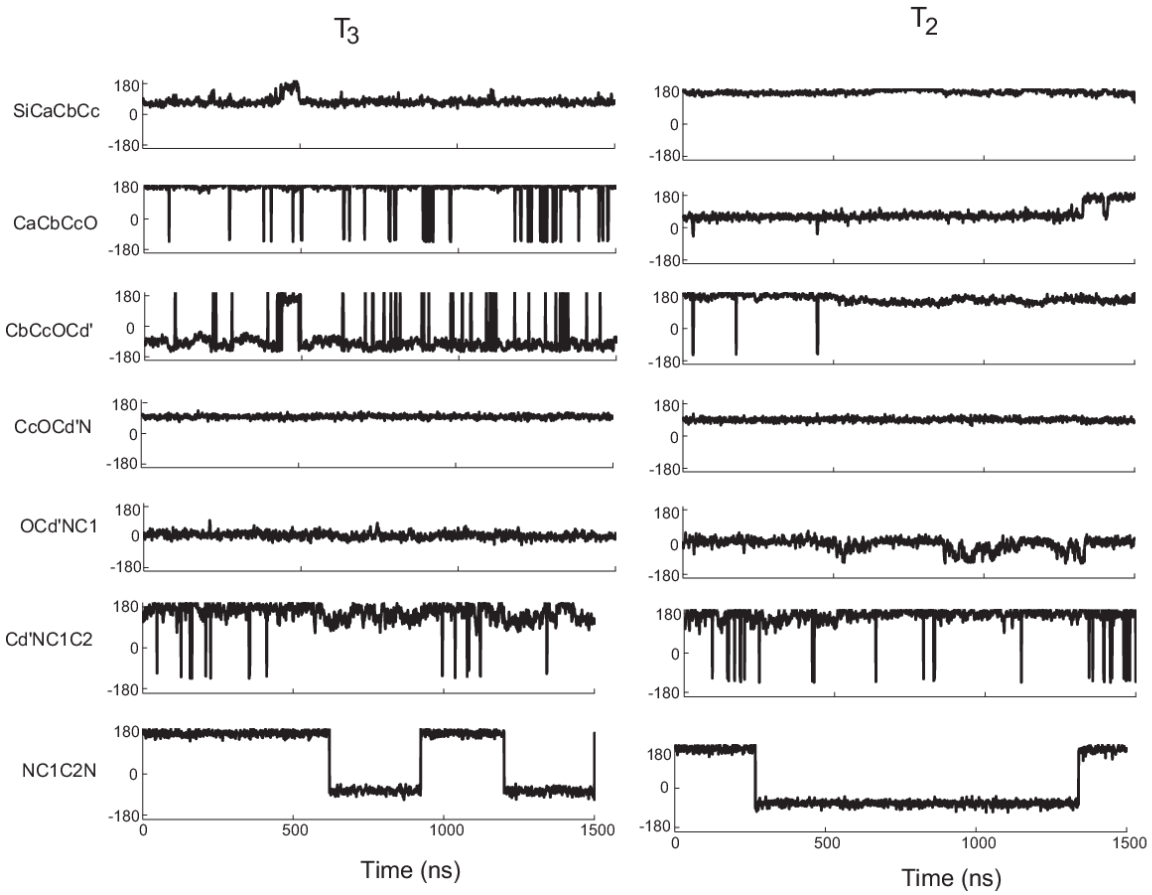


**Figure 3.12** Time dependence of dihedral angles along the length of the linker, extracted from MD simulations, for diamine-MATMS anchored in $T_3$ and $T_2$ configurations, and the model (4, 6) given in Table 3.6.

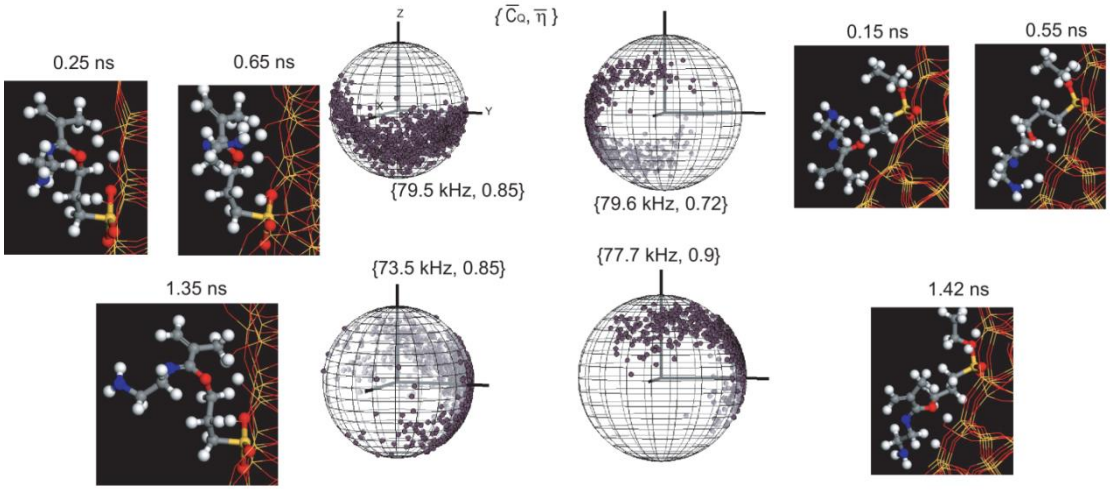


**Figure 3.13** Spatial variation of C-$^2$H$_2$ vectors ($\boldsymbol{d}_i(t)$), corresponding to the model of Figure 3.12, drawn on a unit sphere. Out of four C-$^2$H vectors only $\boldsymbol{d}_1(t)$ and $\boldsymbol{d}_4(t)$ are shown. The average quadrupolar coupling parameters derived from MD are shown near the spheres. Molecular conformations extracted from MD simulation are shown nearby. Yellow (Si), red (O), gray (C), blue (N), and white (H) are the colour codes for the respective atoms.

**Table 3.6**. Diamine-MATMS: Averaged Quadrupolar Parameters $\{\bar{C}_Q, \bar{\eta}\}$ Calculated from Molecular Dynamic Simulations. $\{C_1, i = 1, 2\}$ corresponds to $C_1 - D_1$ and $C_1 - D_2$ whereas $\{C_2, i = 3, 4\}$ corresponds to $C_2 - D_3$ and $C_2 - D_4$ respectively. (refer to Figure 3.1).

| no. | grafting configuration | no. of Protons anchored | $r_{Si-OH}$ ( Å) | $(C_1, i = 1, 2)$ $\{\bar{C}_Q(\text{kHz}), \bar{\eta}\}$ | $(C_2, i = 3, 4)$ $\{\bar{C}_Q(\text{kHz}), \bar{\eta}\}$ |
|---|---|---|---|---|---|
| 1 | $T_3$ | 1 | 3.776 | $\{75, 0.8\}$, $\{80, 0.8\}$ | $\{43, 0.56\}$, $\{46, 0.72\}$ |
| 2 | $T_3$ | 2 | 4.763, 6.467. | $\{77, 0.5\}$, $\{79, 0.76\}$ | $\{44, 0.89\}$, $\{44, 0.78\}$ |
| 3 | $T_2$ | 4 | 3.022, 3.811, 3.511, 4.673. | $\{82, 0.75\}$, $\{80, 0.69\}$ | $\{76, 0.65\}$, $\{74\ 0.9\}$ |
| 4 | $T_2$ | 4 | 3.403, 2.889, 4.381,6.656. | $\{75, 0.62\}$, $\{79.6, 0.72\}$ | $\{77.7, 0.9\}$, $\{73, 0.65\}$ |
| 5 | $T_2$ | 4 | 2.771, 3.509, 3.911, 3.751. | $\{77.5, 0.7\}$, $\{80, 0.8\}$ | $\{43, 0.7\}$, $\{48, 0.9\}$ |
| 6 | $T_3$ | 3 | 3.435, 3.313, 3.409. | $\{80, 0.79\}$, $\{79, 0.85\}$ | $\{73.5, 0.85\}$, $\{73, 0.54\}$ |
| 7 | $T_3$ | 4 | 4.358,4.598, 6.744, 8.649. | $\{155, 0.09\}$ $\{156, 0.07\}$ | $\{153, 0.06\}$ $\{154, 0.08\}$ |

Appendix Figure B3.7 shows results from $T_2$ configuration with four hydroxyls at a distance of 3.022, 3.811, 3.511, and 4.673 Å from the anchoring silicon corresponding to model 3 in Table 3.6. In this case also, the $\{\bar{C}_Q, \bar{\eta}\}$ values derived from models 3, 4, and 6 correspond to

the values for the intermediate dynamic component obtained from the deuterium MAS NMR spectra shown in Table 3.3, at 298 K. Appendix Figure B3.8 shows results from a $T_3$ configuration with hydroxyls positioned at 4.763 and 6.467 Å, corresponding to model (2) in Table 3.6. $\boldsymbol{d}_i(t)$ arising from the $-C_2D_2-NH_2$ part of the diamine provided an average quadrupolar coupling of 44 kHz, whereas $\boldsymbol{d}_i(t)$for =N- $C_1D_2$- resulted in 77 and 79 kHz. The difference in the averaged quadrupolar parameters arising from ($D_3$, $D_4$) and ($D_1$, $D_2$) is probably due to the additional rotational motion of $-C_2D_2-NH_2$ about the $C_1$ - $C_2$ bond. Similar rotational motion was not observed in diamine-GPTMS MD simulations perhaps due to the longer chain length and hence more complex dynamics. We did not encounter in our previous MD studies different averaged tensors arising from a single dynamic run, which may be attributed to the rigidity imparted by the double bond. Dynamic simulations were also performed with a $T_2$ configuration and four hydroxyls positioned at 2.771, 3.509, 3.911, and 3.751 Å, corresponding to model (5) in Table 3.6 and are shown in Appendix Figure B3.9 along with the averaged quadrupolar parameters. In order to investigate the dynamics with hydroxyls positioned differently, simulations were performed with a configuration given in model (7) in the Table 3.6, and the results are shown in Appendix Figure B3.10. Similar to previously reported studies, we have observed that the molecule got almost stabilized through $NH_2$---OH-Si and $(H_2)$C-O--- HO-Si hydrogen bonding, resulting in averaged quadrupolar couplings in the 153-156 kHz range, in agreement with the non-isotropic rigid component for the wet sample at 298 K. Representative plots showing the variation of the polar angle θ for diamine-GPTMS and diamine-MATMS are shown in Appendix Figure B3.11 and Figure B3.12. Similar to diamine-GPTMS, it can be seen that the averaged quadrupolar parameters derived from MD simulations agree with the range of parameters obtained from deuterium MAS NMR analysis. In the case of diamine-MATMS, the trajectory vectors are either confined within a rather narrow strip on the unit sphere, or spread over two or three regions, or over a single large region leading to quadrupolar parameters in the range of intermediate or large amplitude dynamic component, similar to diamine-GPTMS.

We have presented only a few geometrical arrangements of the silanols with respect to the molecule grafted, but it is unlikely to have large deviations of the calculated values while considering other geometrical arrangements. MD analysis suggests that a minimum of one hydroxyl in the vicinity of the linker may be sufficient to initiate dynamics of the linker, resulting in averaged quadrupolar parameters.

Apart from dynamics due to transitions between various molecular conformations in both samples resulting in averaged quadrupolar parameters, a few more points are discussed below. As shown in Table 3.4, the relative percentage of the rigid component is larger for the wet diamine-MATMS. This is supported by the MD simulation which shows stabilization of the linker to the surface through hydrogen bonding. However, in the case of diamine-GPTMS, with a maximum of four silanols and a few geometric arrangements, we did not observe the stabilization of the linker, perhaps due to the larger length of the molecule. As chain length increases, the segmental motion also increases, resulting in more dynamics as shown in Table 3.4.

## 3.4 Conclusions

In this chapter, $^{2}H$ MAS NMR spectra of methylene deuterated diamine functionalized GPTMS and MATMS grafted in SBA-15 were analysed for dynamics information as a function of temperature and hydration. Since applications of functionalized materials also depend on the degree of grafting, we have chosen two different grafting concentrations of the hybrid materials to monitor dynamics. Average quadrupolar parameters extracted from deconvoluted components of $^{2}H$ MAS NMR spectra are in similar ranges for both samples. Deconvolution of $^{2}H$ MAS NMR spectra resulted in (a) a rigid quadrupolar coupling constant indicating small-angle jumps, (b) an intermediate dynamic component, and (c) a large amplitude dynamic component. By assuming a simple *"small angle"* jump model, the jump angle corresponding to the rigid component resulting from the libration/local motion of $C-^{2}H_2$'s was calculated. The ratio between the rigid and sum of intermediate and large amplitude dynamic components is similar for diamine-GPTMS in both dry and wet states, whereas in diamine-MATMS it increases with hydration, signifying more restricted dynamics of the linker with an increase in hydration. This may be attributed to the smaller length of diamine-MATMS and/or to more restricted motion due to the –C=N− double bond in diamine-MATMS when compared with diamine-GPTMS.

It can be seen from the proton and deuterium spectral analysis in both samples that, with an increase in the relative percentage of bulk water from dry to wet, the large amplitude dynamic component increases substantially. This suggests that large amplitude dynamics is induced by bulk water in the vicinity of the linker. Similarly, we also observe a larger percentage of intermediate dynamic component in the dry state of both samples. This

supports the assumption that intermediate dynamics is induced by surface water and isolated silanols.

Subsequently, molecular dynamic simulations were performed with silanols occupying a few geometrical arrangements near the linker to mimic low and high hydration levels. The average quadrupolar couplings calculated from the MD output by analysing the time dependent trajectories of the C–$^{2}$H unit vectors were within the ranges provided by $^{2}$H MAS NMR spectral analysis. Inspection of the spatial distribution of trajectory vectors showed that dynamics resembling "two site" jump motion with almost equal population or "three site" jump motion with slightly varying population resulted in averaged values of the quadrupolar parameters corresponding to the range for the intermediate dynamic component found through NMR analysis. Depending on the position of the accessible silanols on the surface, a restricted distribution of trajectory vectors in a relatively narrow strip on the unit sphere also provided intermediate dynamic component. On the other hand, values of the averaged quadrupolar parameters in the range of the large amplitude dynamic component resulted from a spread of the trajectory vectors over an extended single region on the unit sphere.

MD simulations also provided molecular conformations associated with dynamics and stabilization of the linker with the surface through weak hydrogen bonding. MD simulations indicate that the intermediate and the large amplitude dynamic components derived from NMR data may be the result of transitions between different molecular conformations, including transition between *trans* and *gauche* conformations. For diamine-MATMS by increasing the number of accessible silanols on the surface, the linker gets stabilized through hydrogen bonding with the surface, in agreement with the analysis of NMR data. MD showed evidence of steric hindrance in diamine-MATMS, resulting in intermediate and large amplitude dynamic components arising from a single anchoring configuration.

Many reported studies demonstrate that the functional efficiency of the amine functionalized hybrid mesoporous materials depends on the kinetics of the linkers and the adsorption of guest molecules. Analysis of $^{2}$H MAS NMR spectra and the complementary insights derived from molecular dynamic simulations widen the understanding of molecular transport and binding in amine functionalized hybrid mesoporous materials.

# 4

# Summary and Discussions

Aim of this research is to characterize guest-host interactions at the molecular level in ethane substituted periodic mesoporous organosilicates and amine functionalized SBA-15 by employing $^{1}H$ and $^{2}H$ solid state magic angle spinning (MAS) NMR and MD simulations.

We have employed $^{1}H$ solid state MAS NMR to monitor the distribution of water clusters on the pore surface of ethane substituted periodic mesoporous organosilicate, $PMO_E$. By correlating the weight gain of the samples to the total integrated intensity of the recorded proton spectra at each hydration level, we have calculated the number of protons per $nm^2$ (*p* H $nm^{-2}$) on the pore surface. $PMO_E$ proton spectra acquired at different hydration levels are analysed and interpreted in terms of water clusters of various sizes according to the *p* values and the distribution of water layers on the pore surface. Distribution of water layers as a function of hydration enabled us to predict a pore filling model in $PMO_E$. For $PMO_E$ at moderate to high *p* values, the behaviour of spectral components upon hydration suggests that both radial and axial filling mechanisms play a significant role. This is in contrast to SBA-15, for which analysis of proton MAS NMR spectra as function of hydration suggests a predominantly radial pore-filling mechanism.

$^{2}H$ MAS NMR was employed to monitor the dynamics induced by surface adsorbed water molecules on two types of amine-functionalized SBA-15, diamine-GPTMS and diamine-MATMS, with different grafting concentrations. Amine functionalized linkers are used in this study due to their profound importance in $CO_2$ capture and in biomimetics, where the functional efficiency depends on the kinetics of the linkers and degree of adsorption of the mesoporous materials. Deconvolution of $^{2}H$ MAS NMR spectra resulted in (a) a rigid quadrupolar coupling constant indicating small-angle jumps, (b) an intermediate dynamic component, and (c) a large amplitude dynamic component. The ratio between the rigid and sum of intermediate and large amplitude dynamic components is similar for diamine-GPTMS in both dry and wet states, whereas in diamine-MATMS it increases with hydration, indicating more restricted dynamics of the linker with an increase in hydration. This may be attributed to the smaller length of diamine-MATMS and/or to more restricted motion due to the –C=N− double bond in diamine-MATMS when compared with diamine-GPTMS.

Analysis of deuterium and proton spectra suggests that one water molecule/$nm^2$ adsorbed near the linker may be sufficient to induce dynamics of the linkers thereby resulting in averaged quadrupolar parameters. Molecular Dynamic simulations were performed and the analysis of the time-dependent molecular trajectories lead to average quadrupolar parameters similar to those obtained from deuterium MAS NMR analysis. MD simulations also provided various molecular conformations associated with dynamics and indicated stabilization of the linker on the surface through weak hydrogen bonding. In the two samples studied, we found that difference in grafting concentration had negligible effect on the dynamics.

However, in many cases efficient performance of the functionalized materials depends on the grafting concentration and hence it would be interesting to monitor systematically the dynamics of linkers as a function of grafting concentration. Beyond a specific grafting concentration, dynamics of the linkers may get hindered due to intermolecular interaction. This may be reflected in the deuterium MAS NMR spectra as increased linewidths, change in relaxation times, or providing rigid-limit spinning-sideband patterns which are less sensitive to hydration or temperature. Due to lack of sensitivity, the methodology presented here may have limitations after a specific grafting concentration. This may require non-trivial development/application of additional experiments, incorporating perhaps NMR of other nuclei. In the case of $PMO_E$, investigation of distribution of water clusters was not performed as a function of temperature. With pore walls being both hydrophobic and hydrophilic, low temperature studies at different hydrations may provide further insight about the distribution of water on the pore surface. Nevertheless, the work presented here illustrates that analysis of NMR spectra and correlation with the molecular dynamics simulations can lead to a conclusive molecular level picture of structure and dynamics.

# Appendix A

## Proton MAS NMR analysis – $PMO_E$.

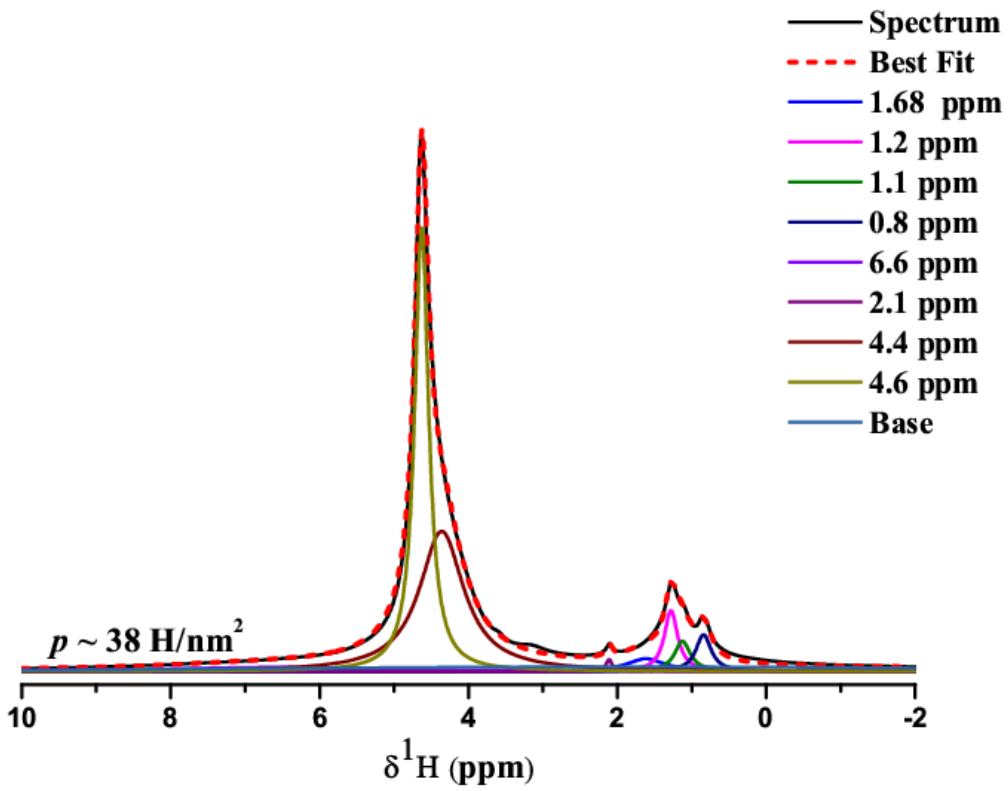


**Figure A2.1** Deconvolution of proton MAS spectrum of $PMO_E$ at $p$ ~ 38 H/nm$^2$ using DMFIT. The corresponding chemical shifts including the impurities (2.1 ppm (~0.2%), 1.2, 0.8 ppm) are indicated along with the best fit.

| $p$ (H/nm$^2$) | 1.62 ppm (%) | 1.13ppm (%) | 4.4 ppm (%) | 4.63 ppm (%) | 6.59 ppm (%) |
|---|---|---|---|---|---|
| 38 | 3.6 | 3.5 | 50.4 | 34.8 | 7.7 |

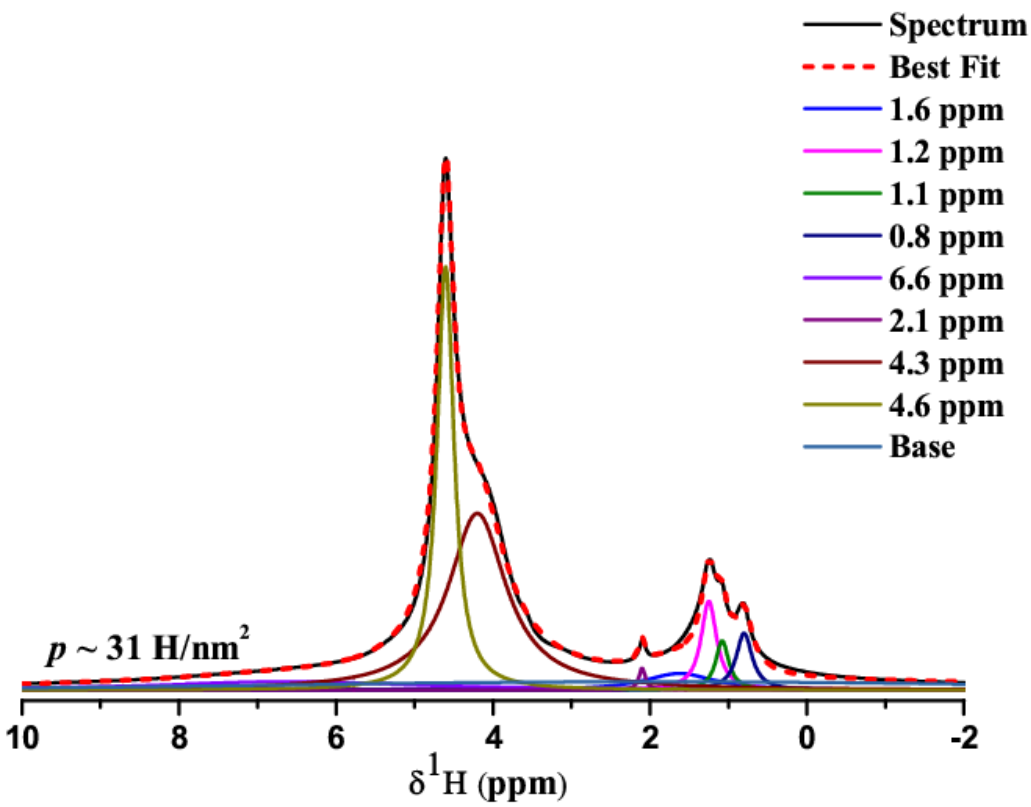


**Figure A2.2** Deconvolution of proton MAS spectrum of $PMO_E$ at $p$ ~ 31 H/nm$^2$ using DMFIT. The corresponding chemical shifts including the impurities (2.1 ppm (~0.2%), 1.2, 0.8 ppm) are indicated along with the best fit. The percentages of the relative integrated intensity after subtraction of the impurity peaks are given.

| $p$ (H/nm$^2$) | 1.63 ppm (%) | 1.1 ppm (%) | 4.3 ppm (%) | 4.6 ppm (%) | 6.6 ppm (%) |
|---|---|---|---|---|---|
| 31 | 5.3 | 3.2 | 48.3 | 34.9 | 8.3 |

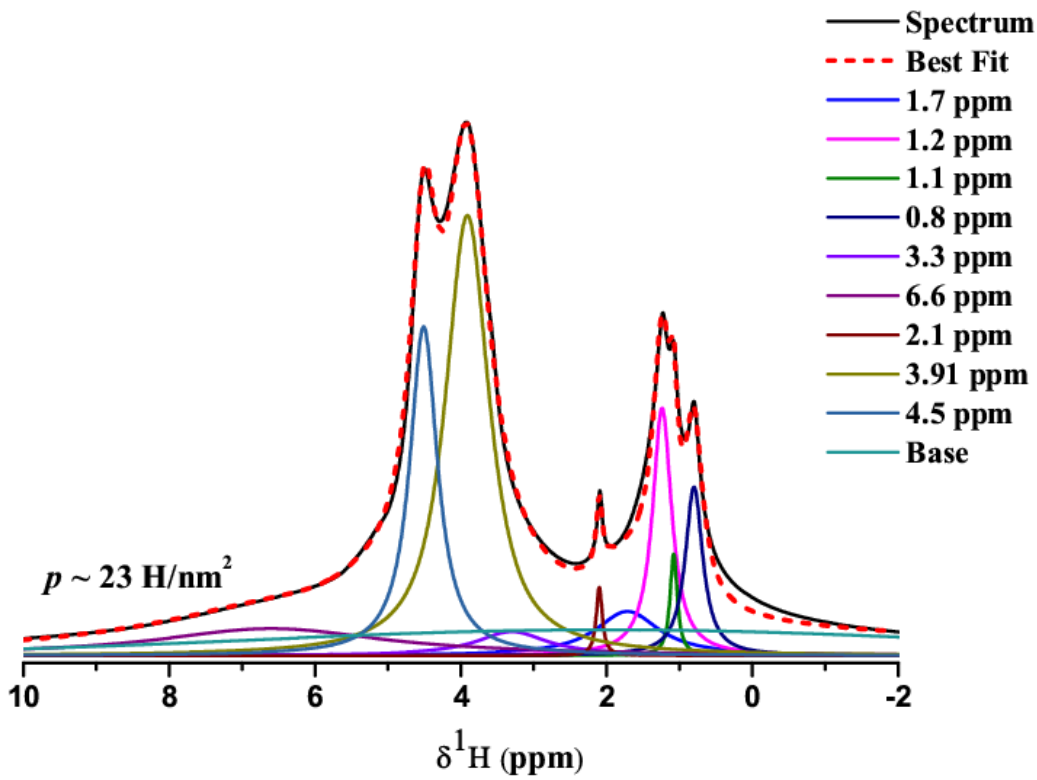


**Figure A2.3** Deconvolution of proton MAS spectrum of $PMO_E$ at $p$ ~ 23 H/nm$^2$ using DMFIT. The corresponding chemical shifts including the impurities (2.1 ppm (~0.2%), 1.2, 0.8 ppm) are indicated along with the best fit. The percentages of the relative integrated intensity after subtraction of the impurity peaks are given.

| $p$ (H/nm$^2$) | 1.71 ppm (%) | 1.06 ppm (%) | 3.3 ppm (%) | 3.91 ppm (%) | 4.51 ppm (%) | 6.6 ppm (%) |
|---|---|---|---|---|---|---|
| 23 | 7.2 | 3.9 | 4.4 | 48.7 | 24.4 | 11.4 |

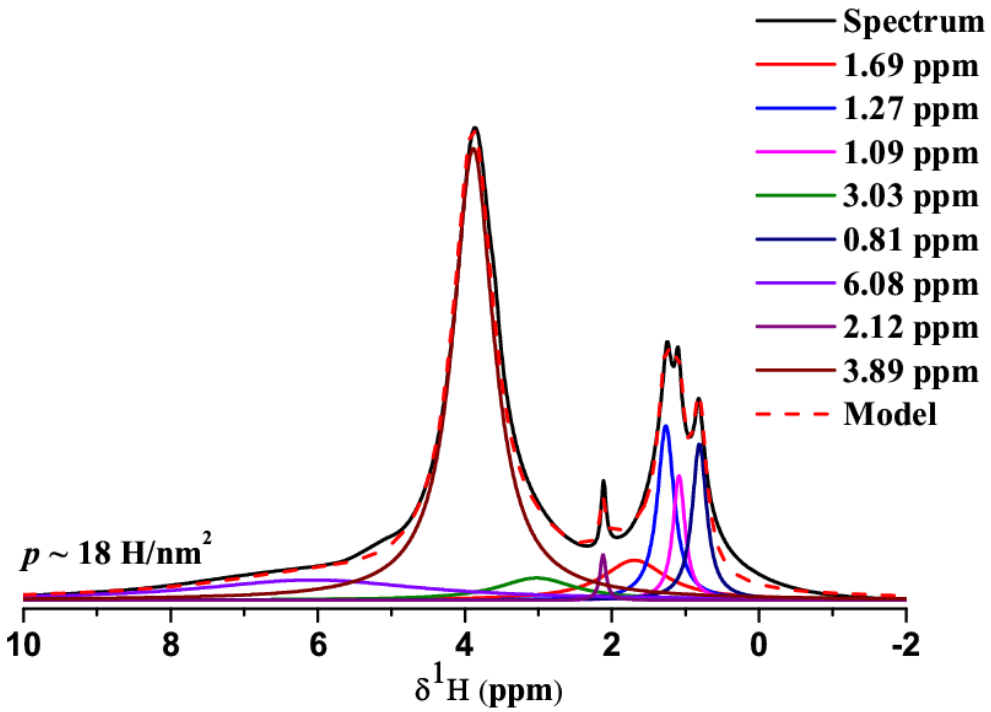


**Figure A2.4** Deconvolution of proton MAS spectrum of $PMO_E$ at $p$ ~ 18 H/nm$^2$ using DMFIT. The corresponding chemical shifts including the impurities (2.1 ppm (~0.2%), 1.2, 0.8 ppm) are indicated along with the best fit. The percentages of the relative integrated intensity after subtraction of the impurity peaks are given.

| $p$ (H/nm$^2$) | 1.64 ppm (%) | 1.1 ppm (%) | 3.3 ppm (%) | 3.9 ppm (%) | 6.08 ppm (%) |
|---|---|---|---|---|---|
| 18 | 11.2 | 3.0 | 4.5 | 66.7 | 14.6 |

## Proton MAS NMR analysis – SBA-15.

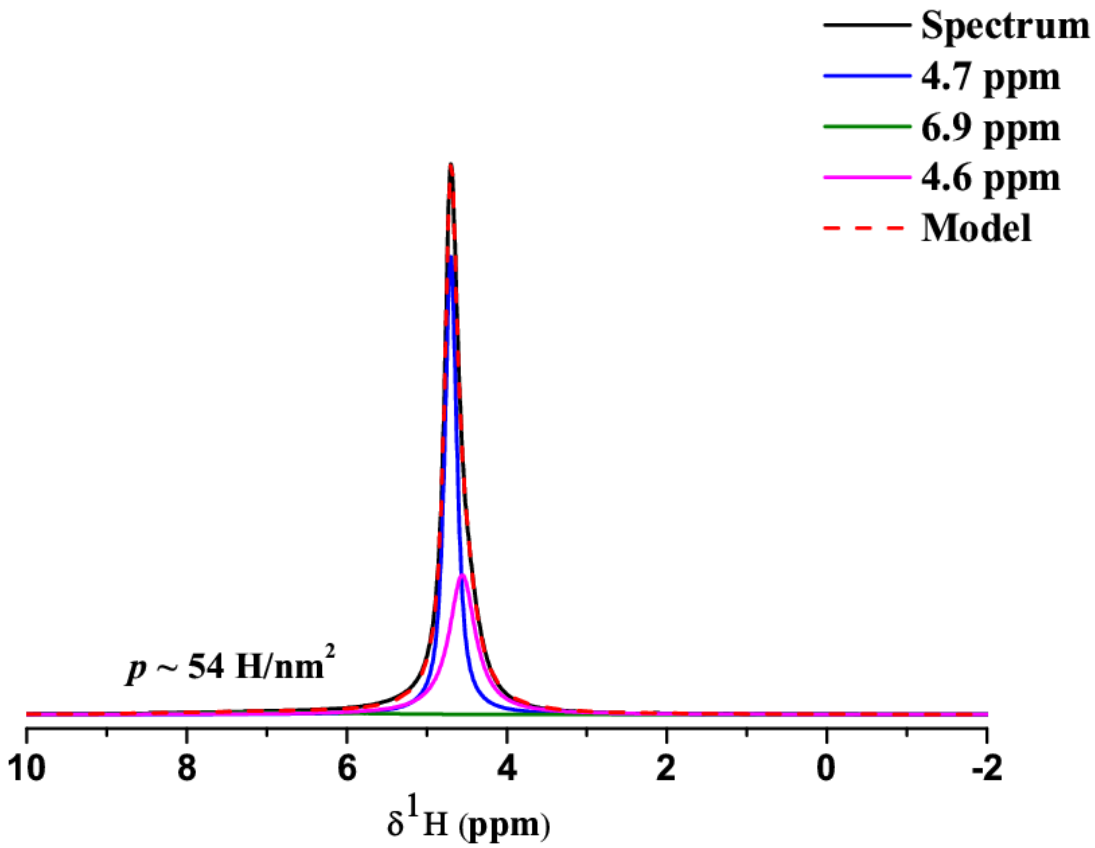


**Figure A2.5** Deconvolution of proton MAS spectrum of SBA-15 at $p$ ~ 54 H/nm$^2$ using DMFIT.

| $p$ (H/nm$^2$) | 4.6 ppm (%) | 4.4 ppm (%) | 6.9 ppm (%) |
|---|---|---|---|
| 54 | 57 | 40 | 3 |

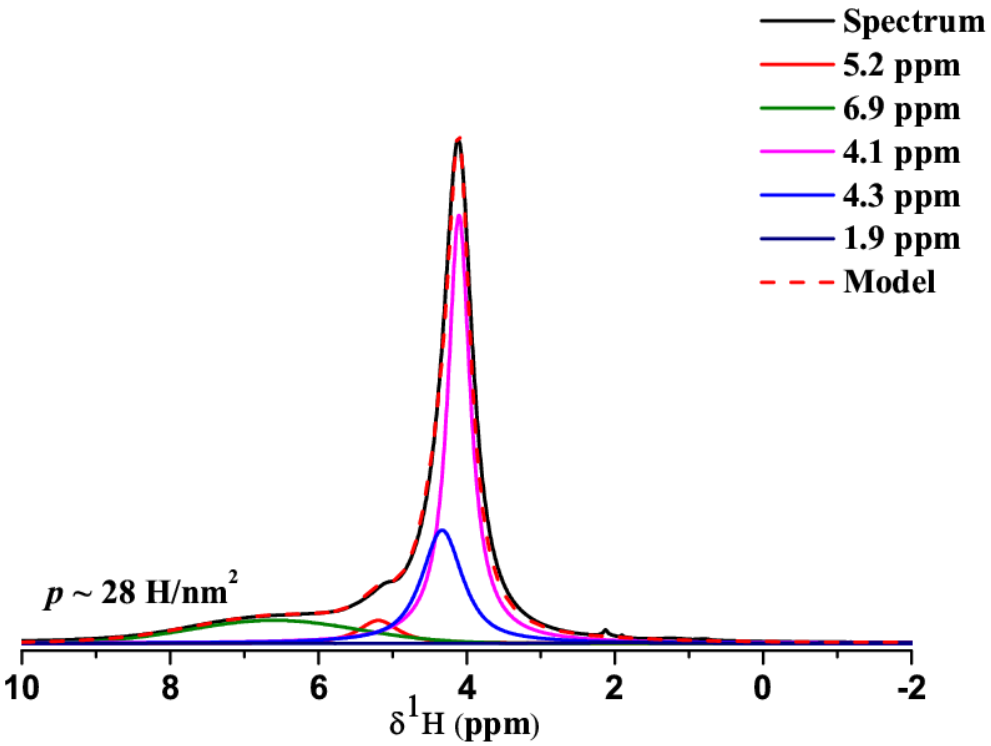


**Figure A2.6** Deconvolution of proton MAS spectrum of SBA-15 at $p$ ~ 28 H/nm$^2$ using DMFIT.

| $p$ (H/nm$^2$) | 1.9 ppm (%) | 4.1ppm (%) | 4.3 ppm (%) | 5.2 ppm (%) | 6.9 ppm (%) |
|---|---|---|---|---|---|
| 28 | 0.5 | 55.5 | 24.5 | 4.8 | 14.7 |

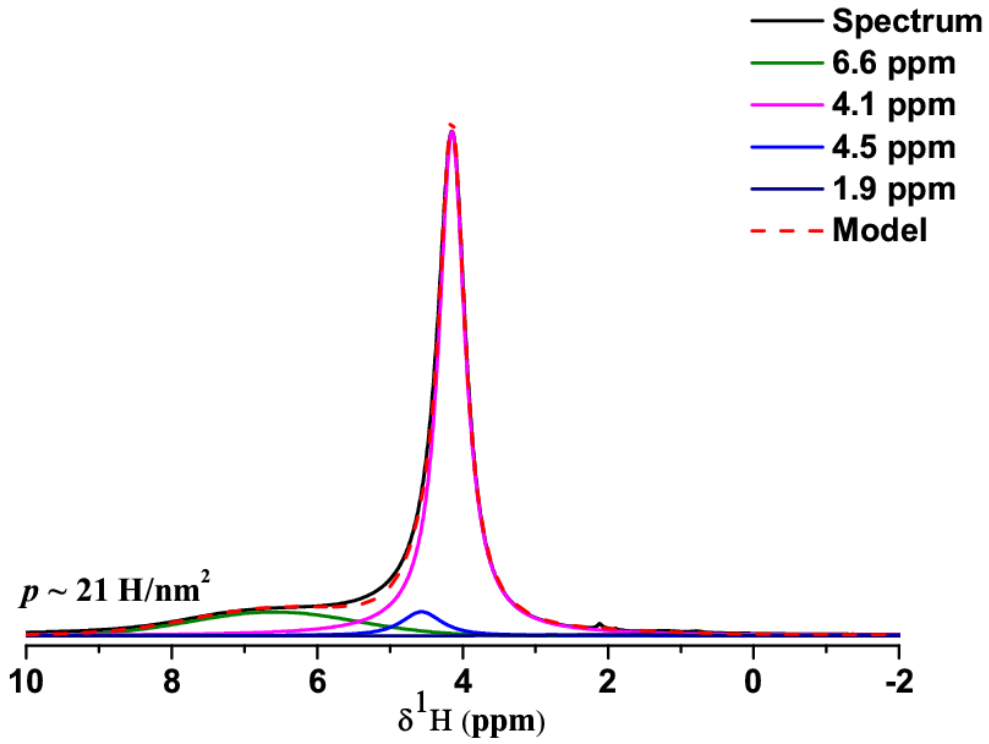


**Figure A2.7** Deconvolution of proton MAS spectrum of SBA-15 at $p$ ~ 21 H/nm$^2$ using DMFIT.

| $p$ (H/nm$^2$) | 1.9 ppm (%) | 4.1 ppm (%) | 4.5 ppm (%) | 6.6 ppm (%) |
|---|---|---|---|---|
| 21 | 0.8 | 78.5 | 5.3 | 15.4 |

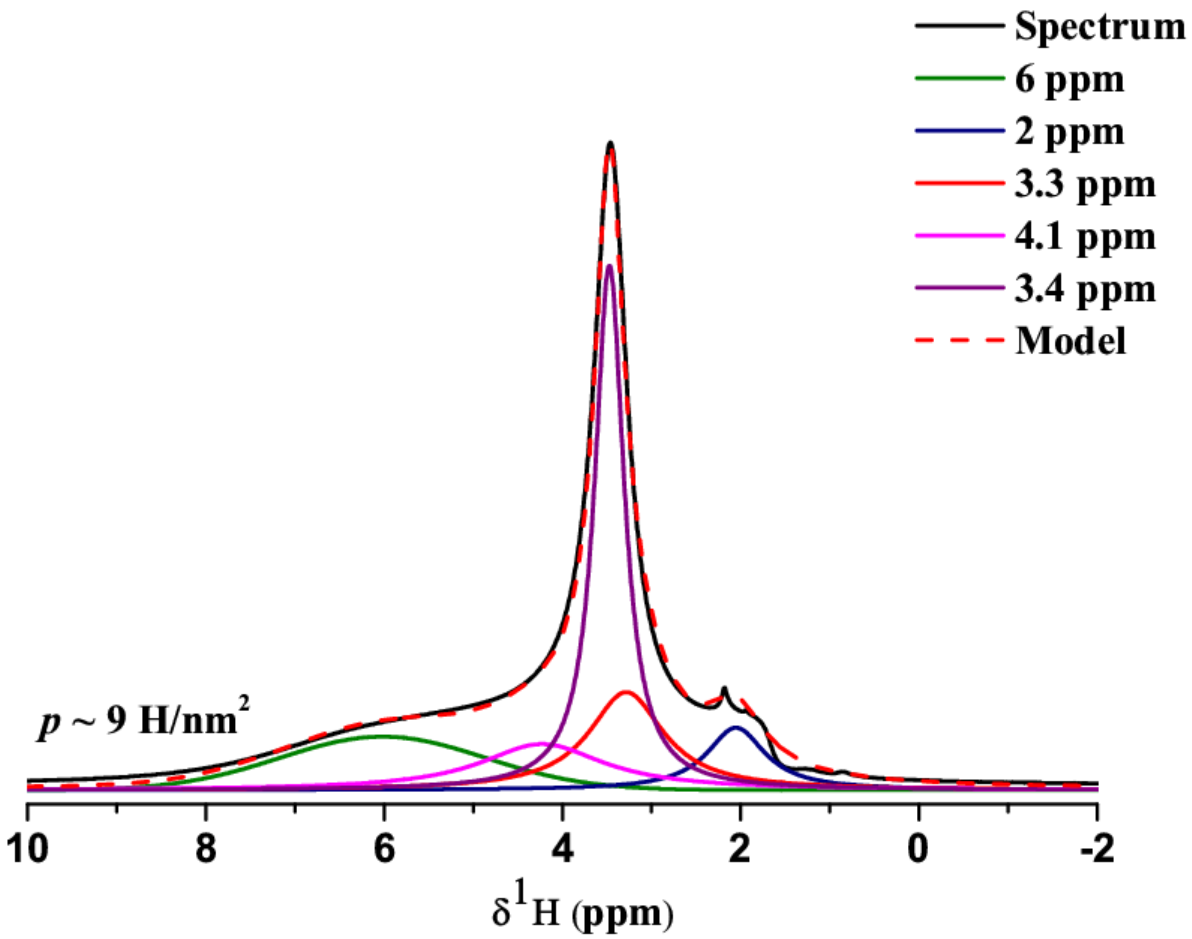


**Figure A2.8** Deconvolution of proton MAS spectrum of SBA-15 at $p$ ~ 9 H/nm$^2$ using DMFIT.

| $p$ (H/nm$^2$) | 2 ppm (%) | 3.3 ppm (%) | 3.4 ppm (%) | 4.1 ppm (%) | 6 ppm (%) |
|---|---|---|---|---|---|
| 9 | 9.3 | 18.7 | 39 | 14.6 | 18.4 |

# Appendix B

## Deuterium MAS NMR spectral analysis

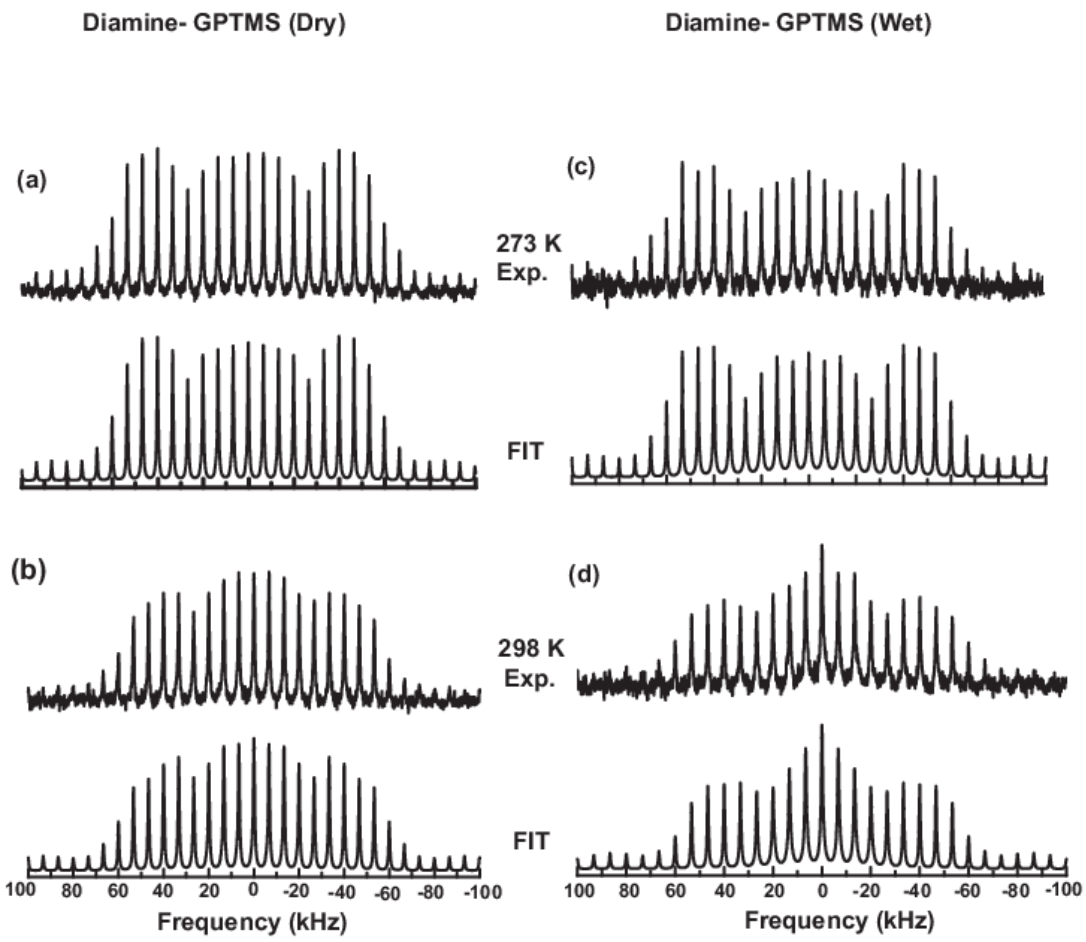


**Figure B3.1** Diamine-GPTMS $^{2}H$ MAS NMR spectra recorded at 6666 Hz MAS, for temperatures 273 and 298 K, along with their best fit are shown for the wet and dry states of the sample. Best fit spectra are obtained by summing the individual deconvoluted components

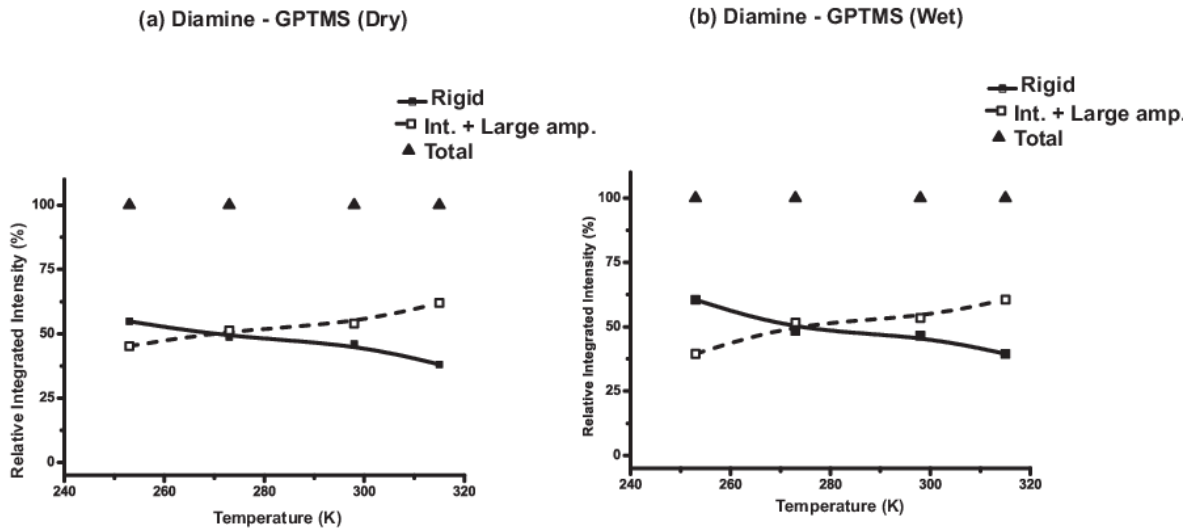


**Figure B3.2** Percentage of rigid (■) and sum of intermediate and large amplitude dynamic components (□) as function of temperature for the dry and wet states of diamine-GPTMS. The total sum (▲) is shown at the top of the plot.

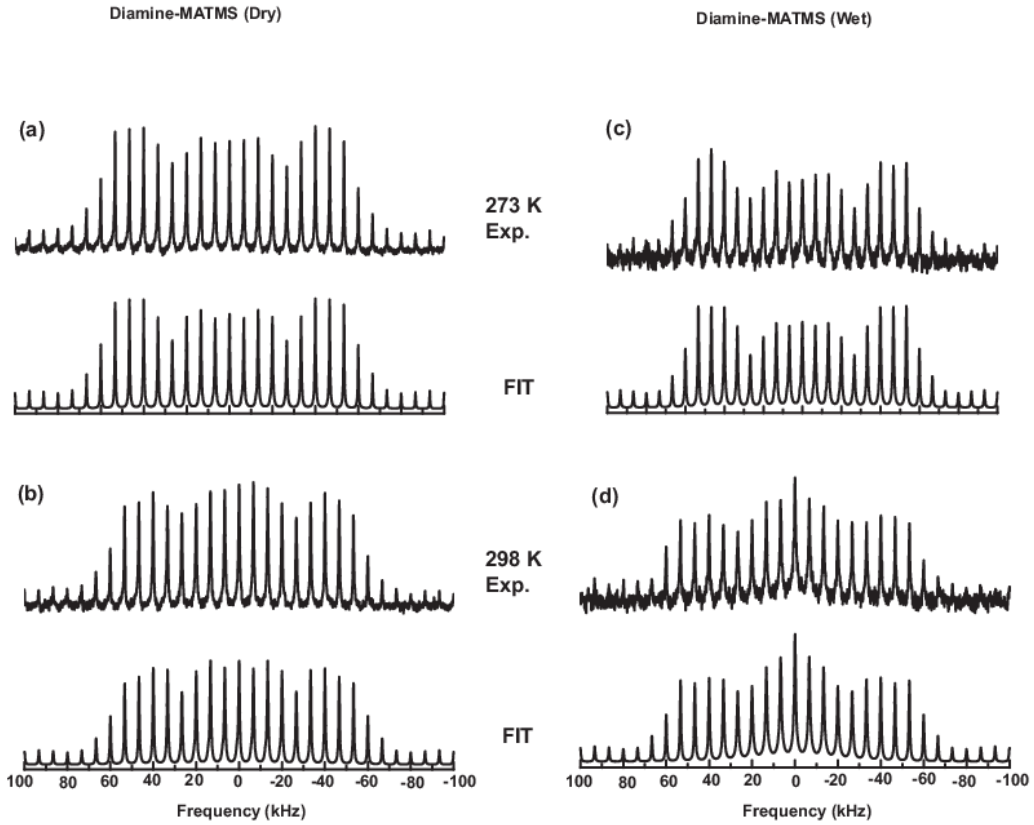


**Figure B3.3** Diamine-MATMS $^{2}H$ MAS NMR spectra recorded at 6666 Hz MAS, for temperatures 273 and 298 K, along with their best fit are shown for the wet and dry states of the sample. Best fit spectra are obtained by summing the individual deconvoluted components.

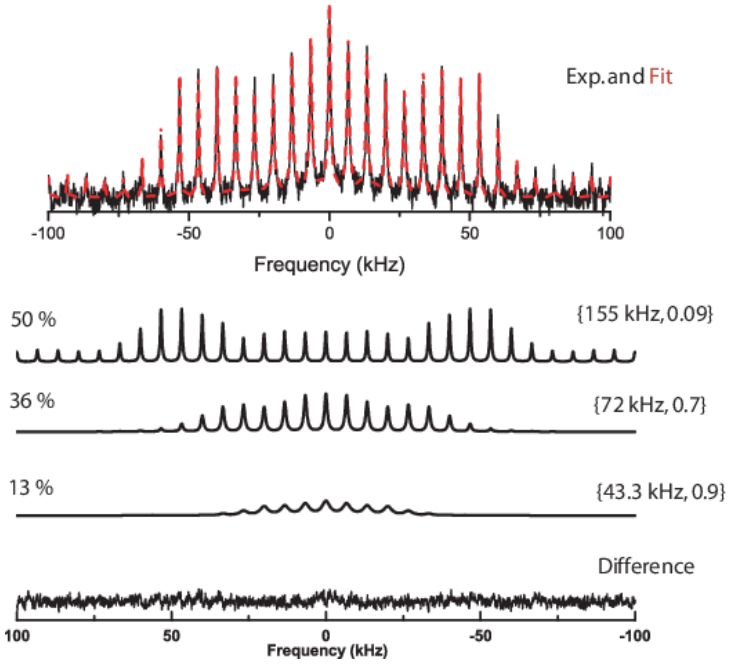


**Figure B3.4a** Diamine-MATMS $^{2}$H MAS NMR spectra recorded at 6666 Hz MAS, and 298 K for the wet state. The relative percentage of integrated intensity and the averaged quadrupolar parameters of the deconvoluted components are shown in the plot.

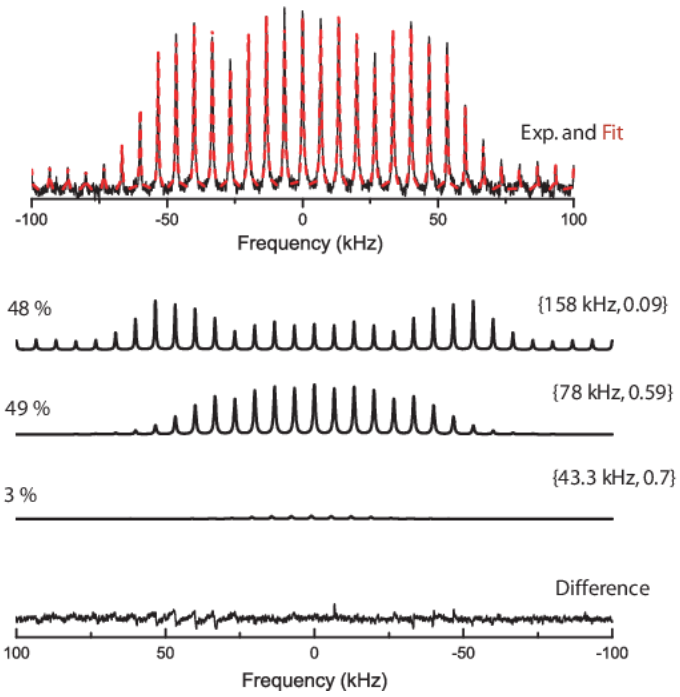


**Figure B3.4b** Diamine-MATMS $^{2}$H MAS NMR spectra recorded at 6666 Hz MAS, and 298 K for the dry state. The relative percentage of integrated intensity and the averaged quadrupolar parameters of the deconvoluted components are shown in the plot. The large amplitude dynamic component contributes very little to the best fit.

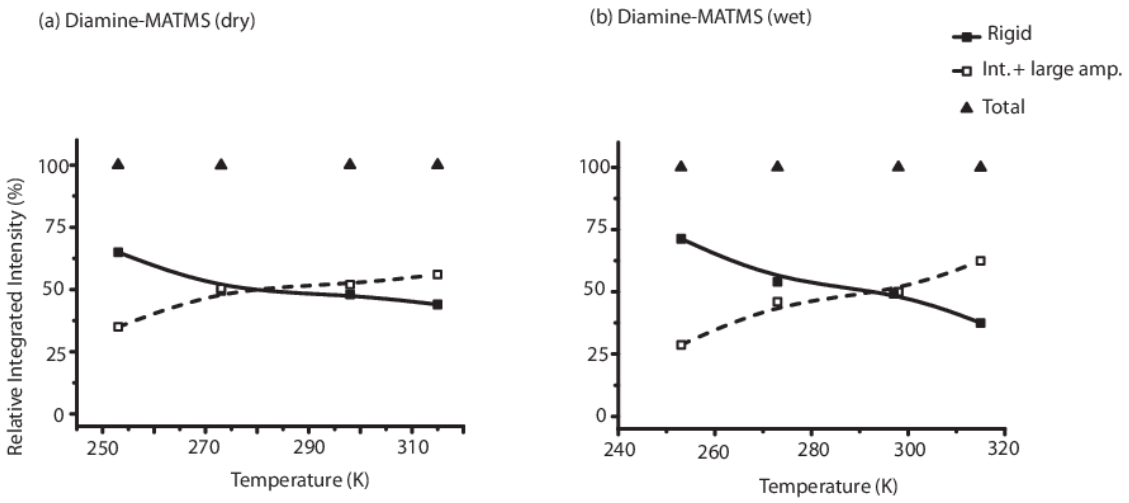


**Figure B3.5** Percentage of rigid (■) and sum of intermediate and large amplitude dynamic components (□) as function of temperature for the dry and wet states of diamine-MATMS. The total sum (▲) is shown at the top of the plot.

# Analysis of Molecular Dynamic Simulations

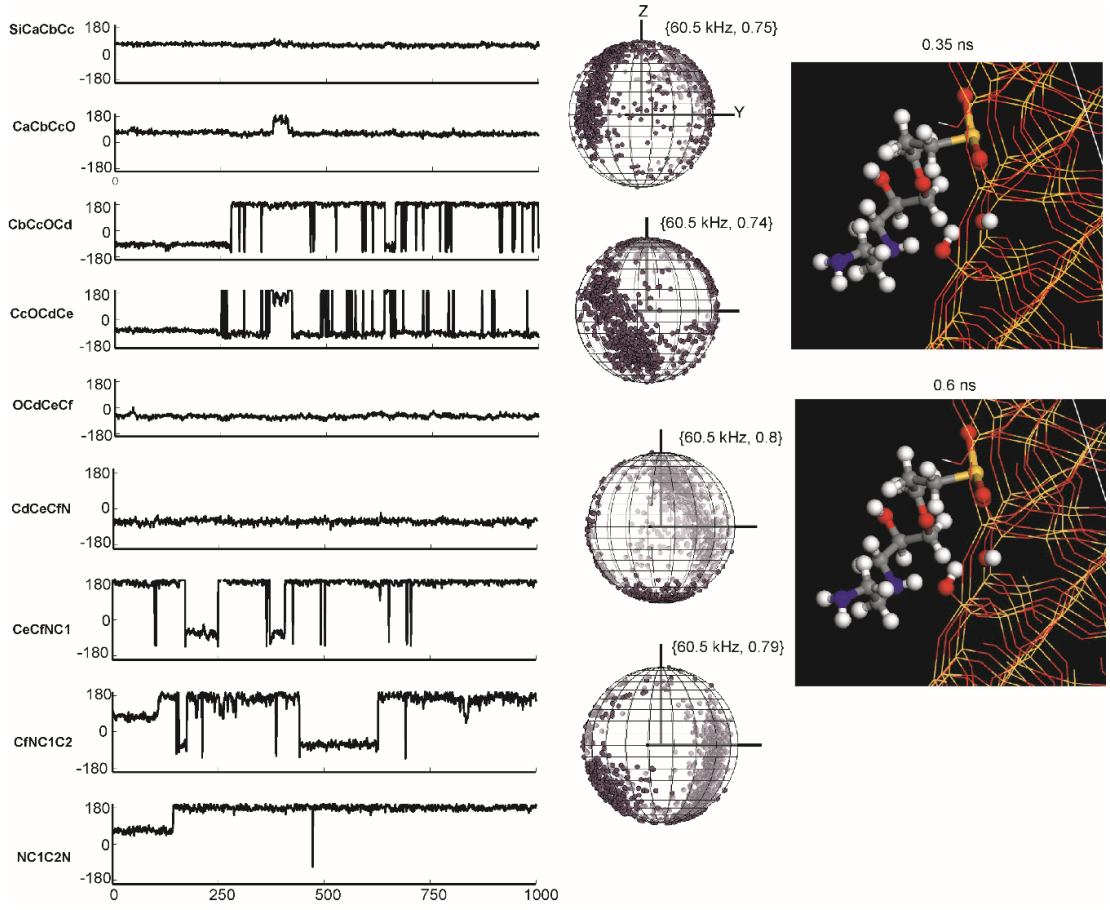


**Figure B3.6** MD calculations for diamine-GPTMS in $T_3$ configuration and three hydroxyls positioned at 4.468, 4.713 and 5.043 Å from the anchoring silicon atom (model (4) in Table 3.5 (Chapter 3). Time dependence of dihedral angles (left), spatial variation of $C-^2H$ vectors (middle), and molecular conformations (right) derived from MD. Averaged quadrupolar parameters are shown nearby. Yellow (Si), red (O), grey (C), blue (N), and white (H) are the colour codes for the respective atoms.

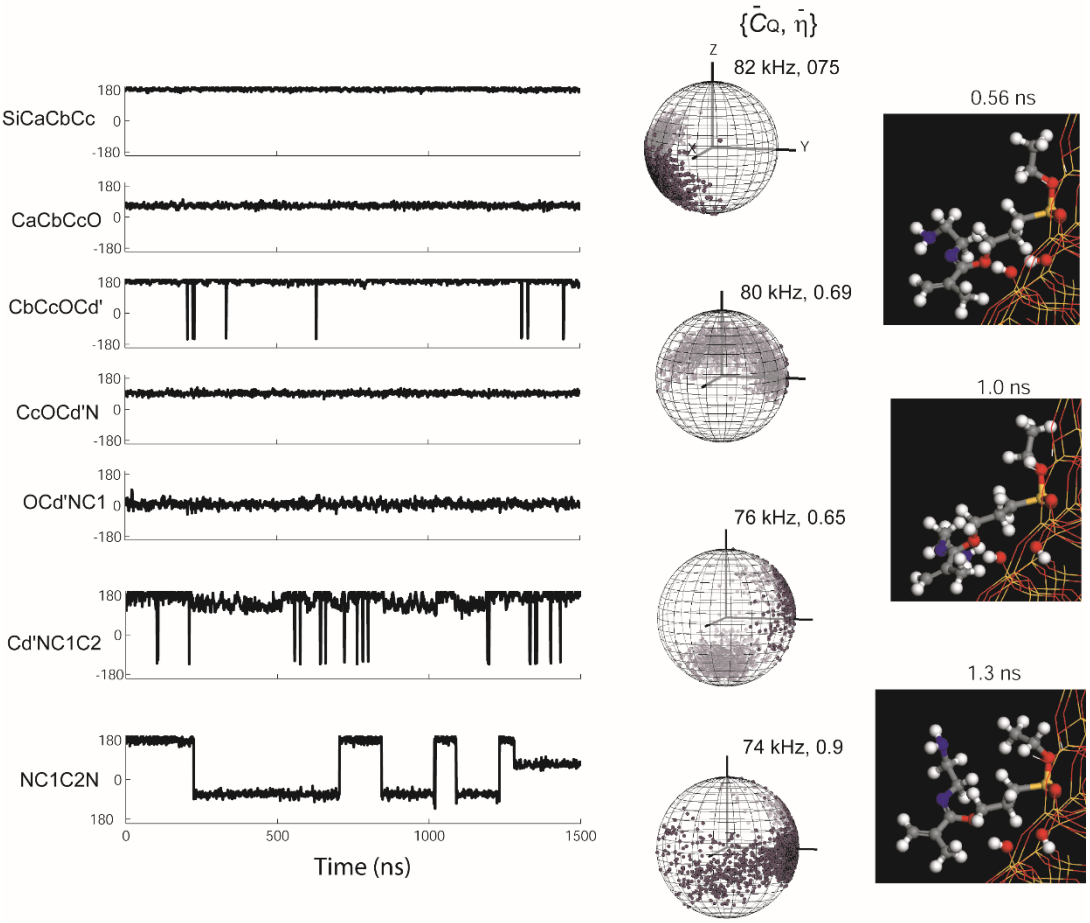


**Figure B3.7** MD calculations for diamine-MATMS in $T_2$ configuration and four hydroxyls positioned at a distance of 3.022, 3.811, 3.511, and 4.673 Å from the anchoring silicon atom (model (3) in Table 3.6 (Chapter 1)). Time dependence of dihedral angles (left), spatial variation of $C-^2H$ vectors (middle), and molecular conformations (right) derived from MD. Averaged quadrupolar parameters are shown nearby. The time dependence of dihedral angles shows very limited dynamics along the chain except for the end group. Dynamics of $–C_2\text{-}^2H_2\text{-}NH_2$ provides an averaged quadrupolar coupling of 74 and 76 kHz, whereas for $=N\text{-}\ C_1\text{-}^2H_2\text{-}$ it is 80 and 82 kHz. Yellow (Si), red (O), grey (C), blue (N), and white (H) are the colour codes for the respective atoms.

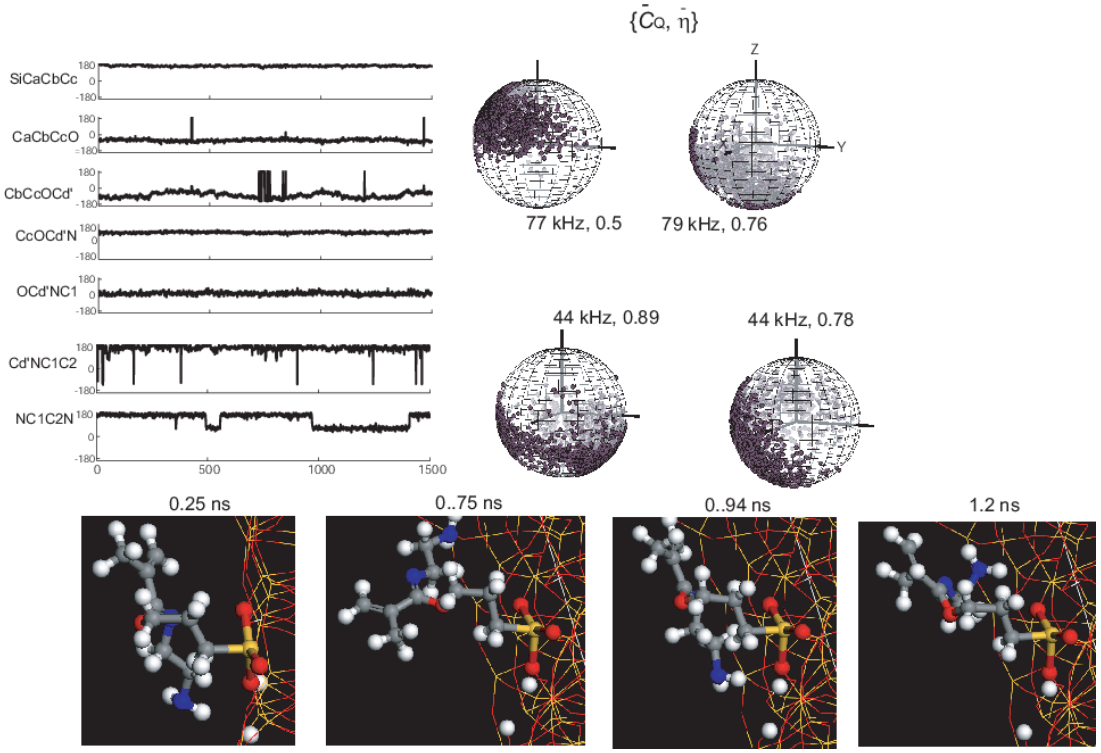


**Figure B3.8** MD calculations for diamine-MATMS in $T_3$ configuration and two silanols positioned at 4.763 and 6.467 Å from the anchoring silicon atom (model (2) in Table 3.6 (Chapter 3)). Time dependence of dihedral angles (left), spatial variation of $C-^2H$ vectors (middle), and molecular conformations (right) derived from MD. Averaged quadrupolar parameters are shown nearby. The time dependence of dihedral angles shows very limited dynamics along the chain except for the end group. Dynamics of $–C_2-^2H_2-NH_2$ provides an averaged quadrupolar coupling of 44 kHz, whereas for =N- $C_1-^2H_2-$ it is 77 and 79 kHz. Yellow (Si), red (O), grey (C), blue (N), and white (H) are the colour codes for the respective atoms.

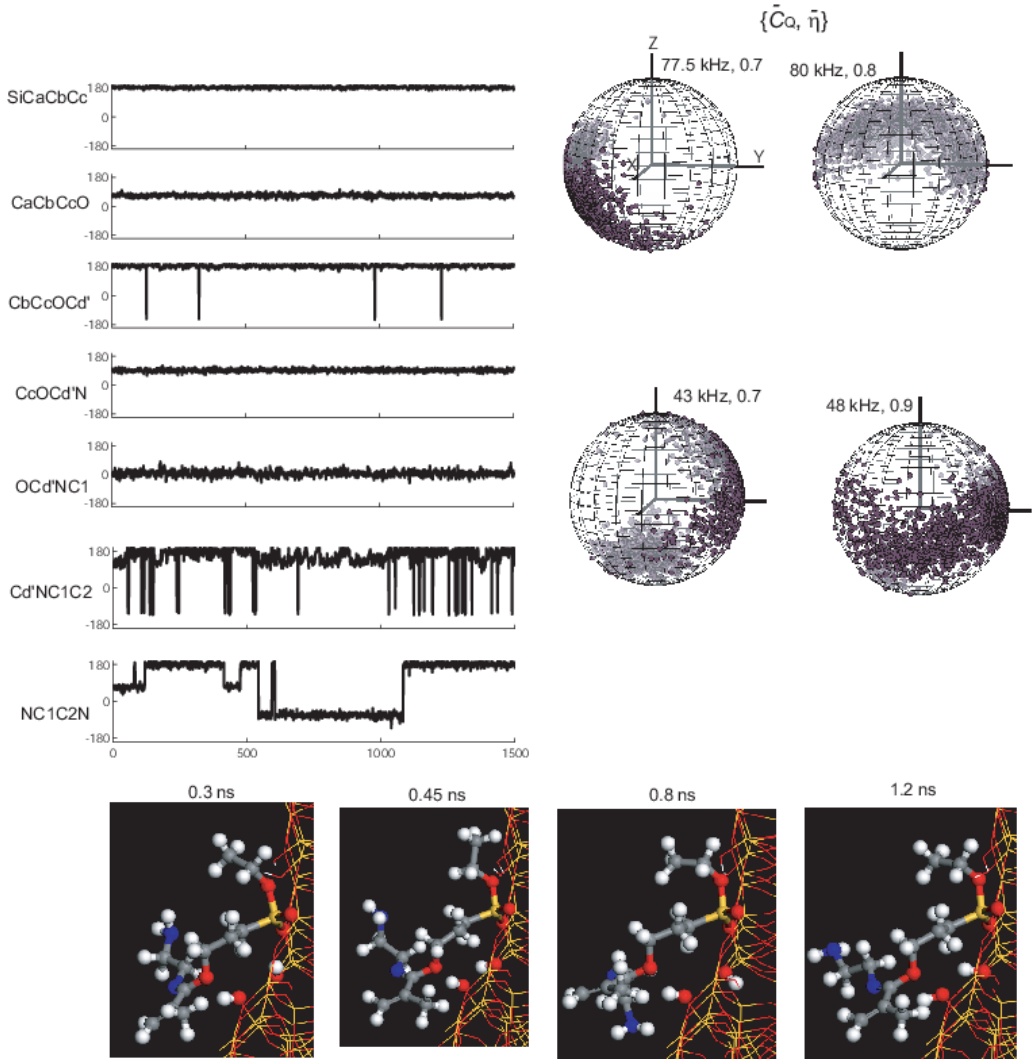


**Figure B3.9** MD calculations for diamine-MATMS in $T_2$ configuration and four hydroxyls positioned at 2.771, 3.509, 3.911, and 3.751 Å from the anchoring silicon atom (model (5) in Table 3.6 (Chapter 3)). Time dependence of dihedral angles (left), spatial variation of $C-^2H$ vectors (right), and molecular conformations (bottom) derived from MD. Averaged quadrupolar parameters are shown nearby. The time dependence of dihedral angles shows very limited dynamics along the chain except for the end group. Dynamics of $-C_2-^2H_2-NH_2$ provides an averaged quadrupolar coupling of 43 and 48 kHz, whereas for =N- $C_1-^2H_2-$ it is 77 and 80 kHz. Yellow (Si), red (O), grey (C), blue (N), and white (H) are the colour codes for the respective atoms.

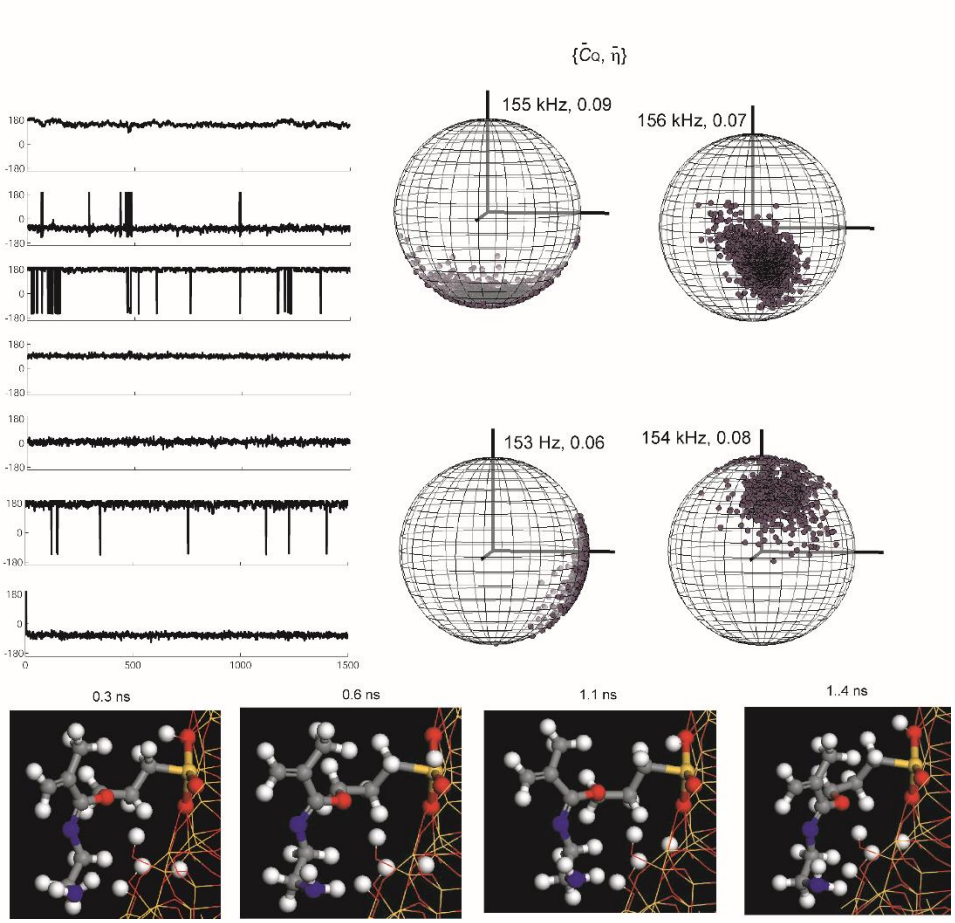


**Figure B3.10** MD calculations for diamine-MATMS in $T_3$ configuration and four hydroxyls positioned at 4.358, 4.598, 6.744 and 8.649 Å from the anchoring silicon atom (model (7) in Table 3.6 (Chapter 3)). Time dependence of dihedral angles (left), spatial variation of $C-^2H$ vectors (right), and molecular conformations (bottom) derived from MD. Averaged quadrupolar parameters are shown nearby. The time dependence of dihedral angles shows very limited dynamics along the chain. The molecule got almost stabilised through $NH_2$---OH-Si and $(H_2)$C-O---HO-Si hydrogen bonding resulting in averaged quadrupolar couplings in the 153-156 kHz range in agreement with the rigid component for the wet sample at 298K. Yellow (Si), red (O), grey (C), blue (N) and white (H) are the colour codes for the respective atoms.

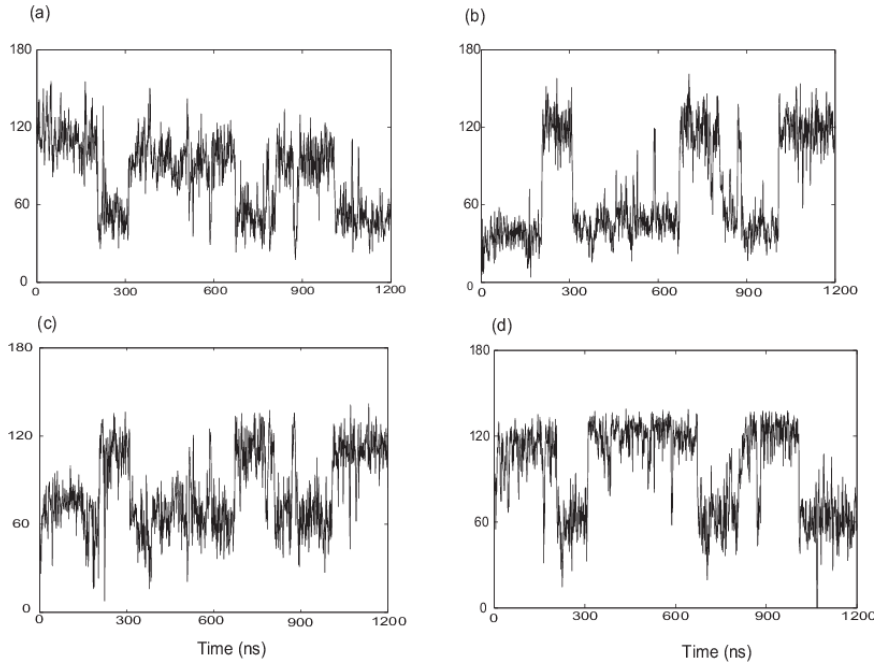


**Figure B3.11** Time dependence of the polar angle $\theta$ for $C_1$-$^2H_{1,2}$ (a,b) and $C_2$-$^2H_{3,4}$ (c,d) for diamine-GPTMS and the model described in Figure 3.10.

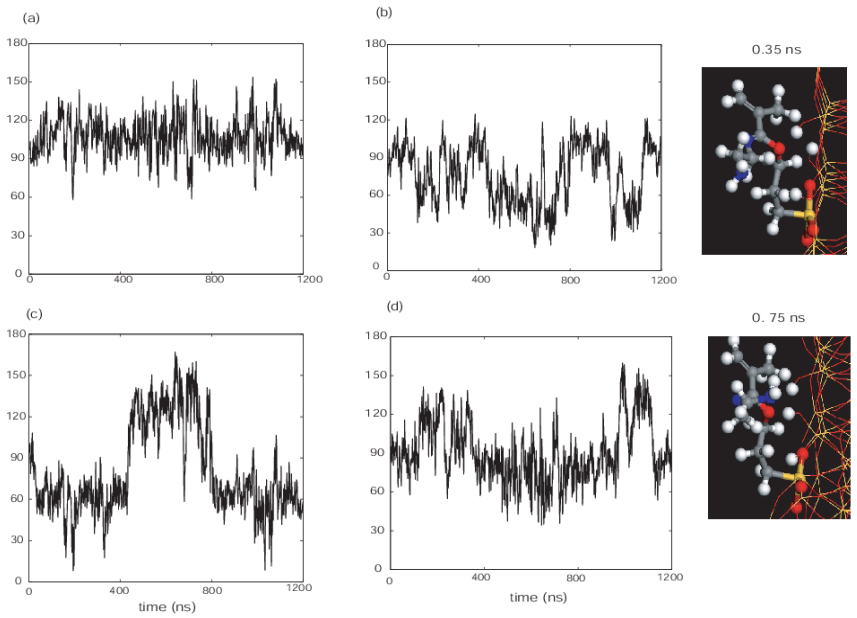


**Figure B3.12** Time dependence of the polar angle $\theta$ for $C_1$-$^2H_{1,2}$ (a,b) and $C_2$-$^2H_{3,4}$ (c,d) for diamine-MATMS and the model (6) given in Table 3.6. Molecular conformations are shown nearby.

# Abbreviations

| | |
|---|---|
| NMR | Nuclear Magnetic Resonance |
| RF | Radio Frequency |
| MAS | Magic Angle Spinning |
| CP | Cross Polarization |
| MRS | Magnetic Resonance Spectroscopy |
| DNP | Dynamic Nuclear Polarization |
| FWHM | Full Width at Half Maximum |
| PAS | Principal Axis system |
| CSA | Chemical Shift Anisotropy |
| SIMPSON | SIMulation Program for SOlid state NMR |
| EFG | Electric Field Grandient |
| SNR | Signal to Noise Ratio |
| M41S | Mesoporous 41 molecular Sieves |
| MCM-41 | Mobil Crystalline Materials-41 |
| SBA-15 | Santa Barbara Amorphous-15 |
| PMO | Periodic Mesoporous Organosilicates |
| $PMO_E$ | Ethane substituted Periodic Mesoporous Organosilicate |
| FTIR | Fourier Transform Infrared Spectroscopy |
| XRD | X-Ray Diffraction |
| TEM | Transmission Electron Microscopy |
| SEM | Scanning Electron Microscopy |
| BET | Brunauer-Emmet-Teller |
| BJH | Barrett-Joyner-Halenda |
| DRS | Dielectric Relaxation Spectroscopy |
| EPR | Electron Paramagnetic Resonance |

| | |
|---|---|
| QENS | Quasi Elastic Neutron Scattering |
| EXPRESS | Exchange Program for Relaxing Spin Systems |
| KLDMAS | Lysine (K), Leucine(L), Dynamic MAS |
| DFT | Density Functional Theory |
| XC | eXchange and Correlation |
| AMID | Ab Initio Molecular Dynamics |
| MD | Molecular Dynamics |
| CASTEP | CAmbridge Serial Total Energy Package |
| VASP | Vienna Ab initio Simulation Package |
| GIPAW | Gauge Including Projector Augmented Wave |
| COMPASS | Condensed-phase Optimized Molecular Potentials for Atomistic Simulation Studies |
| GPTMS | Glycidyloxy Propyl Trimethoxy Silane |
| MATMS | (trimethoxysilyl)propylmethacrylate |
| SENS | Surface Enhanced NMR Spectroscopy |
| HETCOR | Heteronuclear Correlation |
| VCT | Variable Contact Time |
| WISE | WIde-line Separation |
| P123 | Pluronic123 |
| TEOS | TetraEthylOrthoSilicate |
| BTEE | Bis-(TriEthoxysilyl) Ethane |

# Publications

## Refereed Journals

1. V. S. Veena, I. Kavya, A. Lazar, C. P. Vinod, T. G. Ajithkumar, S. Jayanthi. Distribution of Water in the Pores of Periodic Mesoporous Organosilicates – a Proton Solid State MAS NMR Study, ***Phys. Chem. Chem. Phys***.,**20(46),** 29351-29361, (**2018**). https://doi.org/10.1039/C8CP04902E

2. V. S. Veena, I. Kavya, A. Lazar, C. P.Vinod, T. G. Ajithkumar, S. Jayanthi, Dynamics in Amine-Functionalized Mesoporous Hybrid Materials Probed through Deuterium MAS NMR and Molecular Dynamic Simulations, ***J. Phys. Chem. C***, **124(11),** 6154-6170, (**2020**). https://doi.org/10.1021/acs.jpcc.9b11948

# Bibliography


[1] F. Bloch, W. W. Hansen, and M. E. Packard, Nuclear Induction, Phys. Rev. **69** 127 1946. https://doi.org/10.1103/PhysRev.69.127

[2] E. M. Purcell, H. C. Torrey, R. V. Pound, Resonance Absorption by Nuclear Magnetic Moments in a Solid, Phys. Rev. **69** 37-38 1946. https://doi.org/10.1103/PhysRev.69.37

[3] A. Abragam, The Principles of Nuclear Magnetism, (International Series of Monographs on Physics.), Oxford: Clarendon Press; London: Oxford University Press 1961.

[4] C. P. Slichter, Principles of Magnetic Resonance, 3rd Eds., Springer-Verlag Berlin Heidelberg 1996. https://doi.org/10.1007/978-3-662-09441-9

[5] R. R. Ernst, W. A. Anderson, Application of Fourier Transform Spectroscopy to Magnetic Resonance, Rev. Sci. Instrum. **37** 93-102 1966. https://doi.org/10.1063/1.1719961

[6] R. R Ernst, G. Bodenhausen, A. Wokaun, Principles of Nuclear Magnetic Resonance in One and Two Dimensions, (International Series of Monographs on Chemistry 14) Oxford: Clarendon Press; New York: Oxford University Press 1987.

[7] M. Goldman, Quantum Description of High-Resolution NMR in Liquids, (International Series of Monographs on Chemistry, 15) Oxford: Clarendon Press; New York: Oxford University Press 1988.

[8] J. Keeler, Understanding NMR Spectroscopy, John Wiley & Sons Ltd, Chichester, 2002. https://doi.org/10.17863/CAM.968

[9] M. H. Levitt, Spin dynamics: Basics of nuclear magnetic resonance (2nd Eds.). Chichester, West Sussex, England; N.J. Hoboken, John Wiley & Sons Ltd., 2008.

[10] M. Mehring, Principles of High-Resolution NMR in Solids, Springer-Verlag Berlin Heidelberg, 1983. https://doi.org/10.1007/978-3-642-68756-3

[11] K. Schmidt-Rohr, H. W. Spiess, Multidimensional Solid-State NMR and Polymers, Academic Press 1994.

[12] M. J. Duer, Solid state NMR spectroscopy. Principles and Applications, Blackwell Publishing Ltd., UK 2001. https://doi.org/10.1002/9780470999394

[13] M. J. Duer, Introduction to Solid-State NMR Spectroscopy, Blackwell Publishing Ltd, Oxford, UK 2004.

[14] E. R. Andrew, A. Bradbury, R. G. Eades, Nuclear Magnetic Resonance Spectra from a Crystal rotated at High Speed, Nature **182** 1659 1958. https://doi.org/10.1038/1821659a0

[15] E. R. Andrew, A. Bradbury, R. G. Eades, Removal of Dipolar Broadening of Nuclear Magnetic Resonance Spectra of Solids by Specimen Rotation, Nature **183** 1802–1803 1959. https://doi.org/10.1038/1831802a0

[16] I. J. Lowe, Free Induction Decay of Rotating Solids, Phys. Rev. Lett. **2** 285–287 1959. https://doi.org/10.1103/PhysRevLett.2.285

[17] M. M. Maricq, J. S. Waugh, NMR in Rotating Solids, J. Chem. Phys. **70** 3300-3316 1979. https://doi.org/10.1063/1.437915

[18] U. Haeberlen, J. S. Waugh, Coherent Averaging Effects in Magnetic Resonance, Phys. Rev. **175** 453-467 1968. https://doi.org/10.1103/PhysRev.175.453
[19] U. Haeberlen, High Resolution NMR in Solids: Selective Averaging. Advances in Magnetic Resonance Supplement 1. New York: Academic Press 1976.
[20] S. R. Hartmann, E. L. Hahn, Nuclear Double Resonance in the Rotating Frame, Phys. Rev. **128** 2042-2053 1962. https://doi.org/10.1103/PhysRev.128.2042
[21] A. Pines, M. G. Gibby, J. S. Waugh, Proton-enhanced NMR of Dilute Spins in Solids, J. Chem. Phys. **59** 569-590 1973. https://doi.org/10.1063/1.1680061
[22] J. Schaefer, E. O. Stejskal, Carbon-13 Nuclear Magnetic Resonance of Polymers Spinning at the Magic Angle, J. Am. Chem. Soc. **98** 1031–1032 1976. https://doi.org/10.1021/ja00420a036
[23] R. Freeman, S. P Kempsell, M. H. Levitt, Broadband Decoupling and Scaling of Heteronuclear Spin–Spin Interactions in High-Resolution NMR, J. Magn. Reson. **35** 447–450 1979. https://doi.org/10.1016/0022-2364(79)90067-2
[24] J. S. Waugh, Theory of Broadband Spin Decoupling, J. Magn. Reson. **50** 30–49 1982. https://doi.org/10.1016/0022-2364(82)90029-4
[25] P. Mansfield, P. K. Grannell, NMR 'Diffraction' in Solids?, J. Phys. C **6** L422–L426 1973. https://doi.org/10.1088/0022-3719/6/22/007
[26] P. C. Lauterbur, Image Formation by Induced Local Interactions—Examples Employing Nuclear Magnetic-Resonance, Nature **242** 190–191 1973. https://doi.org/10.1038/242190a0
[27] M. Castillo, L. Kwock L, S. K. Mukherji, Clinical Applications of Proton MR Spectroscopy, Am. J. Neuroradiol. **17** 1-15 1996.
[28] E. D. Rubaek, B. Ross (Eds.). Magnetic Resonance Spectroscopy Diagnosis of Neurological Disease, New York, Marcel Dekker, Inc. 1999.
[29] D.M. Wilson, A.L. Burlingame, Deuterium and Carbon-13 Tracer Studies of Ethanol Metabolism in the Rat by $^{2}H$, $^{1}H$-Decoupled $^{13}C$ Nuclear Magnetic Resonance, Biochem. Biophys. Res. Commun. **56** 828-835 1974. https://doi.org/10.1016/0006-291X(74)90680-9
[30] D. S.Wishart, NMR Metabolomics: A Look Ahead, J. Magn. Reson. **306** 155-161 2019. https://doi.org/10.1016/j.jmr.2019.07.013
[31] A. W. Overhauser, Polarization of Nuclei in Metals, *Phys. Rev*. **92** 411–415 1953. https://doi.org/10.1103/PhysRev.92.411
[32] T. R. Carver and C. P. Slichter, Polarization of Nuclear Spins in Metals, Phys. Rev. **92** 212-213 1953. https://doi.org/10.1103/PhysRev.92.212.2
[33] L. R. Becerra, G. J. Gerfen, R. J. Temkin, D. J. Singel, R. G. Griffin, Dynamic Nuclear Polarization with a Cyclotron Resonance MASER at 5T, Phys. Rev. Lett. **71** 3561-3564 1993. https://doi.org/10.1103/PhysRevLett.71.3561
[34] W. G. Breiland, C. B. Harris, A. Pines, Optically Detected Electron Spin Echoes and Free Precession in Molecular Excited States, Phys. Rev. Lett. **30** 158-161 1972. https://doi.org/10.1103/PhysRevLett.30.158
[35] H. J. Mamin, M. Kim, M. H. Sherwood, C. T. Rettner, K. Ohno, D. D. Awschalom, D. Rugar. Nanoscale Nuclear Magnetic Resonance with a Nitrogen-Vacancy Spin Sensor, Science **339** 557-560 2013. https://doi.org/10.1126/science.1231540

[36] D. Budker, M. Romalis, Optical Magnetometry, Nature Physics **3** 227-234 2007. https://doi.org/10.1038/nphys566

[37] M. Bak, J. T. Rasmussen, N. C. Nielsen, SIMPSON: A General Simulation Program for Solid-State NMR Spectroscopy, J. Magn. Reson. **147** 296-330 2000. https://doi.org/10.1006/jmre.2000.2179

[38] U. Sternberg, R. Witter, I. Kuprov, J. M. Lamley, A. Oss, J. R. Lewandowski, A. Samoson, $^{1}$H Line Width Dependence on MAS Speed in Solid State NMR–Comparison of Experiment and Simulation, J. Magn. Reson. **291** 32-29 2018. https://doi.org/10.1016/j.jmr.2018.04.003

[39] R. Zhang, K. H. Mroue, A. Ramamoorthy, Proton-Based Ultrafast Magic Angle Spinning Solid-State NMR Spectroscopy, Acc. Chem. Res. **50** 1105–1113 2017. https://doi.org/10.1021/acs.accounts.7b00082

[40] D. Doskocilova, B. Schneider, NMR Studies of Swollen Crosslinked Polymer Gels, Pure & Appl. Chem. **54** 575-584 1982. https://doi.org/10.1351/pac198254030575

[41] P. Schanda, M. Ernst, Studying Dynamics by Magic-Angle Spinning Solid-State NMR Spectroscopy: Principles and Applications to Biomolecules, Prog. Nucl. Magn. Reson. Spectrosc. **96** 1-46 2016. https://doi.org/10.1016/j.pnmrs.2016.02.001

[42] A. E. Bennett, C. M. Rienstra, M. Auger, K. V. Lakshmi, and R. G. Griffin, Heteronuclear Decoupling in Rotating Solids, J. Chem. Phys. **103** 6951-6958 1995. https://doi.org/10.1063/1.470372

[43] R. S. Thakur, N. D. Kurur, and P. K. Madhu, Swept-frequency two-pulse phase modulation for heteronuclear dipolar decoupling in solid-state NMR, Chem. Phys. Lett. **426** 459-463 2006. https://doi.org/10.1016/j.cplett.2006.06.007

[44] I. Scholz, P. Hodgkinson, B. H. Meier, M. Ernst Understanding Two-Pulse Phase-Modulated Decoupling in Solid-State NMR, J. Chem. Phys. **130** 114510-114527 2009. https://doi.org/10.1063/1.3086936

[45] A. Equbal. S. Paul, V. S. Mithu, J. M. Vinthera, N. C.Nielsen, P. K. Madhu, rTPPM: Towards Improving Solid-State NMR Two-Pulse Phase-Modulation Heteronuclear Dipolar Decoupling Sequence by Refocusing, J. Magn. Reson. **244** 68-73 2014. https://doi.org/10.1016/j.jmr.2014.04.009

[46] G. Metz, X. L. Wu, S. O. Smith, Ramped-Amplitude Cross Polarization in Magic-Angle-Spinning NMR, J. Magn. Reson. **110** 219-227 1994. https://doi.org/10.1006/jmra.1994.1208

[47] S. Hediger, B. H. Meier, R. R. Ernst, Adiabatic Passage Hartmann-Hahn Cross Polarization in NMR Under Magic Angle Sample Spinning, Chem. Phys. Lett. **240** 449-456 1995. https://doi.org/10.1016/0009-2614(95)00505-X

[48] K. J. Harris A. Lupulescu, B. E. G. Lucier, L. Frydman, R. W. Shurko, Broadband Adiabatic Inversion Pulses for Cross Polarization in Wideline Solid-State NMR Spectroscopy, J. Magn. Reson. **224** 38-47 2012. https://doi.org/10.1016/j.jmr.2012.08.015

[49] J. S. Beck, J. C. Vartuli, W. J. Roth, W.J. M. E. Leonowicz, C. T. Kresge, K. D. Schmitt, C. T. Chu, D. H. Olson, E. W. Sheppard, S. B. McCullen, J. B. Higgins, L. J. Schlenker, A New Family of Mesoporous Molecular Sieves Prepared with Liquid Crystal Templates, J. Am. Chem. Soc. **114** 10834-10843, 1992.

https://pubs.acs.org/doi/10.1021/ja00053a020

[50] D. Zhao, J. Feng, Q. Huo, N. Melosh, G. H. Fredrickson, B. F. Chmelka, G. D. Stucky, Triblock Copolymer Syntheses of Mesoporous Silica with Periodic 50 to 300 Angstrom Pores, Science **279** 548-552 1998. http://doi.org/10.1126/science.279.5350.548

[51] Z. A. ALOthman A Review: Fundamental Aspects of Silicate Mesoporous Materials, Materials **5** 2874-2902 2012. https://doi.org/10.3390/ma5122874

[52] T. Linssen, K. Cassiers, P. Cool, E. F. Vansant, Mesoporous Templated Silicates: an Overview of their Synthesis, Catalytic Activation and Evaluation of the Stability, Adv. Colloid Interface Sci. **103** 121-147 2003. https://doi.org/10.1016/S0001-8686(02)00084-2

[53] M.-A.Springuel-Huet, J.-LBonardet, A. Gédéon, Y. Yue, V. N. Romannikov, J. Fraissard, Mechanical Properties of Mesoporous Silicas and Alumina–Silicas MCM-41 and SBA-15 Studied by $N_2$ Adsorption and $^{129}$Xe NMR, Micropor. Mesopor. Mat. **44-45** 775-784 2001. https://doi.org/10.1016/S1387-1811(01)00260-8

[54] A. Nossov, E. Haddad, F. Guenneau, A. Galarneau, F. Di Renzo, F. Fajula, A. Gedeon, Characterization of the Porosity in SBA-15 Silicas by Hyper-Polarized $^{129}$Xe NMR, J. Phys. Chem. B **107** 45 12456–12460 2003. https://doi.org/10.1021/jp036195p

[55] A. Galarneau, M. Nader, F. Guenneau, F. D. Renzo, A. Gedeon, Understanding the Stability in Water of Mesoporous SBA-15 and MCM-41, J. Phys. Chem. C **111** 8268–8277 2007. https://doi.org/10.1021/jp068526e

[56] C.-S. Ha, S. S. Park, Periodic Mesoporous Organosilicas - Preparation, Properties and Applications, Springer Series in Materials Science 281, Springer Nature Singapore Pte Ltd, 2019. https://doi.org/10.1007/978-981-13-2959-3_1

[57] A. Corma, From Microporous to Mesoporous Molecular Sieve Materials and their use in Catalysis, Chem. Rev. **97** 2373-2419 1997. https://doi.org/10.1021/cr960406n

[58] G. Martínez-Edo, A. Balmori, I. Pontón, A. M. del Rio, D. Sánchez-García, Functionalized Ordered Mesoporous Silicas (MCM-41): Synthesis and Applications in Catalysis, Catalysts **8** 617-679 2018. https://doi.org/10.3390/catal8120617

[59] L.-B. Sun, X.-Q. Liua, H.-C. Zhou, Design and Fabrication of Mesoporous Heterogeneous Basic Catalysts, Chem. Soc. Rev. **44** 5092-5147 2015. https://doi.org/10.1039/C5CS00090D

[60] A. E. Ramirez, J.-M. Clacens, C. Lorentz, Y. Pouilloux, Comparison Between SBA-15 and MCM-41: Structure on the Stability and the Selectivity of Basic Catalysts in Oligomerization of Glycerol, Curr. Org. Chem. **16** 2774-2781 2012**.** https://doi.org/10.2174/138527212804546903

[61] H.-P. Lin, C.-Y. Tang, C.-Y. Lin, Detailed Structural Characterizations of SBA-15 and MCM-41 Mesoporous Silicas on a High-Resolution Transmission Electron Microscope, J. Chin. Chem. Soc. **49** 981-988 2002. https://doi.org/10.1002/jccs.200200140

[62] Y. Liu, Z. Li, X. Yang, Y. Xing, C. Tsai, Q. Yang, Z. Wang R. T. Yang, Performance of Mesoporous Silicas (MCM-41 and SBA-15) and Carbon (CMK-3) in the Removal of Gas-Phase Naphthalene: Adsorption Capacity, Rate and Regenerability, RSC Adv. **6** 21193-21203 2016. https://doi.org/10.1039/C5RA27289K

[63] P. Verma, Y. Kuwahara, K. Mori, R. Raja, H. Yamashita, Functionalized Mesoporous SBA-15 Silica: Recent Trends and Catalytic Applications, Nanoscale **12** 11333-11363 2020. https://doi.org/10.1039/D0NR00732C

[64] A. Kiwilsza, A. Pajzderska, M. A. Gonzalez, J. Mielcarek, J. Wąsicki, QENS and NMR Study of Water Dynamics in SBA-15 with a Low Water Content, J. Phys. Chem. C **119** 29 16578–16586 2015. https://doi.org/10.1021/acs.jpcc.5b02672

[65] A. M. Basso, B. P. Nicola, K. B. Gusmão, S. B. C. Pergher, Tunable Effect of the Calcination of the Silanol Groups of KIT-6 and SBA-15 Mesoporous Materials, Appl. Sci. **10** 970-986 2020. https://doi.org/10.3390/app10030970

[66] C. Y.-Ishii, T. Asefa, N. Coombs, M. J. MacLachlan, G. A. Ozin, Periodic Mesoporous Organosilicas, PMOs: Fusion of Organic and Inorganic Chemistry 'inside' the Channel Walls of Hexagonal Mesoporous Silica, Chem. Comm. **24** 2539-2540 1999. https://doi.org/10.1039/A908252B

[67] B. J. Melde, B. T. Holland, C. F. Blanford, A. Stein, Mesoporous Sieves with Unified Hybrid Inorganic/Organic Frameworks, Chem. Mater. **11** 3302–3308 1999. https://doi.org/10.1021/cm9903935

[68] S. Inagaki, S. Guan, Y. Fukushima, T. Ohsuna, O. Terasaki, Novel Mesoporous Materials with a Uniform Distribution of Organic Groups and Inorganic Oxide in Their Frameworks, J. Am. Chem. Soc., **121** 9611-9614 1999. http://doi.org/10.1021/ja9916658

[69] S. Inagaki, S. Guan, T. Ohsuna, O. Terasaki, An Ordered Mesoporous organosilica Hybrid Material with a Crystal-Like Wall Structure, Nature **416** 304-307 2002. https://doi.org/10.1038/416304a

[70] B. Hatton, K. Landskron, W. Whitnall, D. Perovic, G. A. Ozin, Past, Present, and Future of Periodic Mesoporous Organosilicas - The PMOs, Acc. Chem. Res. **38** 305–312 2005. https://doi.org/10.1021/ar040164a

[71] J. L. Blin, M. Impéror-Clerc, Mechanism of Self-Assembly in the Synthesis of Silica Mesoporous Materials: in situ Studies by X-ray and Neutron Scattering, Chem. Soc. Rev. **42** 4071-4082 2013. https://doi.org/10.1039/C2CS35362H

[72] X. Du, F. Kleitz, X. Li, H. Huang, X. Zhang, S.-Z. Qiao, Disulfide-Bridged Organosilica Frameworks: Designed, Synthesis, Redox-Triggered Biodegradation, and Nanobiomedical Applications, Adv. Funct. Mater. **28** 1707325-35 2018. https://doi.org/10.1002/adfm.201707325

[73] C. Sanchez, L. Rozes, F. Ribot, C. Laberty-Robert, D. Grosso, C. Sassoye, C. Boissiere, L. Nicole, "Chimie Douce": A Land of Opportunities for the Designed Construction of Functional Inorganic and Hybrid Organic-Inorganic Nanomaterials, C. R. Chimie **13** 3-39 2010. https://doi.org/10.1016/j.crci.2009.06.001

[74] S. -H. Wu, C. -Y. Mou, H. -P. Lin, Synthesis of Mesoporous Silica Nanoparticles, Chem. Soc. Rev. **42** 3862-3875 2013. https://doi.org/10.1039/C3CS35405A

[75] M. A. Wahab, I. Imae, Y. Kawakami, C. -S. Ha, Periodic Mesoporous Organosilica Materials Incorporating Various Organic Functional Groups: Synthesis, Structural Characterization, and Morphology, Chem. Mater. **17** 2165–2174 2005. https://doi.org/10.1021/cm0480059

[76] M. Kruk, M. Jaroniec, A. Sayari, Adsorption Study of Surface and Structural Properties of MCM-41 Materials for Different Pore Size, J. Phys. Chem. B **101** 583–589 1997. https://doi.org/10.1021/jp962000k

[77] B. Szczęśniak, J. Choma, M. Jaroniec, Major Advances in the Development of Ordered Mesoporous Materials, Chem. Commun. **56** 7836, 2020. https://doi.org/10.1039/d0cc02840a

[78] P. Llewellyn, 13-Adsorption by Ordered Mesoporous Materials, Adsorption by Powders and Porous Solids (Second Edition)**,** Principles, Methodology and Applications, 529-564 2013. https://doi.org/10.1016/B978-0-08-097035-6.00013-9

[79] S. Shylesh, A. Wagener, A. Seifert, S. Ernst, W.R. Thiel, Mesoporous Organosilicas with Acidic Frameworks and Basic Sites in the Pores: An Approach to Cooperative Catalytic Reactions, Angew. Chem. Int. Ed., **49** 184-187 2010. http://doi.org/10.1002/anie.200903985

[80] D. Jiang, Q. Yang, J. Yang, L. Zhang, G. Zhu, W. Su, C. Li, Mesoporous Ethane−Silicas Functionalized with trans-(1R,2R)-Diaminocyclohexane as Heterogeneous Chiral Catalysts, Chem. Mater. **17** 6154-6160 2005. http://doi.org/10.1021/cm0514084

[81] S. Huh, J. W. Wiench, J. -C. Yoo, M. Pruski, V. S. -Y. Lin, Organic Functionalization and Morphology Control of Mesoporous Silicas via a Co-condensation Synthesis Method, Chem. Mater. **15** 4247-4256 2003. https://doi.org/10.1021/cm0210041

[82] H. -T. Chen, S. Huh, J. W. Wiench, M. Pruski, V. S. -Y. Lin, Dialkylaminopyridine-Functionalized Mesoporous Silica Nanosphere as an Efficient and Highly Stable Heterogeneous Nucleophilic Catalyst, J. Am. Chem. Soc. **127** 13305-13311 2005. https://doi.org/10.1021/ja0524898

[83] R. Kumar, H. -T. Chen, J. L. Escoto, V. S. -Y. Lin, M. Pruski, Template Removal and Thermal Stability of Organically Functionalized Mesoporous Silica Nanoparticles, Chem. Mater., **18** 4319-4327 2006. https://doi.org/10.1021/cm060598v

[84] J. D. Webb, T. Seki, J. F. Goldston, M. Pruski, C. M. Crudden, Selective Functionalization of the Mesopores of SBA-15, Microporous Mesoporous Mater. **203** 123-131 2015. https://doi.org/10.1016/j.micromeso.2014.10.032

[85] J. Trébosc, J.W. Wiench, S. Huh, V.S.-Y. Lin, M. Pruski, Solid-state NMR Study of MCM-41-type Mesoporous Silica Nanoparticles, J. Am. Chem. Soc. **127** 3057-3068 2005. https://doi.org/10.1021/ja043567e

[86] K. Mao, J.W. Wiench, V.S.-Y. Lin, M. Pruski, Indirectly Detected Through-Bond Chemical Shift Correlation NMR Spectroscopy in Solids under Fast MAS: Studies of Organic–Inorganic Hybrid Materials, J. Magn. Reson. **196** 92-95 2009. https://doi.org/10.1016/j.jmr.2008.10.010

[87] J. W. Wiench, C. E. Bronnimann, V. S. -Y. Lin, M. Pruski, Chemical Shift Correlation NMR Spectroscopy with Indirect Detection in Fast Rotating Solids: studies of Organically Functionalized Mesoporous Silicas, J. Am. Chem. Soc. **129** 12076-12077 2007. https://doi.org/10.1021/ja074746+

[88] K. Mao, J. L. Rapp, J. W. Wiench, M. Pruski, Characterization of Nanostructured Organic-Inorganic Hybrid Materials Using Advanced Solid-State NMR Spectroscopy,

Mater. Res. Soc. Symp. Proc., **1184** 2009. https://doi.org/10.1557/PROC-1184-HH07-01

[89] I. Langmuir, The Adsorption of Gases on Plane Surfaces of Glass, Mica and Platinum, J. Am. Chem. Soc. **40** 1361–1403 1918. https://doi.org/10.1021/ja02242a004

[90] M. Kruk, M. Jaroniec, Characterization of the Porous Structure of SBA-15, Chem. Mater. **12** 1961-1968 2000. https://doi.org/10.1021/cm000164e

[91] S. Brunauer, P. H. Emmett, E. Teller, Adsorption of Gases in Multimolecular Layers, J. Am. chem. Soc. **60** 309-319 1938. https://doi.org/10.1021/ja01269a023

[92] S. Lowell, J. E. Shields, M. A. Thomas, M. Thommes, Characterization of Porous Solids and Powders: Surface Area, Pore Size and Density, Springer Netherlands, 2004. https://doi.org/10.1007/978-1-4020-2303-3

[93] K. Morishige, M. Tateishi, Accurate Relations between Pore Size and the Pressure of Capillary Condensation and the Evaporation of Nitrogen in Cylindrical Pores, Langmuir **22** 4165–4169 2006.

[94] E. M. Voigt, R. H. Tomlinson, The Determination of Pore Size Distribution and Surface Area from Adsorption Isotherms, Can. J. Chem. **33** 215-231 1955. https://doi.org/10.1139/v55-025

[95] l. P. Barrett, L. G. Joyner, P. P. Halenda, The Determination of Pore Volume and Area Distributions in Porous Substances. I. Computations from Nitrogen Isotherms, J. Am. Chem. Soc. **73** 373–380 1951. https://doi.org/10.1021/ja01145a126

[96] Y. Zhang,F. L. -Y. Lam, Z.-F. Yan, X. Hu, Review of Kelvin's Equation and Its Modification in Characterization of Mesoporous Materials, Chin. J. Chem. Phys. **19** 102-108 2006. https://doi.org/10.1360/cjcp2006.19(2).102.7

[97] T. Kobayashi, O. Lafon, A.S.L. Thankamony, I.I. Slowing, K. Kandel, D. Carnevale, V. Vitzthum, H. Vezin, J.-P. Amoureux, G. Bodenhausen, Analysis of Sensitivity Enhancement by Dynamic Nuclear Polarization in Solid-State NMR: a case Study of Functionalized Mesoporous Materials, Phys. Chem. Chem. Phys. **15** 5553-5562 2013. https://doi.org/10.1039/C3CP00039G

[98] S. Pizzanelli, S. Kababya, V. Frydman, M. Landau, S. Vega, NMR Study of the Adsorption−Desorption Kinetics of Dissolved Tetraalanine in MCM-41 Mesoporous Material, J. Phys. Chem. B **109** 8029-8039 2005. http://doi.org/10.1021/jp044389e

[99] B. Grünberg, T. Emmler, E. Gedat, I. Shenderovich, G. Findenegg, H. H. Limbach, G. Buntkowsky, Hydrogen Bonding of Water Confined in Mesoporous Silica MCM-41 and SBA-15 Studied by $^{1}$H Solid-State NMR, Chem. Eur. J. **10** 5689-5696 2004. http://doi.org/10.1002/chem.200400351

[100] A. Vyalikh, T. Emmler, B. Grünberg, Y. Xu, I. Shenderovich, G. Findenegg, H.-H. Limbach, G. Buntkowsky, Hydrogen Bonding of Water Confined in Controlled-Pore Glass 10-75 Studied by 1H-Solid State NMR, Z. Phys. Chem. **221** 155-168 2007. http://doi.org/10.1524/zpch.2007.221.1.155

[101] T. Amitay-Rosen, S. Kababya, S. Vega, A Dynamic Magic Angle Spinning NMR Study of the Local Mobility of Alanine in an Aqueous Environment at the Inner Surface of Mesoporous Materials, J. Phys. Chem. B **113** 6267-6282 2009. http://doi.org/10.1021/jp810572r

[102] T. Amitay-Rosen, S. Vega, A deuterium MAS NMR Study of the Local Mobility of Dissolved Methionine and Di-Alanine at the Inner Surface of SBA-15, Phys. Chem. Chem. Phys. **12** 6763-6773 2010. http://doi.org/10.1039/b924813g

[103] A. Steel, S. W. Carr, M. W. Anderson, $^{29}$Si Solid-State NMR Study of Mesoporous M41S Materials, Chem. Mater. **7** 1829–1832 1995. https://doi.org/10.1021/cm00058a012

[104] C. C. Liu, G. E. Maciel, The Fumed Silica Surface: A Study by NMR, J. Am. Chem. Soc. **118** 5103–5119 1996. https://doi.org/10.1021/ja954120w

[105] Dassault Systèmes, BIOVIA, Materials Studio, San Diego, 2017.

[106] R. Notman, T. R. Walsh, Molecular Dynamics Studies of the Interactions of Water and Amino Acid Analogues with Quartz Surfaces, Langmuir **25** 1638–1644 2009. https://doi.org/10.1021/la803324x

[107] A. Rimola, D. Costa, M. Sodupe, J. -F. Lambert, P. Ugliengo, Silica Surface Features and Their Role in the Adsorption of Biomolecules: Computational Modeling and Experiments. Chem. Rev. **113** 4216-313 2013. https://doi.org/10.1021/cr3003054

[108] A Chaffee, Molecular Modeling of HMS Hybrid Materials for $CO_2$ Adsorption. Fuel Process. Technol. **86** 1473-1486 2005. https://doi.org/10.1016/j.fuproc.2005.01.013

[109] I. -S. Chuang, G. E. Maciel, Probing Hydrogen Bonding and the Local Environment of Silanols on Silica Surfaces via Nuclear Spin Cross Polarization Dynamics, J. Am. Chem. Soc. **118** 401–406 1996. https://doi.org/10.1021/ja951550d

[110] M. Sattig, S. Reutter, F. Fujara, M. Werner, G. Buntkowsky, M. Vogel, NMR Studies on the Temperature-Dependent Dynamics of Confined Water, Phys. Chem. Chem. Phys. **16** 19229-19240 2014. https://doi.org/10.1039/C4CP02057J

[111] M. Brodrecht, B. Kumari, H. Breitzke, T. Gutmann, G. Buntkowsky, Chemically Modified Silica Materials as Model Systems for the Characterization of Water-Surface Interactions, Z. Phys. Chem. **232** 1127-1146 2018. http://doi.org/10.1515/zpch-2017-1059

[112] M. Weigler, M. Brodrecht, G. Buntkowsky, M. Vogel, Reorientation of Deeply Cooled Water in Mesoporous Silica: NMR Studies of the Pore-Size Dependence, J. Phys. Chem. B **123** 2123-2134 2019. http://doi.org/10.1021/acs.jpcb.8b12204

[113] M. Slivinska-Bartkowiak, M. Jazdzewska, L. L. Huang, K. E. Gubbins, Melting Behavior of Water in Cylindrical Pores: Carbon Nanotubes and Silica Glasses, Phys. Chem. Chem. Phys. **10** 4909-4919 2008. https://doi.org/10.1039/B808246D

[114] T. Azais, G. Hartmeyer, S. Quignard, G. Laurent, F. Babonneau, Solution State NMR Techniques Applied to Solid State Samples: Characterization of Benzoic Acid Confined in MCM-41, J. Phys. Chem. C **114** 8884-8891 2010. https://doi.org/10.1021/jp910622m

[115] V. S. Veena, I. Kavya, A. Lazar, C. P. Vinod, T. G. Ajithkumar, S. Jayanthi, Distribution of Water in the Pores of Periodic Mesoporous Organosilicates – a Proton Solid State MAS NMR Study, Phys. Chem. Chem. Phys. **20** 29351-29361 2018. https://doi.org/10.1039/C8CP04902E

[116] D. Massiot, F. Fayon, M. Capron, I. King, S. Cal, B. Alonso, J.-O. Durand, B. Bujoli, Z. Gan, G. Hoatson, Modelling One- and Two-dimensional Solid-State NMR Spectra, Magn. Reson. Chem. **40** 70-76 2002. http://doi.org/10.1002/mrc.984

[117] H. W. Spiess, Interplay of Structure and Dynamics in Macromolecular and Supramolecular Systems, Macromolecules **43** 5479-5491 2010. http://doi.org/10.1021/ma1005952

[118] M. R. Hansen, R. Graf, H. W. Spiess, Solid-State NMR in Macromolecular Systems: Insights on How Molecular Entities Move, Acc. Chem. Res. **46** 1996-2007 2013. https://doi.org/10.1021/ar300338b

[119] H. W. Spiess, 50th Anniversary Perspective: The Importance of NMR Spectroscopy to Macromolecular Science. Macromolecules **50** 1761-1777 2017. https://doi.org/10.1021/acs.macromol.6b02736

[120] C. M. Gall, J. A. DiVerdi, S. J. Opella, Phenylalanine Ring dynamics by Solid State $^2$H NMR, J. Am. Chem. Soc. **103** 5039-5043 1981. https://doi.org/10.1021/ja00407a012

[121] M. H. Frey, J. A. DiVerdi, S. J. Opella, Dynamics of Phenylalanine in the Solid State by NMR, J. Am. Chem. Soc. **107** 7311-7315 1985. https://doi.org/10.1021/ja00311a016

[122] T. M. Alam, J. Orban, G. P. Drobny, Deuterium NMR Investigation of Backbone Dynamics in the Synthetic Oligonucleotide [d (CGCGAATTCGCG)]$_2$, Biochemistry, **30** 9229-9237 1991. https://doi.org/10.1021/bi00102a014

[123] D. A. Torchia, A. Szabo, Spin-lattice Relaxation in Solids, J. Magn. Reson. **1** 107-121 1982. https://doi.org/10.1016/0022-2364(82)90301-8

[124] R. L. Vold, G. L. Hoatson, Effects of Jump Dynamics on Solid State Nuclear Magnetic Resonance Lineshapes and Spin Relaxation Times, J. Magn. Reson. **198** 57-72 2009. https://doi.org/10.1016/j.jmr.2009.01.008

[125] V. Macho, l. Brombacher, H. W. Spiess, The NMR-WEBLAB: An Internet Approach to NMR Lineshape Analysis, Appl. Magn. Reson. **20** 405-432 2001. https://doi.org/10.1007/BF03162288

[126] N. F. Breen, K. Li, G. l. Olsen, G. P. Drobny, Deuterium Magic Angle Spinning NMR Used to Study the Dynamics of Peptides Adsorbed onto Polystyrene and Functionalized Polystyrene Surfaces, J. Chem. Phys. B **115** 9452-9460 2011. https://doi.org/10.1021/jp1101829

[127] S. Jayanthi, V. Frydman, S. Vega, Dynamic Deuterium Magic Angle Spinning NMR of a Molecule Grafted at the Inner Surface of a Mesoporous Material, J. Phys. Chem. B **116** 10398-10405 2012. https://doi.org/10.1021/jp3061152

[128] H.M. McConnell, Reaction Rates by Nuclear Magnetic Resonance, J. Chem. Phys. **28** 430-431 1958. https://doi.org/10.1063/1.1744152

[129] P. Ugliengo, M. Sodupe, F. Musso, I. J. Bush, R. Orlando, R. Dovesi, Realistic Models of Hydroxylated Amorphous Silica Surfaces and MCM-41 Mesoporous Material Simulated by Large-scale Periodic B3LYP Calculations, Adv. Mater. **20** 4579-4583 2008. https://doi.org/10.1002/adma.200801489

[130] W. Kohn, L. J. Sham, Self-Consistent Equations Including Exchange and Correlation Effects, Phys. Rev. **140** A1133-A1138 1965. https://doi.org/10.1103/PhysRev.140.A1133

[131] D. Costa, A. Tougerti, F. Tielens, C. Gervais, l. Stievano, J. F. Lambert, DFT Study of the Adsorption of Microsolvated Glycine on a Hydrophilic Amorphous Silica Surface, Phys. Chem. Chem. Phys. **10** 6360-6368 2008. https://doi.org/10.1039/b806501b

[132] D. Costa, P.-A. Garrain, B. Diawara, P. Marcus, Biomolecule-Biomaterial Interaction: A DFT-D Study of Glycine Adsorption and Self-Assembly on Hydroxylated $Cr_2O_3$ Surfaces, Langmuir **27** 2747-2760 2011. https://dx.doi.org/10.1021/la104317j

[133] N. Folliet, C. Gervais, D. Costa, G. aurent, F. Babonneau, L. Stievano, J. F. lambert, F. Tielens, A Molecular Picture of the Adsorption of Glycine in Mesoporous Silica through NMR Experiments Combined with DFT‑D Calculations, J. Phys. Chem. C **117** 4104-4114 2013. https://dx.doi.org/10.1021/jp312195a

[134] I. Ben Shir, S. Kababya, A. Schmidt, Molecular Details of Amorphous Silica Surface Determine Binding Specificity to Small Amino Acids, J. Phys. Chem. C **118** 7901-7909 2014. https://dx. dx.doi.org/10.1021/jp409030w

[135] A. Cimas, F. Tielens, M. Sulpizi, M. –P. Gaigeot, D. Costa, The Amorphous Silica–Liquid Water Interface Studied by *ab initio* Molecular Dynamics (AIMD): Local Organization in Global Disorder, J. Phys. **26** 244106-244116 2014. https://dx.doi.org/10.1088/0953-8984/26/24/244106

[136] S. Jayanthi, M. Werner, Y. Xu, G. Buntkowsky, S. Vega, Restricted Dynamics of a Deuterated Linker Grafted on SBA-15 Revealed by Deuterium MAS NMR, J. Phys. Chem. C **117** 13114-13121 2013. https://doi.org/10.1021/jp4028782

[137] S. Jayanthi, S. Kababya, A. Schmidt, S. Vega, Deuterium MAS NMR and Local Molecular Dynamic Model to Study Adsorption–Desorption Kinetics of a Dipeptide at the Inner Surfaces of SBA-15, J. Phys. Chem. C, **120** 2797-2806 2016. https://doi.org/10.1021/acs.jpcc.5b11429

[138] H. Sun. Compass: An ab initio Force-Field Optimized for Condensed-Phase Applications Overview with Details on Alkane and Benzene Compounds. J. Phys. Chem. B **102** 7338-7364 1998. https://doi.org/10.1021/jp980939v

[139] W. R. Grùning, A. J. Rossini, A. Zagdoun, D. Gajan, A. Lesage, L. Emsley and C. Copéret, Molecular-level Characterization of the Structure and the Surface Chemistry of Periodic Mesoporous Organosilicates using DNP-Surface Enhanced NMR Spectroscopy, Phys. Chem. Chem. Phys. **15** 13270–13274 2013. https://doi.org/10.1039/C3CP00026E

[140] F. Lin, M. Mertens, P. Cool, S. Doorslaer, Influence of Synthesis Conditions on Properties of Ethane-Bridged Periodic Mesoporous Organosilica Materials as Revealed by Spin-Probe EPR, J. Phys. Chem. C, **117** 22723–22731 2013. http://doi.org/10.1021/jp4061076

[141] J. T. A. Jones, C. D. Wood, C. Dickinson and Y. Z. Khimyak, Periodic Mesoporous Organosilicas with Domain Functionality: Synthesis and Advanced Characterization, Chem. Mater. **20**, 3385–3397 2008. https://doi.org/10.1021/cm7036124

[142] J. Mietner, F. Brieler, L. Y. Joo, M. Fröba, Properties of Water Confined in Periodic Mesoporous Organosilicas: Nanoimprinting the Local Structure, Angew. Chem., Int. Ed. **56** 12348–12351 2017. https://doi.org/10.1002/anie.201705707

[143] D. J. States, R. Haberkorn, D. Ruben, A Two-Dimensional Nuclear Overhauser Experiment with Pure Absorption Phase in Four Quadrants, J. Magn. Reson. **48** 286-292 1982. https://doi.org/10.1016/0022-2364(82)90279-7

[144] C. Lei, Y. Shin, J. Liu, E. J. Ackerman, Entrapping Enzyme in a Functionalized Nanoporous Support, J. Am. Chem. Soc. **124** 11242−11243 2002. https://doi.org/10.1021/ja026855o

[145] J. Deere, E. Magner, J. Wall, B. Hodnett, Adsorption and Activity of Cytochrome C on Mesoporous Silicates., Chem. Commun. **5** 465-465 2001. https://doi.org/10.1039/B009478L

[146] T. Cass, F. S. Ligler, Immobilized Biomolecules in Analysis-A Practical Approach; Oxford: Oxford University Press: 1998.

[147] D. Zhao, Q. Huo, J. Feng, B.F. Chmelka, G.D. Stucky, Nonionic Triblock and Star Diblock Copolymer and Oligomeric Surfactant Syntheses of Highly Ordered, Hydrothermally Stable, Mesoporous Silica Structures. J. Am. Chem. Soc. **120** 6024−6036 1998. https://doi.org/10.1021/ja974025i

[148] H. Takahashi, B. Li, T. Sasaki, C. Miyazaki, T. Kajino, S. Inagaki, Immobilized Enzymes in Ordered Mesoporous Silica Materials and Improvement of their Stability and Catalytic Activity in an Organic Solvent, Microporous Mesoporous Mater., **44** 755-762 2001. https://doi.org/10.1016/S1387-1811(01)00257-8

[149] J. Liu, M.K. Chaudhury, D.H. Berry, J.E. Seebergh, J.H. Osborne, K.Y. Blohowiak, Effect of Surface Morphology on Crack Growth at a Sol-Gel Reinforced Epoxy/Aluminum Interface. J. Adhes. Sci. Technol. **20** 277−305 2006. https://doi.org/10.1080/00218460600713725

[150] Q. Wang, N. Liu, X. Wang, J. Li, X. Zhao, F. S. Wang, Conductive Hybrids from Water-Borne Conductive Polyaniline and (3-Glycidoxypropyl)trimethoxysilane. Macromolecules **36** 5760−5764 2003. https://doi.org/10.1021/ma0345246

[151] W. Que, Y. Zhou, Y. L. Lam, Y. C. Chan, C. H. Kam, Preparation and Characterization of $SiO_2/TiO_2$/gamma-glycidoxypropyltrimethoxysilane Composite Materials for Optical Waveguides. Appl. Phys. A **73** 171−176 2001. https://doi.org/10.1007/s003390000612

[152] G. Dubois, W. Volksen, R. D. Miller, Dielectric Films for Advanced Microelectronics; Wiley: Hoboken, 2007.

[153] L. Connell, L. Gabrielli, O. Mahony, L. Russo, L. Cipolla, J. Jones, Functionalizing Natural Polymers with Alkoxysilane Coupling agents: Reacting 3-Glycidoxypropyl Trimethoxysilane with Poly (γ-glutamic acid) and Gelatin, Polym. Chem. **8** 1095-1103 2017. https://doi.org/10.1039/C6PY01425A

[154] L. Gabrielli, L. Connell, L. Russo, J. Jiménez-Barbero, F. Nicotra, L. Cipolla, J.R. Jones, Exploring GPTMS Reactivity Against Simple Nucleophiles: Chemistry Beyond Hybrid Materials Fabrication, RSC Adv. **4** 1841-1848 2014. https://doi.org/10.1039/C3RA44748K

[155] A. Yamada-Nosaka, H. Tanzawa, $^1$H-NMR Studies on Water in Methacrylate Hydrogels. II, J. Appl. Polym. Sci. **43** 1165-1170 1991. https://doi.org/10.1002/app.1991.070430617

[156] L. Ma, N. Li, J. Zhu, X. Chen, Visible Light-Induced Metal Free Surface Initiated Atom Transfer Radical Polymerization of Methyl Methacrylate on SBA-15, Polymers **9** 58-69 2017. https://doi.org/10.3390/polym9020058

[157] P. Innocenzi, T. Kidchob, T. Yoko, Hybrid Organic-Inorganic Sol-Gel Materials Based on Epoxy-Amine Systems, J. Solgel Sci. Technol., **35** 225-235 2005. http://doi.org/10.1007/s10971-005-2290-4

[158] P. Innocenzi, C. Figus, T. Kidchob, M. Valentini, B. Alonso, M. Takahashi, Sol-gel reactions of 3-glycidoxypropyltrimethoxysilane in a highly basic aqueous solution, Dalton Trans., 9146-9152 2009. http://doi.org/10.1039/B905830C

[159] M. Ojeda, M. Mazaj, S. Garcia, J. Xuan, M. M. Maroto-Valer, N. Z. Logar, Novel Amine-Impregnated Mesostructured Silica Materials for $CO_2$ Capture. Energy Procedia **114** 2252−2258 2017. https://doi.org/10.1016/j.egypro.2017.03.1362

[160] L. Yu, M. Kanezashi, H. Nagasawa, T. Tsuru, Role of Amine Type in $CO_2$ Separation Performance within Amine Functionalized Silica/Organosilica Membranes: A Review, Appl. Sci. **8** 1032 2018. https://doi.org/10.3390/app8071032

[161] W.-K. Cheah, Y.-L. Sim, F.-Y. Yeoh, Amine-functionalized mesoporous silica for urea adsorption, Mater. Chem. Phys. **175** 151-157 2016. https://doi.org/10.1016/j.matchemphys.2016.03.007

[162] A. Stein, B. J. Melde, R. C. Schroden, Hybrid Inorganic−Organic Mesoporous Silicates-Nanoscopic Reactors Coming of Age, Adv. Mater. **12** 1403−1419 2000. doi:10.1002/1521-4095(200010)12:19%3C1403::AID-ADMA1403%3E3.0.CO;2-X

[163] I. Ben Shir, S. Kababya, T. Amitay-Rosen, Y. S. Balazs, A. Schmidt, Molecular Level Characterization of the Inorganic−Bioorganic Interface by Solid State NMR: Alanine on a Silica Surface, a Case Study. J. Phys. Chem. B **114** 5989−5996 2010. https://doi.org/10.1021/jp100114v

[164] J.D. van Beek, matNMR: A Flexible Toolbox for Processing, Analyzing and Visualizing Magnetic Resonance Data in Matlab®, J. Magn. Reson. **187** 19-26 2007. https://doi.org/10.1016/j.jmr.2007.03.017

[165] A. Bendjeriou-Sedjerari, J. D. Pelletier, E. Abou-Hamad, L. Emsley, J. -M. Basset, A Well-Defined Mesoporous Amine Silica Surface via a Selective Treatment of SBA-15 with Ammonia, Chem. Commun., **48** 3067-3069 2012. http://doi.org/10.1039/C2CC00143H

[166] G. Buntkowsky, M. Vogel, R. Winter, Properties of Hydrogen Bonded Liquids at Interfaces. Z. Phys. Chem., **232** 937−972 2018. https://doi.org/10.1515/zpch-2018-1110

[167] M. Weigler, M. Brodrecht, H. Breitzke, F. Dietrich, M. Sattig, G. Buntkowsky, M. Vogel, 2H NMR Studies on Water Dynamics in Functionalized Mesoporous Silica, Z. Phys. Chem, **232** 1041-1058 2018. https://doi.org/10.1515/zpch-2017-103

[168] H. K. Livingston, Cross-Sectional Areas of Molecules Adsorbed on Solid Surfaces, J. Am. Chem. Soc., **66**(4) 569-573 1944. https://doi.org/10.1021/ja01232a021

[169] D. Hentschel, H. Sillescu, H. W. Spiess, Molecular Motion in Solid Polyethylene as Studied by 2D Wide Line NMR Spectroscopy. Makromol. Chem. **180** 241−267 1979. https://doi.org/10.1002/macp.1979.021800123

[170] O. Pschorn, H. W. Spiess, Deuterium Lineshape Study of Tetrahedral Jumps in Solid Hexamethylenetetramine. J. Magn. Reson. **39** 217−228 1980. https://doi.org/10.1016/0022-2364(80)90131-6

[171] H. W. Spiess, Molecular Dynamics of Solid Polymers as Revealed by Deuteron NMR. Colloid Polym. Sci. **261**, 193−209 1983. https://doi.org/10.1007/BF01469664

[172] L. W. Jelinski, J. J. Dumais, A. K. Engel, Solid State $^{2}$H NMR Studies of Molecular Motion. NMR Macromol. **247** 55−65 1984. https://doi.org/10.1021/bk-1984-0247.ch004